Optomechanics and Squeezed light

Michaël Croquette

SORBONNE UNIVERSITÉ

LKB

THÈSE DE DOCTORAT
DE SORBONNE UNIVERSITÉ

Spécialité : Physique

École doctorale n°564: Physique en Île-de-France

réalisée

au Laboratoire Kastler Brossel

sous la direction de Pierre-François Cohadon

présentée par

Michaël Croquette

pour obtenir le grade de :

DOCTEUR DE SORBONNE UNIVERSITÉ

Sujet de la thèse :

Optomécanique et lumière comprimée

soutenue le 7 décembre 2022

devant le jury composé de :

M.	Ludovic BELLON	Rapporteur
M.	Kamel BENCHEIKH	Rapporteur
M.	Jérôme DEGALLAIX	Examinateur
Mme	Sara DUCCI	Examinatrice
Mme	Emily LAMOUR	Présidente du Jury
M.	Pierre-François COHADON	Directeur de thèse

Remerciements

Je suis rentré dans l'équipe Optomécanique du laboratoire Kastler Brossel en avril 2018 pour commencer mon stage de M2. J'arrivais en terrain connu, Pierre-François m'avait fait passer mon entretien pour rentrer à l'ENS et avait été mon tuteur, m'aidant à trouver mon stage de M1. Je tiens donc à le remercier en premier, car il a eu un grand rôle dans mon épanouissement à l'ENS, mais également pendant ma thèse durant laquelle il m'a soutenue face aux difficultés (genou, cryostat, Covid19, in that order) rencontrées. Je le remercie particulièrement pour ses relectures et corrections apportées à mon manuscrit et à mon oral de soutenance qui ont permis de les rendre lisibles et audibles.

Je rejoignais également dans l'équipe Rémi Metzdorff qui finissait sa thèse et Sheon Chua qui finissait son postdoc. Les deux étaient donc pressées par le temps et ils ont pourtant été d'une patience infinie avec moi. J'ai énormément appris auprès d'eux et je les remercie du travail qu'ils ont fourni sur les deux expériences que j'ai reprises. Et je les remercie encore d'être restés disponibles et d'encore aujourd'hui répondre à mes nombreuses questions.

Les permanents de l'équipe ont aussi tous eu un rôle important pour moi. Samuel Deleglise m'a particulièrement aidé sur les manips et apporte une énergie incroyable à l'équipe. Il réussit également l'exploit d'être sympathique malgré ses opinions politiques douteuses. Tristan Briant et Thibaut Jacqmin sont plus absorbés par leur tâche d'enseignement, mais j'ai eu la chance de la partager avec eux et de constater qu'ils étaient tous les deux des professeurs passionnants et je les remercie d'avoir toujours su se montrer disponibles pour répondre à mes questions. Enfin, je remercie également Antoine Heidmann qui est toujours membre de l'équipe et qui reste à l'écoute des doctorants malgré son rôle chronophage de directeur du laboratoire.

Mais on sait tous que ce sont les thésards qui font tout le boulot dans l'équipe donc je tiens à remercier Thibault Capelle et Édouard Ivanov qui ont toujours pris le temps de m'aider en tant que thésards plus expérimentés et qui ont eu la gentillesse de nous fabriquer des échantillons alors qu'ils étaient en train de finir leur thèse. La nouvelle génération de thésard a su se montrer à la hauteur et je souhaite le meilleur à Émile Ferreux, Kyrylo Gerashenko, Luis Najera et Himanshu Patange. Je tiens particulièrement à remercier Ferhat qui a commencé et finit sa thèse en même temps que moi. C'est toujours un plaisir de discuter de tout avec lui et il a réussi à rendre les derniers mois de rédaction, qui sont habituellement pénibles, agréables pour nous deux grâce à sa merveilleuse sympathie.

Au cours de ma thèse, j'ai particulièrement travaillé avec Alexandre Journeaux et Guillaume Dangoisse qui ont tous les deux fait un stage de 6 mois au laboratoire. C'était un plaisir de travailler avec eux et je suis convaincu de la réussite future de leur thèse

qu'il s'apprête chacun à commencer. Enfin au cours de ma dernière année de thèse, Pierre-Edouard Jacquet est arrivé au laboratoire pour commencer sa thèse qui reprendra l'expérience de squeezing. Son enthousiasme débordant et sa bonne humeur m'ont complètement remotivé et je le remercie sincèrement pour ça. Je lui souhaite également le meilleur pour ses années de thèse à venir.

J'ai également eu la chance de collaborer avec d'autres laboratoires, je remercie donc toute l'équipe de CALVA à l'IN2P3 et notamment Angélique Vollard, Manuel Andia, Pierre Gruning, Aymeric Van de Walle et Nicolas Leroy. C'était un plaisir de collaborer avec eux et ils m'ont toujours très bien reçu à Orsay. Je remercie également Jérôme Degallaix du LMA pour sa contribution sur les revêtements des miroirs. Il a toujours été de bon conseil et a ensuite accepté de faire partie de mon jury. Enfin, je remercie l'équipe de Francesco Marin pour leurs échantillons de très bonne qualité qu'ils ont eu la gentillesse de faire pour nous.

Je remercie Ludovic Bellon et Kamel Bencheikh d'avoir accepté d'être rapporteurs et Emily Lamour, Sara Ducci et Jerome Degallaix d'avoir accepté d'être examinateurs. Je remercie également le projet SIRTEQ qui a financé mon doctorat.

J'ai mentionné (à peu près) toutes les personnes qui m'ont aidé sur le plan scientifique, mais je dois aussi remercier les services du laboratoire, notamment les ateliers électroniques et mécanique qui ont été essentiels dans le développement de nos expériences et avec qui il a toujours été agréable de collaborer. Et enfin un petit mot pour les thésards des autres équipes qui sont devenus des amis, je pense à Tom, Anne, Arthur, Yohann, Jérémy, Paul, Léa et Adrien (qui l'était déjà avant et qui l'est devenu encore plus).

J'en arrive donc à remercier mes amis qui m'ont soutenu pendant ma thèse en se montrant curieux de mes recherches et qui m'ont toujours apporté une confiance folle. Il m'est arrivé de penser que je n'arriverais jamais à rédiger cette thèse, mais leur conviction inébranlable du contraire s'est avérée contagieuse. La liste pourrait être très longue, mais je tiens à nommer Hugo qui est tout simplement le meilleur; Robin et Vassilis avec qui j'ai eu le plaisir de vivre en colocation pendant les 2 premières années de ma thèse et de partager des repas de gourmets ; Charles, Lauranne, Flore, Maxime, Sacha et Maylis que j'ai le bonheur de connaitre depuis le Lycée et qui ont fait l'effort de venir à ma soutenance pour m'entendre baragouiner pendant 2h sans rien comprendre; Hortense, Simon Ben Arous, Juliette, Arthur, Thomas, mais aussi Bertin, Divol, Félicien, Élise, Simon Rosenberg, Yann, Romi et Clément qui ont rendu ma vie très chouette depuis 2015. Enfin celle qui a supporté mes explications foireuses et mes vulgarisations improvisées avec patience et une attention parfois impitoyable, je tiens à remercier Solène qui m'a supporté et soutenu pendant ces quatre années.

Je finirais par le plus important, ma famille qui a toujours rendu ma vie facile et heureuse. Peu de gens peuvent appeler leur mère quand ils ont un problème de cryostat où leur père pour discuter de bootstrap. Je les remercie pour leurs conseils et leur incroyable soutien. Je remercie aussi mes sœurs Magali et Sandra qui malgré leurs enfants Gaby, Maxime, Noa et Lenny qui ont rendu mes vacances particulièrement heureuses, m'ont toujours accordé du temps et se sont intéressées à mon travail. Je remercie enfin ma grand-mère Marie-Anne Bouchiat pour son soutien indéfectible et sa curiosité admirable.

Contents

Introduction to the thesis

Optics has long been a field of physics characterized by high-level instrumentation and extremely sensitive experiments. While at the end of the 19th century most founding experiments in thermodynamics or electromagnetism were performed with very basic experimental setups, in 1887, Michelson and Morley refine the Michelson interferometer to a sensitivity below an hundredth of an optical fringe putting an experimental end to the ether controversy. Soon after, the invention of the Fabry-Perot interferometer greatly increased the resolution of spectroscopic measurements.

But it is the invention of the laser in 1960 that definitely gives interferometry its unique status. Even though the radiation sources available in the 1960s are still far from the limits enforced by the quantum nature of light, laser interferometry appears as a natural candidate to achieve a unique experimental challenge: the detection of gravitational waves [1], which actually involves both a km-scale Michelson interferometer and Fabry-Perot cavities inside the arms.

At first, the mirrors have only been dealt with as fixed objects reflecting light, but at the end of the seventies, Carlton Caves starts to consider the mirrors as movable objects sensitive to the radiation pressure force from the reflected light [2]. Taking into account both phase and amplitude quantum fluctuations of the light beam, he demonstrates that ultrasensitive interferometric measurements such as gravitational wave detection are limited by two fundamental noise sources: phase noise (also often referred to as *quantum shot noise*, QSN) and quantum-radiation pressure noise (QRPN). As both noises have an inverse dependence with laser power, this yields to a limit, the *Standard Quantum Limit* (SQL), which is the smallest displacement measurable with a coherent laser field. As a consequence, the mirrors upgrade their status. From mere reflecting systems, they turn into real physical object of study, which move in reaction to radiation-pressure fluctuations of the probe laser beam. *Optomechanics* is born, at least on theoretical grounds.

The existence of the SQL has been an important motivation for the generation of squeezed light [3, 4, 5] as squeezed states allow to go beyond the SQL. It took more than thirty years from the first demonstration of squeezing in 1985 [6] to routine operation of squeezed light sources with graviational-wave interferometers (GWI) [7, 8], but squeezed light now is an essential ingredient of the sensitivity of GWI and more progress is expected soon, with frequency-dependent squeezing implemented both in LIGO and Virgo for the 4th LIGO-Virgo-KAGRA Observation Run, due to start in the spring of 2023.

In parallel, starting in the 1990s, tremendous progress made in parallel in ultrastable laser sources, sensitive photodetectors, low-noise electronics, high-Q mechanics, low-loss

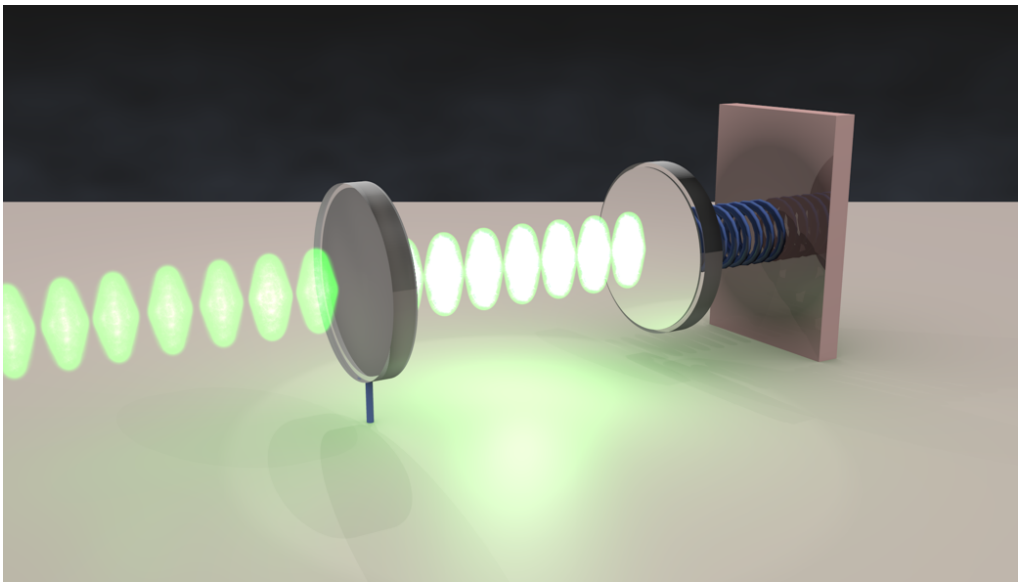

Fig. .1 **The generic optomechanical system***: a linear single-input Fabry-Perot cavity, with an end mirror clamped to a vibrating object (represented here by a spring). Image from [9].*

optical coatings and micro-fabrication have enabled the field of table-top experimental optomechanics to be born. The generic optomechanical physical system, very similar to the systems actually investigated in this thesis, is quite simple: it consists of a linear optical Fabry-Perot cavity where the end mirror is movable. Here, the spring represents the displacement of the mirror, which can be either related to an internal degree of freedom of the mirror substrate, or a mechanical resonator onto which the mirror is clamped. Such systems have been instrumental in investigating quantum limits in simple systems.

As all vibrations modes of the mirrors can be described to a very good extent as (quantum) harmonic oscillators, they display quantum fluctuations (of position, momentum...) of their own. In analogy to the laser cooling of atoms and ions, radiation pressure can be used to laser cool the motion of these macroscopic objects, possibly down to the quantum ground state [10]. Such experiments, pioneered at LKB in the late 1990S [11] and early 2000s, have been responsible for the popularity and tremendous growth of the field of optomechanics ever since.

The experiments presented in this manuscript address a number of these experimental objectives: optomechanical cooling (with a technique known as feedback cooling) of a µg-scale optomechanical resonator, generation of squeezed light, both to probe the displacement of an optomechanical system in a table-top experiment, and to increase the sensitivity of large-scale GWI.

In Chapter I, I will motivate the experiments I have conducted during my PhD by presenting a general introduction to the optomechanics scene: quantum limits in continuous position measurements and their applications to GWI, how to go beyond quantum limits with squeezed light, radiation-pressure cooling...

In Chapter II, I will first present the different physical concepts used to describe the experiments I will present throughout the rest of the manuscript. This will first include classical optics and its quantum counterpart, standard optical techniques and tools, generation of squeezed light... I will also present the associated mechanical concepts: vibration modes, Fluctuation-Dissipation Theorem (FDT) and thermal position noise, QSN and QRPN, and the two techniques used to cool a mirror with radiation pressure.

The cooling experiments performed on a µg-scale optomechanical resonator will be motivated and detailed in Chapter III. This will include a description of the mechanical, optical and cryogenic systems designed, fabricated and operated to demonstrate cooling of a macroscopic mechanical resonator down to a few tens of quanta.

Chapter IV will present a different experiment: the design, fabrication and initial operation of a frequency-dependent squeezing source to demonstrate wideband sub-SQL displacement measurements of a mechanical resonator. The detailed discussion will include the laser source, the optical parametric oscillator used to generate frequency-independent squeezing, and the rotation cavity designed to extend the squeezing to frequency-dependent.

Chapter V will present the design and some experimental results I have obtained for a next-generation cryogenic optomechanical system.

I will eventually conclude the manuscript by summarizing the experimental results I have obtained and detail the next steps toward a wideband demonstration of sub-SQL measurements.

Chapter I

A panorama of optomechanics

Quantum limits in position measurements

Optical interferometers and Fabry-Perot cavities have long been been of great interest to perform high-sensitivity displacement measurements with applications in mechanical sensing, up to the challenge of gravitational-wave detection [1].

The gravitational waves detected on earth so far are caused by the coalescence of binary systems of extreme high-mass objects (black holes or neutron stars), causing an oscillation of space-time itself in the plane orthogonal to the propagation direction of the wave. These oscillations are still very small and cause a strain h which typically corresponds to an induced relative length change of only 10^{-21} or below. In a Michelson interferometer, as the gravitational wave passes through, one of the arms will be elongated while the other is compressed and vice versa as the oscillation goes (see Fig. I.1 (a)). Michelson interferometers are therefore well suited for such a detection, as one can detect a difference of optical path between the two arms. The longer the arms are, the larger the fractional (relative) change will be: for technical and budget reasons, GWI have been built with arms of kilometer length: 4 km for LIGO and 3 km for Virgo. To enhance the optical length even further, Fabry-Perot cavities have been installed in each arm (see Fig. I.1 (b)).

GWI and table-top optomechanics experiments therefore have a lot in common as in both cases, displacement (or an effective displacement in the case of a gravitational wave) is measured through the phase-shift light experiences inside the cavity, multiplied by the number of round-trips of the light beam.

In both cases, the quantum nature of light is responsible for two noises that eventually limit the measurement sensitivity as soon as classical (technical noise of the laser source, thermal displacement noise of the mirror...) is negligible. The first noise is related to the quantum phase noise of the light beam, i.e. field fluctuations perpendicular to the mean field in the complex phase-space (see Fig. I.2). This noise term is historically called *quantum shot noise* (QSN). This is direct measurement noise, that can be lowered by increasing the strength of the measurement, i.e. the laser power. Indeed, as laser power is increased, the fluctuation disk (of unit size, whatever the power is) gets further away and the phase fluctuations $\Delta\Phi$ (which correspond to the angle spread of the disk as seen from the origin of phase-space) decrease as $1/\sqrt{\langle N\rangle}$, where $\langle N\rangle$ is the average flux, i.e.

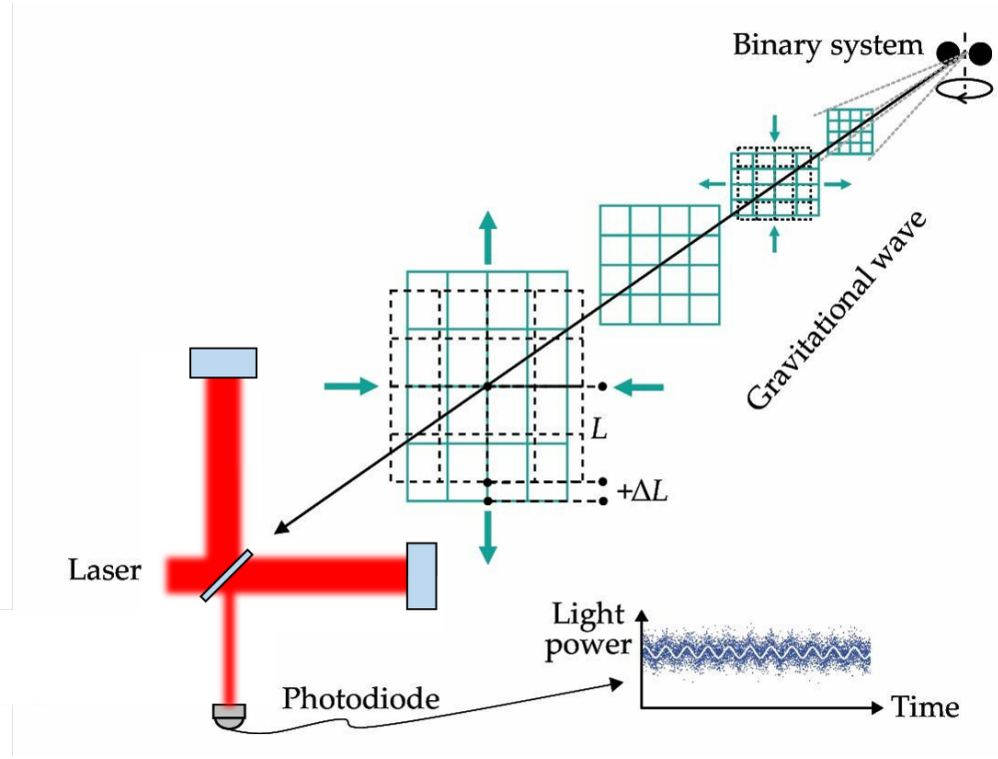

Fig. I.1 **Principle of interferometric GW detection**. *A binary system (typically neutron star or black holes) creates a gravitational wave that will travel to earth were it will cause a variation of the optical path in the two arms creating an oscillation on the amplitude measured by the photodiode. Figure adapted from [12].*

the number of photons per second in the beam.

Such a $1/\sqrt{\langle N\rangle}$ scaling law explains why advanced GWI, such as Advanced Virgo or Advanced LIGO, are operated with extreme high power CW lasers, typically with 40 W of input power for Advanced Virgo during O4, which will start next spring, and even higher power for subsequent upgrades.

But, independently of the potential issues raised by high optical power (thermal absorption...), displacement sensitivity cannot be increased at will by a mere power increase of the laser. Indeed, light also presents amplitude (and intensity) fluctuations (see Fig. I.2), and these fluctuations are imprinted onto the mirror motion by radiation pressure. Completely negligible for most experiments because of the weakness of radiation pressure (with a mean force of amplitude $\simeq 2\hbar k\langle N\rangle$, where $2\hbar k$ is the momentum impulsed to the mirror by a single photon reflection, and fluctuations of amplitude $\simeq 2\hbar k\sqrt{\langle N\rangle}$), this measurement back-action obviously increases with optical power and can become dominant for extreme values of the laser power: in such a regime, motion is actually monitored with extreme sensitivity but the detected motion is mostly representative of the intensity fluctuations of the probe laser beam, which is of little interest for displacement or weak force sensing.

To discuss this in more detail, we need to consider separately the cases of GWI and

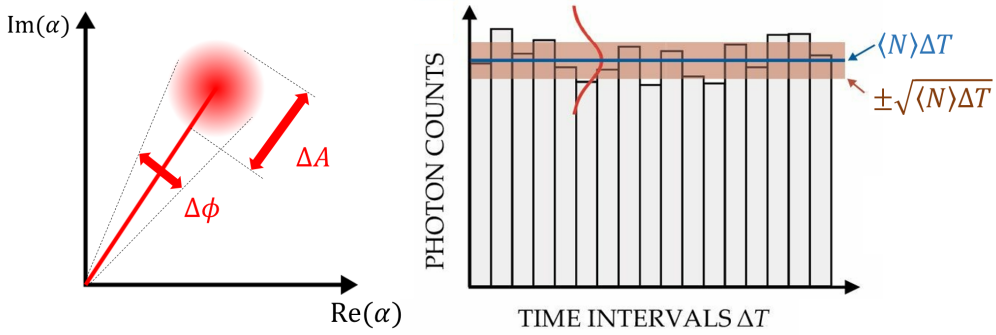

Fig. I.2 **Representations of the quantum fluctuations of a light beam**. *Left : Representation of a coherent state of light in the complex plane. The "ball" represents the fluctuations of the amplitude and phase of the field. Right : The flux of photons measured in short time intervals ΔT compared to the coherence time of light are uncorrelated and can be treated as random, independent photon events following a Poisson low, with an average value $\langle N \rangle \Delta T$ and a standard deviation $\sqrt{\langle N \rangle \Delta T}$. Figure adapted from [12].*

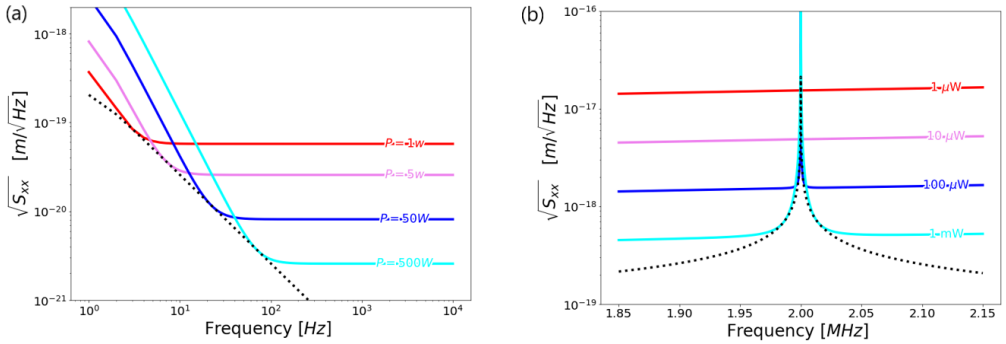

Fig. I.3 **Quantum noise in high-sensitivity displacement measurements**. *(a) Displacement noise for a GWI, for different optical powers. QRPN dominates at low frequency while QSN does at high frequency. (b) Displacement noise for an optomechanical resonator with a resonance frequency of 2 MHz and a high quality factor. QRPN dominates close to the resonance while QSN does far from the mechanical resonance. In both cases, increasing power lowers QSN but increases QRPN. The dotted lines represent the SQL.*

table-top optomechanical systems. They indeed have different length and frequency scales, which changes the exact features of quantum noise. Fig. I.3 (a) presents the quantum-limited displacement noise spectrum of two such systems over a broad frequency range. For a typical GWI, the moving mirror is a $\simeq$ 40 kg mirror suspended by a complex pendulum system, with a resonance frequency around 1 Hz. For all practical purpose, in the envisioned detection frequency band (typically 10 Hz to 10 kHz), the mirror behaves as a free mass, with a mechanical response function (also known as the mechanical susceptibility):

$$\chi(\Omega) = -1/M\Omega^2, \tag{I.1}$$

where M is the mirror mass and $\Omega/2\pi$ the frequency at which the measurement is performed. This explains the fall-off of QRPN for increasing frequency, which is the result of the $1/\Omega^2$ filtering of the intensity fluctuations (white noise) by the mechanical response. As QSN only reproduces the quantum phase fluctuations (white noise as well), QRPN dominates at low frequency while QSN does at high frequency, with a corner frequency between both regimes (where the two noises have the same magnitude), where sensitivity is optimum. As discussed above, increasing laser power lowers QSN at the expense of a higher QRPN and the corner frequency is shifted to a lower frequency.

Overall, for a coherent laser field (which presents the standard quantum fluctuations, evenly distributed on phase and amplitude (circular noise pattern, see Fig. I.2), the sensitivity is never better than the *Standard Quantum Limit* (SQL):

$$\delta x_{SQL} \simeq \sqrt{\hbar\chi} \propto 1/\Omega \tag{I.2}$$

for a GWI.

Quantum noise also limits the measurement sensitivity of micro-optomechanical systems, though in this case, experiments are usually performed close to the resonance frequency. One then has to take into account the full expression of the mechanical susceptibility:

$$\chi(\Omega) = \frac{1}{M\left(\Omega_M^2 - \Omega^2 - i\Omega\Omega_M/Q\right)}, \tag{I.3}$$

where $\Omega_M/2\pi$ is the resonance frequency and Q is the mechanical, quality factor.

Fig. I.3 (b) presents the quantum-limited displacement noise spectrum for such an optomechanical system. Here, QRPN is peaked around the resonance frequency (as is the mechanical response) while QSN is responsible for a noise floor observed at some distance of the resonance. As for the GWI case, changing the laser power lowers one noise component while increasing the other and the corresponding compromise leads again to the SQL, which is now peaked as well around the resonance frequency (as is the mechanical susceptibility). Note there are two corner frequencies evenly distributed around the resonance frequency in this case.

QSN has been rather easy to demonstrate with modern (ultrastable and low-noise) laser sources, high-finesse cavities and high-Q mirrors: it is actually the most common source for the noise floor observed far from the mechanical resonance in current optomechanics experiments. Though known on a theoretical basis since the early 1908s, QRPN has however proven very challenging because it competes with thermal noise which usually dominates for micro-scale oscillators (typically with MHz resonance frequencies),

even at cryogenic temperature. It took until 2013 for the group of C. Regal in Boulder to demonstrate QRPN for a macroscopic object (I.4) for the first time, using a very light optical membrane (see V) and a combination of conventional cryogenic cooling and radiation-pressure cooling (discussed below). Fig. I.4 presents their setup and results. The observed calibrated position noise level displays a sharp peak around the mechanical resonance frequency. For low optical power, displacement noise doesn't depend on probe power (blue spectrum and corresponding dot on the plot) as it only corresponds to thermal noise (brown curve) but for $P \gg P_{SQL}$ (where P_{SQL} is the optical power required to observe the SQL at the resonance frequency), the noise level follows a linear dependence with P (black curve) as expected for QRPN. Note in this case, the SQL could not be demonstrated because of the remaining thermal noise even at an effective temperature of 2 mK.

It is however possible to reduce QSN without increasing the optical power, by using a light beam with lower phase fluctuations, called a squeezed state (see Chap. IV). In such a beam, phase noise has been reduced by creating correlations between the photons. However, reduced QSN means, by virtue of the Heisenberg inequality, increased amplitude fluctuations, and hence of QRPN. Current GWI are not dominated by QRPN at low frequency because of some excess classical noise, so it is possible to increase their sensitivity at high frequency by using phase-squeezed states of light, as demonstrated by both LIGO and Virgo in 2019 (I.5). Here, the black curve correspond to the GW observatory sensitivity with coherent light. Using a squeezed phase state (red curve) allows to reduce the observed noise by 3 dB above 200 Hz, where QSN is dominant. Noise is unaltered at lower frequency, where classical noise dominates. The 3-dB number, only effective over a part of the detection band, and not the most critical one for the current GW source

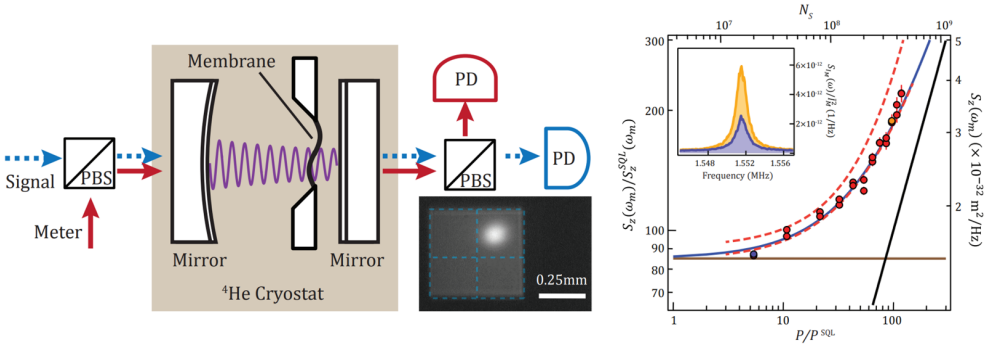

Fig. I.4 ***Experimental demonstration of of QRPN on a macroscopic object.*** *Left: experimental setup. The SiN membrane is inserted in a membrane-in-the-middle cavity. Mirror is cooled by cryogenic cooling (down to 4 K) and by radiation-pressure cooling (down to 2 mK). Insert shows the position of the optical waist and the vibration nodes of the (2,2) mechanical mode used (dashed blue lines). (Right) Dependence of the noise spectrum at resonance with normalized optical power P/P_{SQL}, with the thermal noise contribution (brown curve) and the QRPN contribution (black curve). Insert shows 2 specific noise spectra. Figure adapted from [13].*

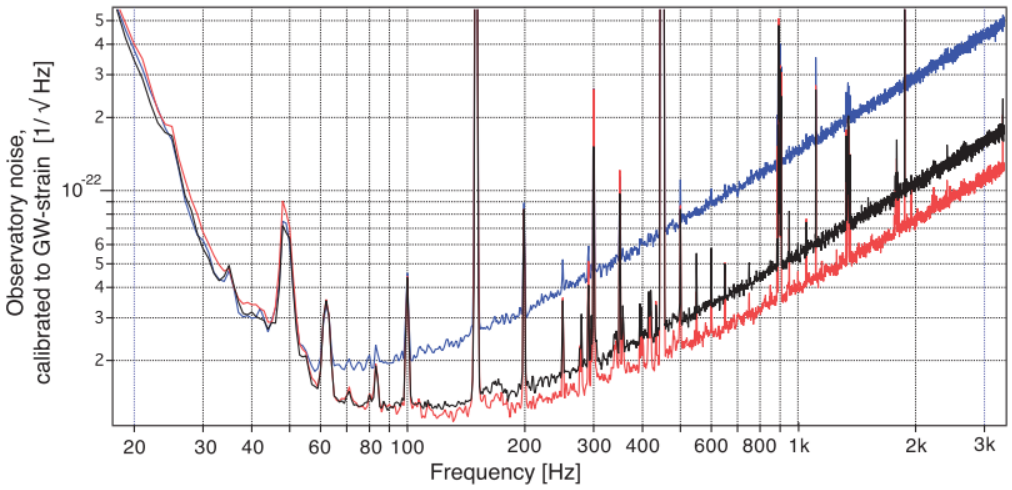

Fig. I.5 ***Impact of squeezing on the strain noise of the Advanced Virgo GWI.*** *Strain noise for a coherent state (black curve), for a phase-squeezed state (red curve) and for an amplitude-squeezed state (blue curve). Quantum noise (QSN) only limits the sensitivity at high frequency (above 200 kHz), where the sensitivity can be increased or lowered with squeezing. Figure from [14].*

considered, may seem modest considering the experimental effort involved, but it still increases the BNS (binary neutron stars) detection range by a few %. Future upgrades of the GWI will clearly strongly increase this noise reduction and its impact over the BNS range.

Using an amplitude-squeezed state (blue curve) actually increases QSN (in the same frequency band as before) as expected. The observation that the noise level is not reduced at low frequency with amplitude-squeezing confirms QRPN is mostly irrelevant for current GWI. A careful analysis of the whole set of the three noise curves actually sheds light on some QRPN, amplified by the phase-squeezed state (that displays increased intensity fluctuations), even though it is still overwhelmed by excess classical noise[15, 14]. In future observation runs, optical power will be further increased and excess classical noise reduced so the GWI will be limited by QRPN at low frequency. We will see in Chapter IV that it is actually possible to take advantage of the different frequency dependence of these two quantum contributions to the sensitivity curve to reduce both QSN (at high frequency) and QRPN (at low frequency) to increase the quantum-limited sensitivity of GWI over a broad frequency range.

Optomechanics and the Quantum Ground State challenge

Optomechanics has been founded within the fields of ultrasensitive displacement measurement or GW detection. In such contexts, mirror motion mostly appears as an additional noise source (QRPN) but optomechanics also offers essential tools to demonstrate a long-standing goal of experimental physics: demonstrating the quantum ground state (QGS) of a macroscopic mechanical resonator.

Two conditions have to be fulfilled for such an experiment:

- the mechanical resonator has to be in its QGS, which means its thermal energy has to be negligible compared to the quantum of energy: $k_B T \ll \hbar\Omega_M$,
- the experiment has to be sensitive enough to probe the corresponding position fluctuations.

Optomechanics obviously meets the second requirement: typical table-top experiments have demonstrated sensitivities at the level of $10^{-18}\,\mathrm{m}/\sqrt{\mathrm{Hz}}$ or better in the MHz range, while for typical nm-scale resonators, the zero-point position fluctuations level can be as high as $10^{-16}\,\mathrm{m}/\sqrt{\mathrm{Hz}}$.

However, using optical sensing (especially in free space) usually sets a lower limit to the size of the mechanical resonators under consideraton, and hence to their resonance frequency. Optomechanical systems have long been limited to a few tens of MHz at most, while, even at dilution fridge temperatures ($\simeq 10$ mK), $k_B T \ll \hbar\Omega_M$ implies a resonance frequency in the GHz band. But optomechanics actually offers some alternatives, in the form of at least two cooling mechanisms that have the ability to effectively cool a mechanical resonator well below its environment temperature, and allow to meet the temperature requirement.

A first technique, known as *cold damping* or *feedback cooling* uses the sensitivity of optical interferometry to probe the resonator motion and use the displacement signal in real-time to drive an additional force (for example through the amplitude modulation of an additional feedback laser beam) to increase the mechanical damping of the resonator without any additional fluctuations. This process was first demonstrated in a high-sensitivity experiment in the optomechanics team at LKB in 1999 [11], to cool the vibration motion mode of the mirror from room temperature down to about 10 K (see Fig. I.6).

Another technique only uses a single laser beam, in close analogy to atomic physics. Indeed, the generic optomechanical system presented in the introduction (spring-loaded mirror) presents some similarities with an atom pumped close to an atomic transition. In some well-designed experimental conditions, a photon (with a frequency slightly lower than the atomic resonance frequency) incident on an atom can absorb some kinetic energy during the process. As a result of many such interactions, the mean kinetic energy of an assembly of atoms, and their temperature, can be significantly lowered.

Similarly, a photon incident into the cavity with a frequency slightly lower than its resonance frequency, can preferentially absorb phonons of the moving mirror to increase its energy and reach the cavity resonance frequency. So "pumping" the cavity with "red-detuned" light, may extract energy from the mirror motion and cool it. This technique is known as sideband cooling, and was first demonstrated independently by the LKB group [16] and by M. Aspelmeyers' group in Vienna [17] in 2006.

These proof-of-concept experiments, both for feedback cooling and sideband cooling, only demonstrated cooling from room temperature down to 10 K, but combining cryogenic cooling (down to 100 mK or below for example, in a dilution fridge) with either feedback

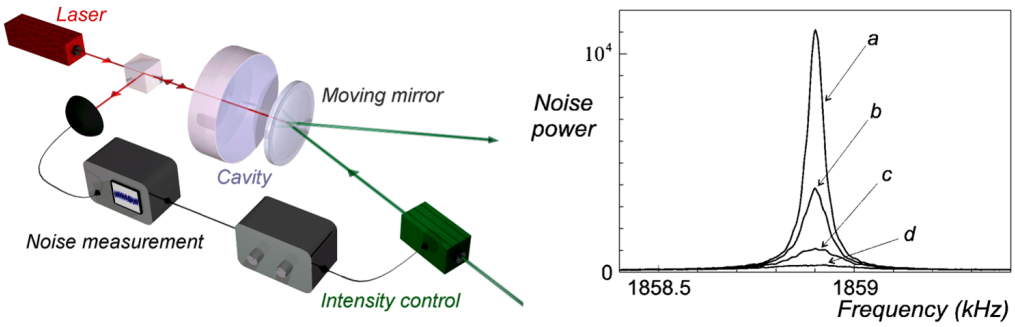

Fig. I.6 ***First feedback cooling experiment performed at LKB.*** *Left: Experimental setup. The field reflected by the cavity is used to probe the mirror position. An auxiliary laser beam, reflected on the end mirror, is used to apply a feedback force on the mirror and counter the Brownian noise. Right. Thermal noise spectrum of the mirror without feedback (a) and with increasing feedback gains (b) to (d).*

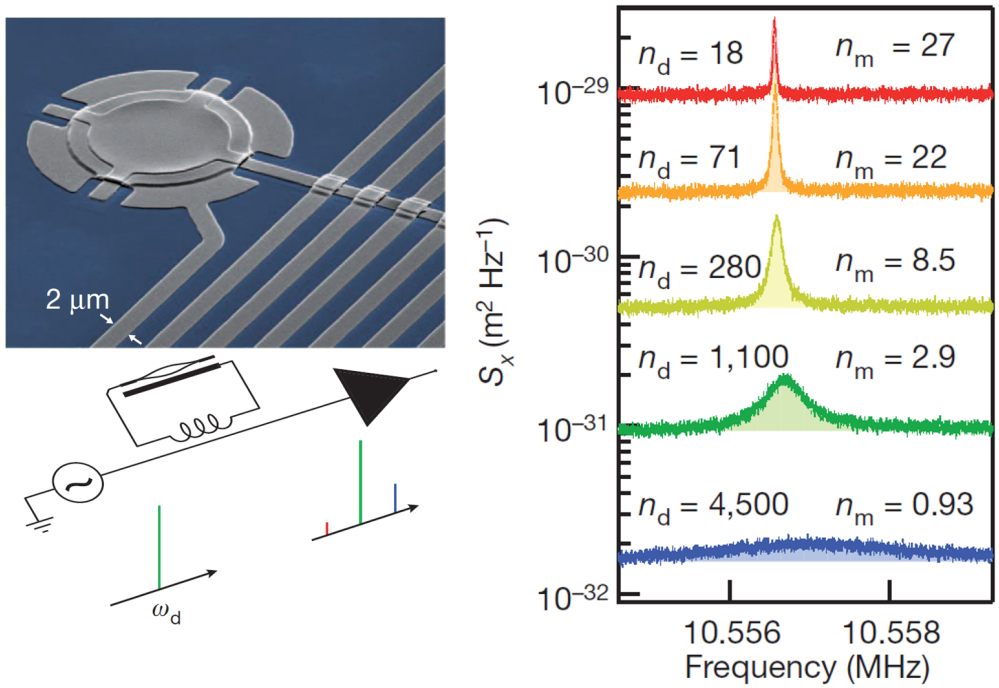

Fig. I.7 ***First experimental demonstration of an optomechanical system cooled close to its quantum ground state.*** *Left: experimental setup and effective electrical circuit. The resonator is a 15-µm-diameter aluminum plate suspended 50 nm above a lower electrode. The microwave drive at ω_d (green carrier) is scattered to a Stokes band (red) and an anti-Stokes band (blue). The detuning creates an imbalance between the two bands, which cools the drum resonator. Right: thermal noise spectrum as the drive power (n_d) is increased. The corresponding temperature is expressed in terms of mechanical phonons (n_m). Figure adapted from [10].*

or sideband cooling immediately appeared as a very promising idea to reach effective temperatures in the µK range and demonstrate QGS cooling.

The first demonstration of QGS cooling was performed by J. Teufel and his collaborators in 2011, with a 15-µm-diameter aluminum plate as optomechanical resonator [10]. The plate was suspended 50 nm above a lower electrode, with the drum motion modulating the capacitance of a LC circuit (visible on the bottom left of Fig. I.7). This resonating circuit is equivalent to an optical cavity, but in the GHz range. For a detuned resonator, the anti-Stokes sideband is favoured over the Stokes band, and the net effect of the microwave drive is a damping and cooling effect, as can be seen on the experimental noise spectra: the thermal noise spectrum both widens and gets lower as the drive power (expressed in terms of number n_d of drive microwave photons) is increased. Such a cooling experiment has now been performed with many different systems, and the QGS has been characterized not only by a quantitative feature such as the position noise level, but with striking qualitative aspects such as sideband asymmetry as well [18]. Quantum mechanical motion has also been since then extended to other non-classical states such as mechanical squeezed states, light-mechanics entangled states or entangled states between two mechanical resonators.

Optomechanics, a field of its own

Optomechanics has experienced a tremendous growth for the past 15 years or so, with Hundreds of research articles have been published, with a whole zoology of experimental platforms (see Fig. I.8): micro-mirrors, micro-toroids, nano-membranes, photonic crystals, microwave circuits, cold atoms, trapped nanoparticles... Optomechanical resonators cover a huge range in mass, from fg for a silicon nanoparticle to 40 kg for a GWI suspended mirror, and in frequency, from 1 Hz for the GWI pendulum motion to the GHz band for photonic-crystal nanowires. Starting from quantum-limited displacement sensing and the experimental quest for the QGS, the two topics I will cover in this thesis, optomechanics now has applications in fields as diverse as weak measurement, GW detection, experimental stochastic thermodynamics (by probing thermal motion in real-time and monitoring the fluctuations of thermodynamic quantities), biophysics (by monitoring mechanical properties of specific resonators, which depend on a virus adsorption on its surface...), quantum thermodynamics, quantum information (for microwave-to-optics conversion of quantum states, or by taking advantage of the extreme values of Q for quantum memory applications)...

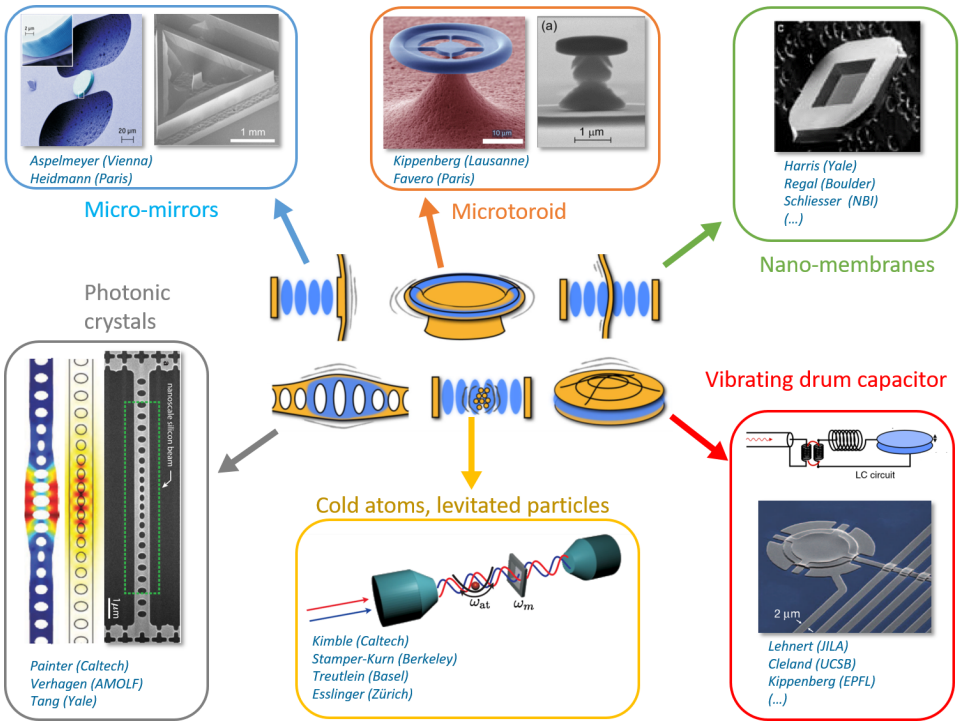

Fig. I.8 ***The zoology of optomechanical systems.*** *Demonstrated optomechanical systems can be summarized in different geometries, such as micro-mirrors [19, 20], micro-toroids [21], nano-membranes [22, 13, 23, 24, 25], photonic crystals [26, 27, 28], microwave circuits [29, 30, 31], cold atoms [32, 33, 34, 35, 36], trapped nano-particles [37, 38, 36]... The corresponding vibration modes are represented by the gray lines while the electromagnetic energy is represented in blue. Figure adapted from [39].*

Chapter II

Theory

In this chapter, I will introduce the fundamental theoretical notions needed to understand and analyse the experiments presented in this thesis. The first 4 sections describe the optical concepts and tools used throughout the manuscript: classical description of the optical field, properties and characterization of Fabry-Perot cavities, quantum description of light, and the implementation of $\chi^{(2)}$ nonlinear mechanisms required to generate squeezed light.

In Section II.5, I introduce specific optomechanical concepts: radiation-pressure coupling between the displacement and the optical field, the fluctuation-dissipation theorem and thermal noise spectrum, quantum phase noise in continuous position measurement, quantum radiation pressure noise (QRPN) and the corresponding standard quantum limit (SQL).

Section II.6 deals with another aspect of tabletop optomechanics, which is the ability to use the extreme sensitivity of optical sensing combined with radiation pressure to probe the displacement of a mesoscopic mechanical resonator and to cool its thermal motion by two techniques: sheer radiation pressure (self-)cooling using the probe beam inside an optical cavity and (feedback) cooling using the probe beam to modulate the radiation pressure of a second beam. Both techniques have been used to demonstrate cooling down close to the quantum ground state with a number of experimental platforms, mostly sub-µm and nm-scale optomechanical resonators.

II.1 Classical description of the optical field : the electric field of a Gaussian beam

In this work, we will only consider TEM_{00} Gaussian modes of the electric field to represent our laser beam. Higher-order transverse modes are, of course, present in the experiment, but they mostly appear as mode-matching defects and optical losses, so we will not describe them in detail, even though we obviously take them into account in the discussion.

We will also assume a monochromatic (at frequency $\omega_L/2\pi$, with the corresponding wavevector $k = \omega_L/c$) and linearly polarized field, so we can write the complex field $\vec{E}$ as:

$$\vec{E}(x, y, z, t) = \alpha(t) e^{i\omega_L t} E(x, y, z)\hat{p} + \text{c.c}, \tag{II.1}$$

where $\alpha(t)$ is the slow time-varying field envelope, $\hat{p}$ is the unitary polarization vector (orthogonal to the direction of propagation along the z-axis) and

$$E(x,y,z) = E_0 \frac{w_0}{w(z)} exp\left(-\frac{x^2+y^2}{w(z)^2}\right) \exp\left(-ikz - ik\frac{x^2+y^2}{2R(z)} + i\psi_G(z)\right) \tag{II.2}$$

where E_0 is the complex amplitude and the interesting geometric parameters of the Gaussian beam are represented on Figure II.1:

- $w(z)$ is the local waist of the laser beam
- w_0 is the minimum waist (at the focus point)
- $R(z)$ is the local radius of curvature
- $\psi_G(z)$ is the Gouy phase.

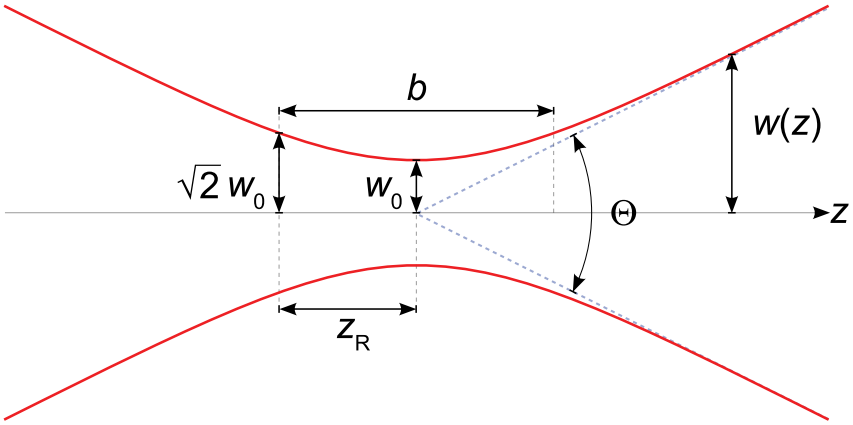

Fig. II.1 *Representation of a Gaussian beam with a waist w_0. Figure from [40]*

II.2 The Fabry-Perot cavity

During the course of my PhD work, optical cavities have been essential tools to probe mechanical displacements of course, but also to stabilize and filter laser sources, generate (frequency-doubled) green light and then create squeezed light by pumping an optical parametric oscillator with green light.

II.2.1 Dynamics of the field

Let us a consider a simple linear Fabry-Perot cavity represented on the figure II.2 where we represented the following optical fields:

- the incident field α_{in}
- the intra-cavity field propagating from left to right α and the counter-propagating field α'

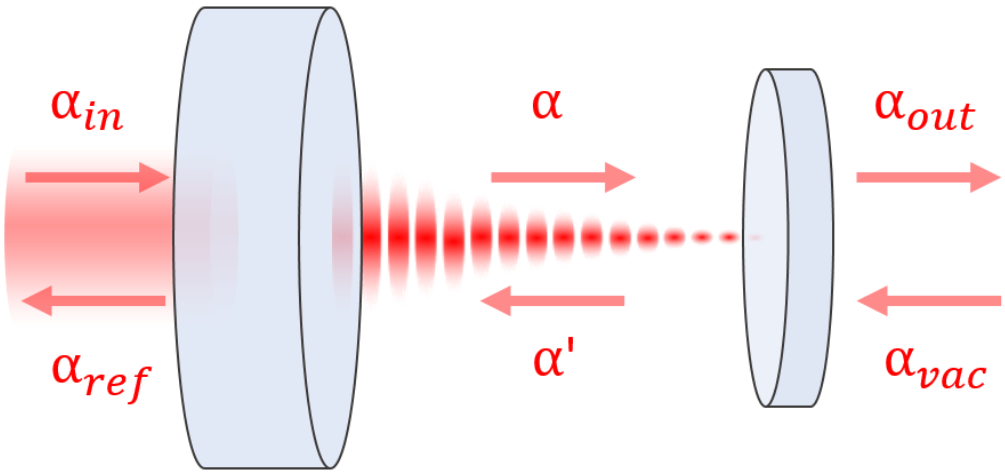

Fig. II.2 *Representation of the various fields interacting with a Fabry-Perot cavity*

- the reflected field α_{ref}
- the transmitted field α_{out}, which is non-zero only in the presence of a residual transmission of the end mirror. In our cavity geometry, we are usually only able to detect the reflected field, so we will use this field to model the optical losses.
- a possible additional field (incident from the right), that we will only take into account as Vacuum fluctuations (see the following section II.3 on the quantum description of the light beam) α_{vac}

Let us note T and P the intensity transmission coefficients of the input mirror and the end mirror. If we neglect the absorption in the mirrors, their reflection coefficients can be written as $1-T$ and $1-P$. We can write the following equations for the fields at the input mirror position ($x=0$) and at the output mirror position ($x=L_{cav}$) :

$$\alpha(x=0,t) = \sqrt{T}\alpha_{in}(t) + \sqrt{1-T}\alpha'(x=0,t) \tag{II.3}$$
$$\alpha_{ref}(t) = \sqrt{T}\alpha'(x=0,t) - \sqrt{1-T}\alpha_{in}(t) \tag{II.4}$$
$$\alpha'(x=L_{cav},t) = \sqrt{P}\alpha_{vac}(t) + \sqrt{1-P}\alpha(x=L_{cav},t) \tag{II.5}$$
$$\alpha_{out}(t) = \sqrt{P}\alpha(x=L_{cav},t) - \sqrt{1-P}\alpha_{vac}(t) \tag{II.6}$$

We will write $\psi(t) = 2kL_{cav}(t)$ the phase-shift acquired by the optical field over a single round-trip inside the cavity and $\tau = 2L_{cav}(t)/c$ the duration of such a round trip. We can now write

$$\alpha'(x=L_{cav},t) = \alpha'(x=0,t+\tau/2)e^{-i\frac{\psi}{2}} \tag{II.7}$$
$$\alpha(x=L_{cav},t) = \alpha(x=0,t-\tau/2)e^{i\frac{\psi}{2}}. \tag{II.8}$$

If we now consider a high-finesse cavity ($T + P \ll 1$) close to the optical resonance ($\psi \approx 2n\pi$, where n is an integer), we can make the following approximations:

$$e^{-i\frac{\psi}{2}} \approx 1 - i\frac{\psi}{2} \tag{II.9}$$

and

$$\sqrt{1-T} \approx 1 - \frac{T}{2} \tag{II.10}$$

$$\sqrt{1-P} \approx 1 - \frac{P}{2} \tag{II.11}$$

$$\sqrt{1-T}\sqrt{1-P} \approx 1 - \frac{T+P}{2}. \tag{II.12}$$

And we can write using II.3,II.5,II.8 and II.7.

$$\frac{\alpha(t+\tau) - \alpha(t)}{\tau} = \left(i\frac{\psi}{\tau} - \frac{\kappa}{2}\right)\alpha(t) + \sqrt{\frac{\kappa_{in}}{\tau}}\alpha_{in}(t) + \sqrt{\frac{\kappa_0}{\tau}}\alpha_{vac}(t) \tag{II.13}$$

with

$$\kappa = \frac{T+P}{\tau} \tag{II.14}$$

$$\eta = \frac{T}{T+P} \tag{II.15}$$

$$\kappa_{in} = \frac{T}{\tau} = \eta\kappa \tag{II.16}$$

$$\kappa_0 = \frac{P}{\tau} = (1-\eta)\kappa \tag{II.17}$$

$$\tag{II.18}$$

where

- κ is the cavity bandwidth also known as the decay rate of the cavity and can be seen as the inverse of the average lifetime of a photon inside the cavity.
- η is the quantum efficiency of the cavity i.e., the ratio of photons that have interacted with the cavity and that are sent back to the reflected field and that you can actually measure.
- κ_{in} is the coupling rate to the input field, and κ_0 is the coupling rate to the output vacuum. Note that $\kappa = \kappa_{in} + \kappa_0$.

We can now approximate the left term of equation II.13 as the derivative of $\alpha(t)$ (which is valid if the round-trip time τ is negligible compared to the time scale of the mirror motion) and we get :

$$\dot{\alpha}(t) = \left(-\frac{\kappa}{2} + i\psi/\tau\right)\alpha(t) + \sqrt{\frac{\kappa_{in}}{\tau}}\alpha_{in}(t) + \sqrt{\frac{\kappa_0}{\tau}}\alpha_{vac}(t). \tag{II.19}$$

II.2.2 The input-output relations

In the Fourier domain, equation II.19 becomes

$$\left(\frac{\kappa}{2} - i\psi/\tau + i\Omega\right)\alpha[\Omega] = \sqrt{\frac{\kappa_{in}}{\tau}}\alpha_{in}[\Omega] + \sqrt{\frac{\kappa_0}{\tau}}\alpha_{vac}[\Omega], \tag{II.20}$$

which is known as the input relation. It is also worth writing the output relation that will be useful for future calculation :

$$\alpha_{out}[\Omega] = \sqrt{\kappa_0\tau}\alpha[\Omega]\,(1 + i\psi/2 + i\Omega\tau/2) - \alpha_{vac}[\Omega]. \tag{II.21}$$

If we now take again equation (II.19), and only consider the 0^{th} order static term at resonance, we get:

$$\bar{\alpha} = \frac{2}{\kappa}\sqrt{\frac{\kappa_{in}}{\tau}}\bar{\alpha}_{in} \tag{II.22}$$

$$\bar{\alpha}_{out} = \sqrt{\kappa_0\tau}\bar{\alpha}, \tag{II.23}$$

which can be written in terms of laser intensity as

$$I = \frac{4}{\kappa^2}\frac{\kappa_{in}}{\tau}I_{in} = \frac{2}{\pi}\eta\mathcal{F}I_{in} \tag{II.24}$$

$$I_{out} = 4\eta(1-\eta)I_{in}. \tag{II.25}$$

The average intracavity power is just the input intensity amplified by the finesse of the cavity (η being usually around unity).

II.2.3 The reflection coefficient near resonance

We now want to compute the reflection coefficient $r(\Omega) = -\alpha_{ref}/\alpha_{in}$ that corresponds to the response of the optical cavity. From equation II.4 and II.5, neglecting the vacuum fluctuations and in the high finesse approximation, we get

$$\alpha_{ref}[\Omega] = \sqrt{\frac{\kappa_{in}}{\tau}}\alpha[\Omega] - \alpha_{in}[\Omega] \tag{II.26}$$

$$= \left(\frac{\kappa_{in}}{\tau}\frac{1}{\kappa/2 - i(\psi/\tau - \Omega)} - 1\right)\alpha_{in}[\Omega] \tag{II.27}$$

in the Fourier domain. We now consider a cavity where the phase-shift is only due to a constant detuning: $\Delta\omega = \omega_L - \omega_{cav} = \psi/\tau$ and we can now write $r[\Omega]$ as

$$r(\Omega) = 1 - \frac{2-\epsilon}{1 + i\xi(\Omega)} = \frac{\epsilon - 1 + i\xi(\Omega)}{1 + i\xi(\Omega)}, \tag{II.28}$$

where

$$\epsilon = \frac{2P}{T+P} = \frac{2\kappa_0}{\kappa} \tag{II.29}$$

and

$$\xi(\Omega) = \frac{\Omega - \Delta\omega}{\kappa/2}. \tag{II.30}$$

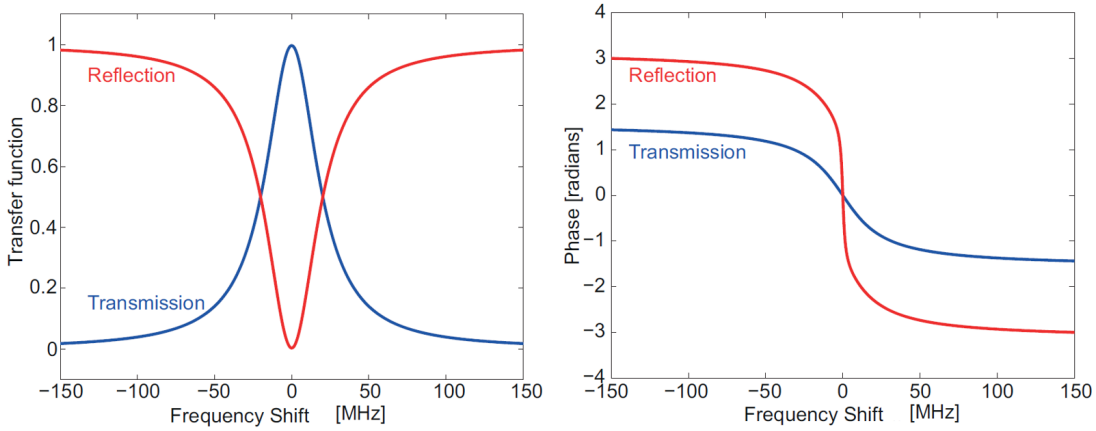

Fig. II.3 *Amplitude and phase transfer functions of an optical cavity in reflection and transmission. Cavity parameters chosen are* $L_{cav} = 1\ m$, $\lambda = 1\ \mu m$, $T = 0.005$ *and* $P = 0.04$. *(Courtesy of Sheon Chua).*

We can now compute the magnitude of this transfer function and we get

$$|r(\Omega)|^2 = 1 - \frac{(2-\epsilon)\epsilon}{1+\xi^2(\Omega)}. \tag{II.31}$$

We can see that, as we slowly sweep the cavity detuning (by sweeping either the cavity length or the laser frequency), we will get a reflexion coefficient for the mean field (corresponding to $\Omega = 0$) with a Lorentzian dip of Full Width at Half Maximum (FWHM) κ.

The simplified expression for the reflection coefficient will be particularly useful to compute the effect of the rotation cavity on a squeezed state (see section II.5.5 of this chapter). It can also be useful to note the value of the cavity reflection and transmission coefficients at zero detuning and in terms of P and T :

$$R_{res} = (1-\epsilon)^2 = \left(\frac{T-P}{T+P}\right)^2 \tag{II.32}$$

and

$$T_{res} = 1 - R_{res} = 1 - (1-\epsilon)^2 = \epsilon(2-\epsilon) = \frac{4PT}{(T+P)^2}. \tag{II.33}$$

II.2.4 Filtering property of a cavity

It is also interesting to note that the transmission coefficient can be written as

$$|t(\Omega)|^2 = 1 - |r(\Omega)|^2 = \frac{(2-\epsilon)\epsilon}{1+\xi^2(\Omega)}, \tag{II.34}$$

At resonance (zero-detuning: $\Delta\omega = 0$), the transmitted field of the cavity is low-pass filtered with a cut-off frequency $\kappa/2\pi$. This property will be taken advantage of for the

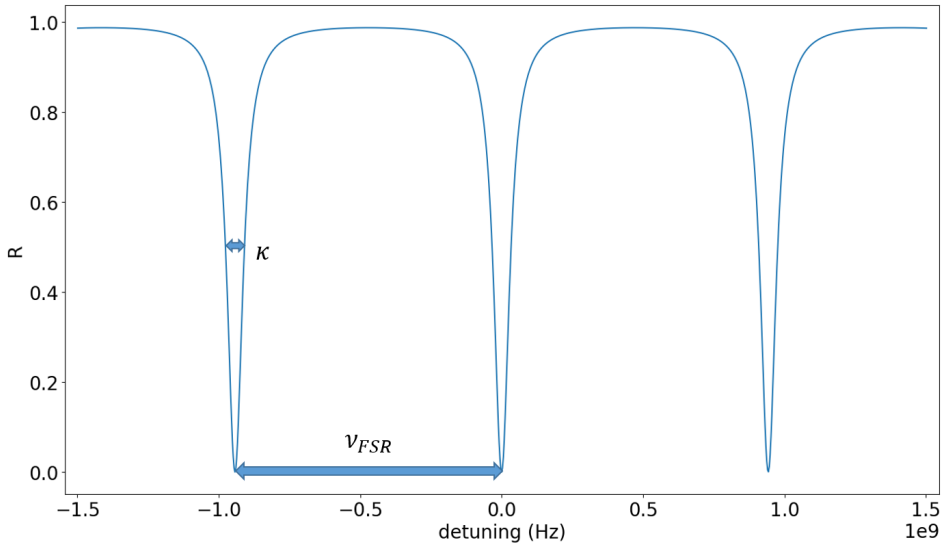

Fig. II.4 ***Reflection of a cavity as a function of frequency detuning.*** *The Free Spectral Range (FSR) corresponds to the frequency interval between two peaks, the cavity bandwidth at the Full width at half maximum of the peak and the finesse as the ration between the two. Here we have a cavity with* $T = P = 0.2$ *and* $L_{cav} = 1$ *m, so* $\nu_{FSR} = 150$ *MHz,* $\kappa = 2\pi \times 9.5$ *MHz and* $\mathcal{F} = 15.7$.

Mode Cleaner infrared cavity (MCIR) IV.3, a high-finesse cavity through which we send the bright field delivered by the laser source to get rid of most of the classical noise of the laser.

II.2.5 Optical characterization of a cavity

To actually measure the transmission coefficient of our cavity mirrors T and P, we can measure the peak near resonance and extract $\kappa = \frac{T+P}{\tau}$. If we know precisely our cavity length, we can compute $T + P = \frac{\kappa}{c/(2L)}$ and by measuring R_{res} we can get $|T - P| = (T + P)\sqrt{R_{res}}$. This method doesn't allow us to distinguish between T and P but we usually have quite a good estimation of these values, which are provided by the manufacturer of the coatings.

If we don't know precisely the length, we can look at the reflection response of the cavity as a function of the laser detuning for a quasi-static sweep ($\Omega = 0$). We see on figure II.4 equally separated resonance peaks corresponding to the cavity resonant condition where $L_{cav} = n\lambda/2$ with n an integer and we can define $\nu_{FSR} = \frac{c}{2L}$, the Free Spectral Range (FSR) of the cavity as the frequency difference between two resonant frequencies.

We call $\mathcal{F}$ the cavity finesse:

$$\mathcal{F} = \frac{\omega_{FSR}}{\kappa} = \frac{2\pi}{T+P} \approx \frac{\text{average lifetime of a photon inside the cavity}}{\text{round trip duration}}. \tag{II.35}$$

It is a unit-less number corresponding (up to a π factor) to the average number of round trips made by a photon inside the cavity. If one is able to measure the reflection over a few resonances, calibrating the horizontal axis in frequency is not required, as one just needs the ratio between the distance between two consecutive resonances and their width to compute the finesse.

Then you have, for $P < T$:

$$T = \frac{\pi(1+\sqrt{R_0})}{\mathcal{F}} \tag{II.36}$$

$$P = \frac{\pi(1-\sqrt{R_0})}{\mathcal{F}} \tag{II.37}$$

Note that these results assume a perfect mode matching of the cavity which can be difficult to achieve, but they still give quite a good estimation of the transmission coefficients of the mirrors. One also has to keep in mind that P accounts for the output mirror transmission as well as for the losses inside the cavity, which can be caused by beam clipping, mirror imperfections, etc... So comparing the measured value of P with the specified transmission provides an estimation of the excess losses inside the cavity. This calculation also assumes a High-Finesse cavity which is the case for all the cavity described in this PhD apart from the OPO who has a measured finesse of 9 at 532 nm. In the general case, the finesse for an optical cavity is given by

$$\mathcal{F} = \frac{\pi(R_1 R_2)^{\frac{1}{4}}}{1-\sqrt{R_1 R_2}} \tag{II.38}$$

where R_i is the power reflectivity of mirror number i. A complete characterization of the optical cavities used in the experiments discussed in this manuscript can then be obtained by performing a full set of measurements of the various coefficient presented in this section. These characteristics are essential to properly fit and analyze the experimental spectra and results presented in this manuscript.

II.3 Quantum description of the optical field

Continuous position sensing with a high-finesse optical cavity probed by a laser can reach an extreme sensitivity, typically at the $10^{-18}\,\mathrm{m}/\sqrt{\mathrm{Hz}}$ level and below. Such a sensitivity can be achieved with a low-noise highly stable laser source and is only limited by the quantum fluctuations of the light beam.

This section presents the theoretical tools required to compute and manipulate quantum noise in optics experiments. As even very low power lasers correspond to intense beams in terms of the number of photons per second (typically, at 1064 nm, a very weak beam of 1 µW already amounts to 3.10^{12} photons per second), the following model considers and manipulates quantum fluctuations as classical stochastic variables (similar to classical fluctuations, only their origin being quantum). Such a semi-classical formalism is, however, well adapted to the experiments described here and allows a simple mapping from the previous classical description of light to its quantum counterpart.

II.3.1 Quantization of the optical field

If we set $E_0 = \sqrt{\frac{2\hbar\omega_L}{\epsilon_0 c\pi w_0^2}}$, and we compute the optical power carried by the time-average of the field by integrating the Poynting vector over the (xy) plane, we get

$$P = \frac{\epsilon_0 c}{2}\iint \langle E\rangle^2 \mathrm{d}S = \frac{\epsilon_0 c}{2}E_0^2\,|\alpha(t)|^2\,\pi w_0^2 = \hbar\omega_L\, I(t), \tag{II.39}$$

where $I(t) = |\alpha(t)|^2$. We can clearly see that $I(t)$ corresponds to the average flux (number of photons flowing through a surface per unit of time) of photons of energy $\hbar\omega_L$. From now on we will only consider the dynamic of $\alpha(t)$, which contains all the useful information about the beam. If we want to really look at the quantized field, we have to replace the complex field amplitude α and its complex conjugate α^* by the annihilation operator $\hat{a}$ and its complex conjugate, the creation operator $\hat{a}^\dagger$, with the commutations relations :

$$[\hat{a}(t), \hat{a}(t')] = [\hat{a}^\dagger(t), \hat{a}^\dagger(t')] = 0 \quad \text{and} \quad [\hat{a}(t), \hat{a}^\dagger(t')] = \delta(t-t'). \tag{II.40}$$

II.3.2 Amplitude and phase modulations and their representations

To describe quantum fluctuations of the beam at an angular frequency $\Omega\,(\ll \omega_L)$, one has to take into account quantum modes at $\omega_L \pm \Omega$. Here, I first recall some basic properties of amplitude and phase modulations, that will be used for the quantum noise description as well.

If one considers a classical field $E(t)$ undergoing an amplitude modulation at a frequency $\Omega_m \ll \omega_L$:

$$E(t) = E_0(1 + m\cos(\Omega_m t))e^{i\omega_L t} = E_0\left[1 + \frac{m}{2}(e^{i\Omega_m t} + e^{-i\Omega_m t})\right]e^{i\omega_L t} \tag{II.41}$$

$$= E_0\left[e^{i\omega_L t} + \frac{m}{2}e^{i(\omega_L+\Omega_m)t} + \frac{m}{2}e^{i(\omega_L-\Omega_m)t}\right]. \tag{II.42}$$

We see that the resulting field is the sum of three waves : the carrier at the natural frequency ω_L and the two side bands at $\omega_L \pm \Omega_m$. We can represent those three fields in the "sideband diagram", but we can also represent $\alpha(t) = (1 + m\cos\Omega_m t)$ on the "phasor diagram" on the figure (II.5).

We can do the same thing for a phase-modulated field where we assume a small modulation ($m \ll 1$) and we can write :

$$E(t) = E_0 e^{i[\omega_L t + m\cos(\Omega_m t)]} \approx E_0\left[1 + i\frac{m}{2}(e^{i\Omega_m t} + e^{-i\Omega_m t})\right]e^{i\omega_L t} \tag{II.43}$$

$$= E_0\left[e^{i\omega_L t} + i\frac{m}{2}e^{i(\omega_L+\Omega_m)t} + i\frac{m}{2}e^{i(\omega_L-\Omega_m)t}\right]. \tag{II.44}$$

We get more or less the same result but this time the sidebands are complex so we now consider the sideband diagram as a 3D plot where the x-axis is the frequency and for each of this frequency we construct a complex plane where we represent our

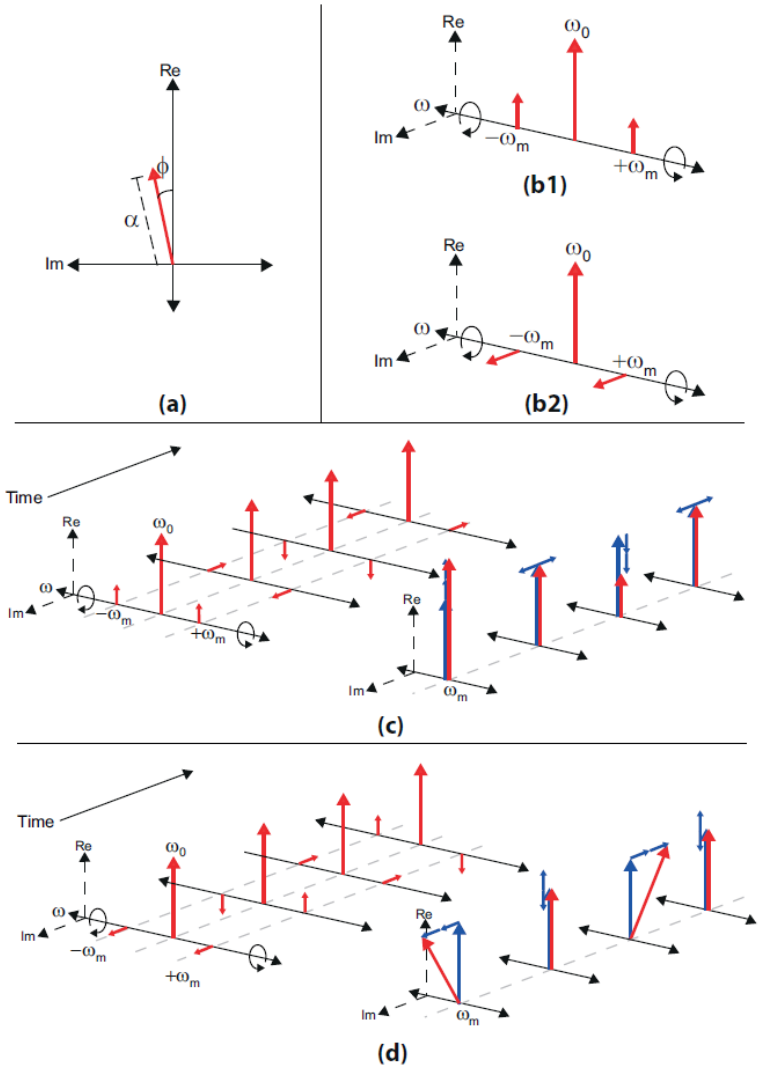

Fig. II.5 **Modulations as beat notes between a carrier and sidebands**. *(a) The classical "phasor diagram" where α is represented on the complex plane. (b) The classical "sideband diagram" where the three fields are represented at $t = 0$ for amplitude modulation (b1)(II.41) and phase modulation (b2) (II.43). (c) Time evolution of the amplitude sideband modulation in the rotating frame: the carrier is static but the two sidebands rotate at the same frequency but in opposite directions (at $\pm\omega_m$). On the right, we see the result in the phasor diagram. (d) Time evolution of the phase-modulation sidebands and resulting phasor evolution. The modulation effect has been exaggerated for clarity and we see that the approximation that the amplitude remains constant starts to break. Figure from [41].*

sidebands. The phasor diagram becomes the representation in the complex plane of $\alpha(t)$. Any modulation or noise at frequency Ω can thus be represented as two sidebands at $\pm\Omega$ and all the information about this noise is contained in their amplitudes and phase relationships with the carrier.

II.3.3 One-photon formalism

If we now want to represent the actual vacuum quantum fluctuations of the light, we will write the field amplitude as a sum over all frequencies Ω of the two sidebands at $\pm\Omega$. The expression of the time-varying part of the electromagnetic field $E(t)$ displays its audio-side band components around the carrier frequency ω_0:

$$a(t) = \int_0^{+\infty} \frac{\mathrm{d}\Omega}{2\pi} \left[a_+[\Omega] e^{-i\Omega t} + a_-^*[\Omega] e^{i\Omega t} \right], \tag{II.45}$$

where $a_\pm(\Omega)$ are the normalized amplitudes of the upper and lower side bands at frequencies $\omega_L \pm \Omega$ and are just a decomposition of the usual Fourier coefficients at positive and negative frequencies. On the sideband diagram, we now have to imagine an infinite number of sidebands and the phase diagram can be represented with the "ball on a stick picture" where fluctuations are represented by a ball of radius unity on top of a stick representing the mean value of the coherent field (see figure II.6)

II.3.4 Displaced frame

In the experiment described in this manuscript, we often deal with bright optical field of at least a few nW, corresponding to a flux of photons of $\approx 10^{10}$ photons/sec. So we will only use the quantum description of the field for the fluctuation part and write $\hat{a}(t) = \bar{a} + \delta\hat{a}(t)$. The bandwidth of our detector being much smaller than ω_L, what we measure is the average over one or more cycles of the electromagnetic wave, so the measurable intensity is :

$$< I(t) > \propto < E(t)^2 > = |\bar{a} + \delta a(t)|^2 \approx |\bar{a}|^2 + 2\,\mathrm{Re}[\bar{a}^* \delta a(t)], \tag{II.46}$$

where we average to zero the terms oscillating at $2\omega_L$ and neglect the term in $|\delta a(t)|^2$ since $\delta a(t) \ll \bar{a}$. So the power fluctuations can be written as

$$\delta I(t) = 2\,\mathrm{Re}[\bar{a}^* \delta a(t)]. \tag{II.47}$$

Now taking the Fourier transform we get :

$$\delta I[\Omega] = \int_{-\infty}^{+\infty} 2\,\mathrm{Re}[\bar{a}^* \delta a(t)] e^{i\Omega t} \mathrm{d}t \tag{II.48}$$

$$= \int_{-\infty}^{+\infty} [\bar{a}^* \delta a(t) + \bar{a} \delta a^*(t)] e^{i\Omega t} \mathrm{d}t \tag{II.49}$$

$$= \bar{a}^* \delta a_+[\Omega] + \bar{a} \delta a_-^*[\Omega], \tag{II.50}$$

where we used the definition of $\delta a(t)$ to compute the Fourier transform in the final step.

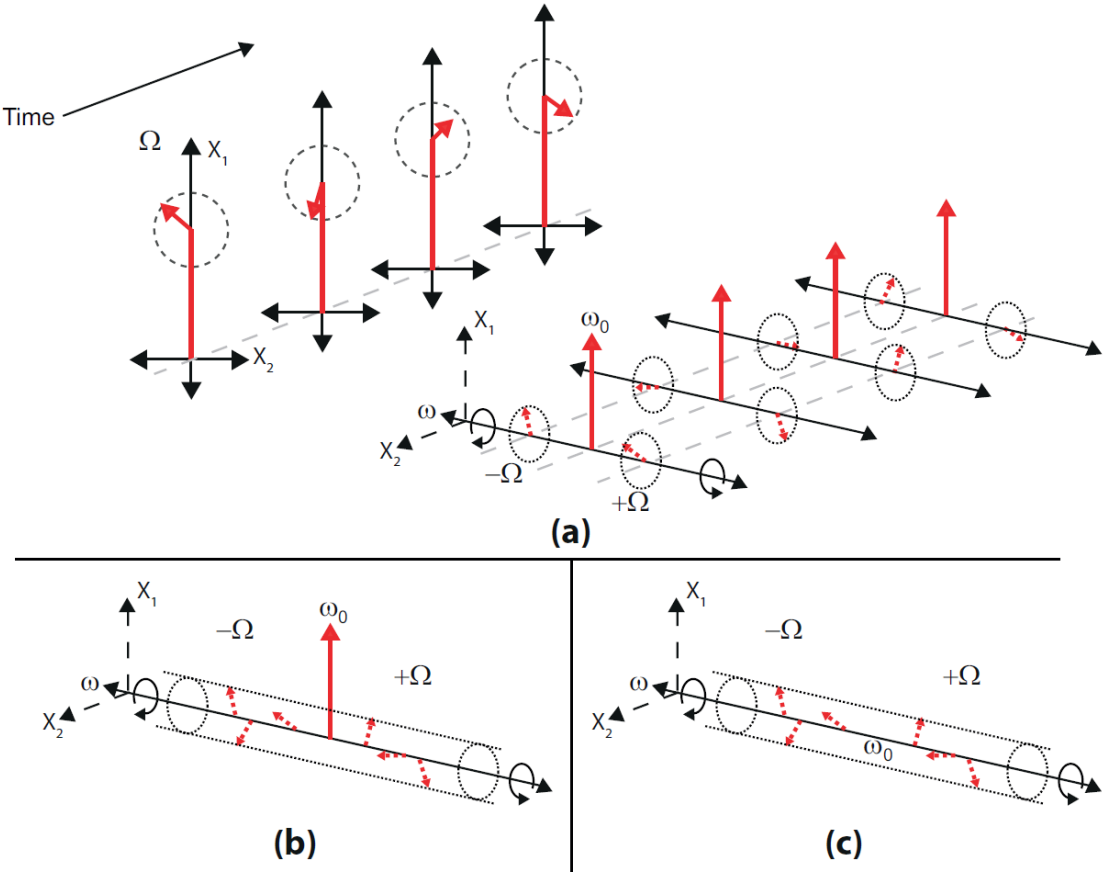

Fig. II.6 **Quantum noise as fluctuations of sideband modes.** *(a)The quantum phasor diagram where $\hat{a}(t) = \bar{a} + \delta\hat{a}(t)$ is represented on the complex plane as a constant classical field $|a|$ with time-dependent fluctuations of average variance unity for both quadratures and the sideband diagram where fluctuations are represented as sideband of amplitude unity but with a time-varying orientation. The quantum noise of the field can be represented by considering all the sidebands for $\Omega \in \mathbb{R}$. Quantum sideband diagrams of a coherent state (b) and a vacuum state (c). Figure from [41].*

II.3.5 Two-photon formalism

We now define the quadrature fields as the following linear combinations of the one-photon fields :

$$a_1 = \frac{(\delta a_+ + \delta a_-^*)}{\sqrt{2}} \quad \text{and} \quad a_2 = \frac{(\delta a_+ - \delta a_-^*)}{\sqrt{2}i}. \tag{II.51}$$

We can see that in the classical field representation, these quadratures correspond to the real and imaginary parts of the field. This formalism was developed by Carlton Caves in 1981 [5]. We can now express δI as

$$\delta I[\Omega] = ((\bar{a}^* + \bar{a})a_1[\Omega] + i(\bar{a}^* - \bar{a})a_2^*[\Omega]) \tag{II.52}$$

$$= \sqrt{2}\mathrm{Re}[\bar{a}]a_1[\Omega] + \sqrt{2}\mathrm{Im}[\bar{a}]a_2^*[\Omega]. \tag{II.53}$$

Finally, we can express the mean value of the field as $\bar{a} = |\bar{a}|e^{i\phi}$ and δI becomes

$$\delta I[\Omega] = \sqrt{2}|\bar{a}|\left(a_1[\Omega]\cos\phi + a_2[\Omega]\sin\phi\right) \tag{II.54}$$

We see that as we sweep the phase of the mean field we will be able to measure the amplitude of our two quadrature fields directly by measuring the Fourier transform of the field intensity which will always be the physical quantity we can actually measure. So the amplitude and phase fluctuations of our field are characterised by its two quadratures a_1 and a_2 which for are usually called respectively the amplitude quadrature and the phase quadrature. Indeed we can always choose the phase of the mean field to that they are aligned this way.

II.3.6 The vacuum state

We now consider a field with a zero mean intensity and only fluctuations. If we compute the mean fluctuations value of the two quadratures, we will find that $\langle|a_1|^2\rangle = \langle|a_2|^2\rangle = 1/2$ because of the commutation relations between $\hat{a}$ and $\hat{a}^\dagger$. We will use the "quantum phasor diagram" to represent this state by its Wigner function as a function of a_1 and a_2. In this representation, the state fluctuations are represented by a round hill in the centre of the phase space. We also see that, because of the circular symmetry, we can say that Δa_1 corresponds to amplitude fluctuations and Δa_2 to phase fluctuations. This state is particularly useful combined with the displaced frame approximation discussed above. We will represent our laser field by a coherent field, i.e. the sum of a classical bright field and a vacuum state with amplitude fluctuations $\langle a_1^2\rangle = 1/2$ and phase fluctuations $\langle a_2^2\rangle = 1/2$.

II.3.7 Representation and calculation of quantum noise

If we now consider vacuum fluctuations of the electromagnetic field, these can be seen as amplitude and phase modulations at every frequency Ω, so we can just consider $a_+[\Omega]$ and $a_-[\Omega]$ as two incoherent complex random variables of unit amplitude. Switching to

$a_1[\Omega]$ and $a_2[\Omega]$ just requires applying a unitary transformation, so a_1 and a_2 keep the same properties and we can write

$$\langle|\delta I[\Omega]|^2\rangle = 2|\bar{a}|^2\left(|a_1\cos\phi|^2 + |a_2\sin\phi|^2\right) = |\bar{a}|^2. \tag{II.55}$$

We retrieve the usual expression for shot noise: the intensity noise is a white noise proportional to the beam intensity. Using matrix representation, we can also write the noise power as

$$\langle|\delta I[\Omega]|^2\rangle = \left||\bar{a}|\begin{bmatrix}\cos\phi & \sin\phi\end{bmatrix}\begin{bmatrix}1 & 0\\ 0 & 1\end{bmatrix}\right|^2 = |b_\phi \cdot v_{in}|^2 \tag{II.56}$$

where b_ϕ is the local oscillator state and v_{in} embodies the input vacuum fluctuations with

$$v_{in} = \mathbf{I}. \tag{II.57}$$

The point of this notation is that one can calculate the quantum noise at the output of any optical system using

$$v_{out} = \mathbf{T}\cdot v_{in}$$

where $\mathbf{T}$ is the transfer matrix of the system. Output fluctuations can be measured by mixing the field of interest with an additional bright beam (local oscillator) and we get the noise power spectrum:

$$\langle|\delta I[\Omega]|^2\rangle = |b_\phi \cdot v_{out}|^2 = |b_\phi \cdot \mathbf{T}\cdot v_{in}|^2. \tag{II.58}$$

Chaining multiple optical elements (optical cavity, optical circulators, etc...) just requires chaining the corresponding transfer matrices to obtain the final output state.

II.3.8 Squeezed state representation

Vacuum or coherent states are obviously not the only available states of the quantum optical field in the quantum optics toolbox. Among states of great theoretical and experimental interest are squeezed states, which display asymmetrical variances between a_1 and a_2. The generation of squeezed states will be discussed in the following section, and dedicated experiments will be presented in a later chapter.

In the formalism presented above, the effect of a squeezer is represented by the following operator:

$$\mathbf{S}(\sigma,\psi) = \mathbf{R}(\psi)\mathbf{S}(\sigma)\mathbf{R}(-\psi) = \mathbf{R}\psi\ \mathbf{S}_\sigma\mathbf{R}_\psi^\dagger = \begin{bmatrix}\cos\psi & -\sin\psi\\ \sin\psi & \cos\psi\end{bmatrix}\begin{bmatrix}e^\sigma & 0\\ 0 & e^{-\sigma}\end{bmatrix}\begin{bmatrix}\cos\psi & \sin\psi\\ -\sin\psi & \cos\psi\end{bmatrix}, \tag{II.59}$$

where ψ is the angle of the ellipse of squeezing and $e^{-\sigma}$ and e^σ are the squeezing and anti-squeezing coefficients. Conventionally, squeezing magnitudes are expressed in decibels (dB), with $\sigma_{dB} = \sigma \times 20/\ln(10)$ We can immediately see that the effect of this operator on vacuum fluctuations will produce the following state:

$$v_{sqz} = \mathbf{R}_\psi\begin{bmatrix}e^\sigma & 0\\ 0 & e^{-\sigma}\end{bmatrix}\mathbf{R}_\psi^\dagger \tag{II.60}$$

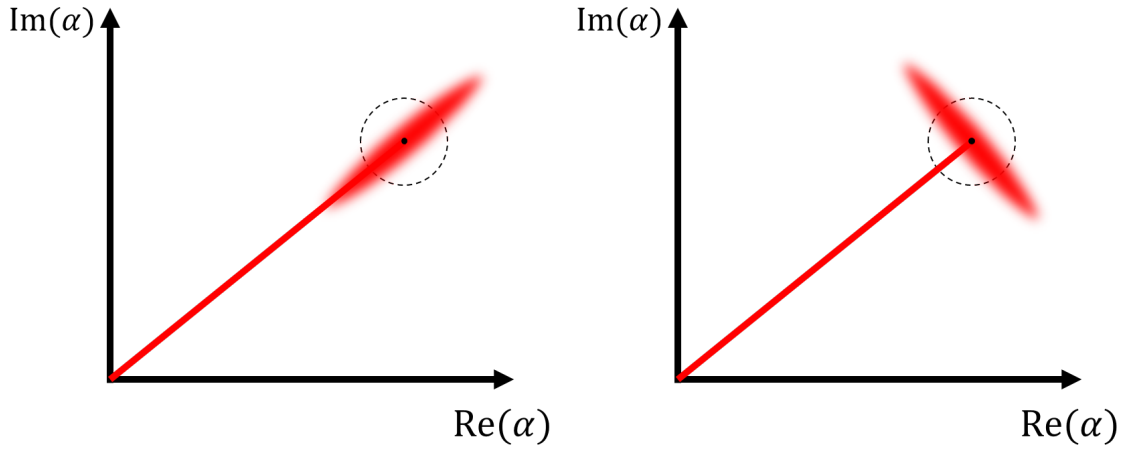

Fig. II.7 *Phase squeezed state and amplitude squeezed state representation on the complex plane.*

The point of the two-photon formalism is that it gives us an immediate representation of a squeezed state and makes the link between the optical field and the actual signal measured with a photodetector. In the one-photon formalism, this can be seen as correlation between the two sidebands at $\pm\Omega$ (II.6) :

$$a_+ = \frac{e^{\sigma} + ie^{-\sigma}}{\sqrt{2}} \quad \text{and} \quad a_- = \frac{e^{\sigma} - ie^{-\sigma}}{\sqrt{2}}. \tag{II.61}$$

We see that for high value of σ, a_+ and a_- have a similar orientation so when recombining them to obtain the quadratures, their fluctuations will be suppressed along one axis and amplified along the other.

II.3.9 One-photon transfer

Finally, if we want to obtain the effect of a linear optical element (i.e. an optical element which doesn't mix upper and lower sidebands), we can easily apply the following conversion matrix

$$\mathbf{A}_2 = \frac{1}{\sqrt{2}} \begin{bmatrix} 1 & 1 \\ -i & +i \end{bmatrix} \tag{II.62}$$

to switch back to the one-photon formalism where the transfer matrix $\mathbf{T}$ is diagonal:

$$\mathbf{T} = \mathbf{A}_2 \cdot \begin{bmatrix} t_+ & 0 \\ 0 & t_-^* \end{bmatrix} \cdot \mathbf{A}_2^{-1} \tag{II.63}$$

We will see in section II.5.5 part how to compute the coefficients $t_+(\Omega)$ and $t_-^*(\Omega)$ for a Fabry-Perot cavity.

II.3.10 The effect of optical losses on a squeezed state

Squeezed state are particularly sensitive to optical losses that are experimentally unavoidable. It is then necessary to be able to characterize their effect on a squeezed state. The

presence of loss on an optical field $\hat{a}$ is similar to the introduction of a partially reflective mirror with a transmission η_l. The main issue is that on the other port of the mirror, vacuum fluctuations couple to the exiting squeezed state that can then be written as

$$\hat{a}_{out} = \sqrt{\eta_l}\hat{a} + \sqrt{1-\eta_l}\delta\hat{a}_{vac}. \tag{II.64}$$
$$\tag{II.65}$$

The PSD of the output field can be computed and we find

$$S_1^{out} = \eta_l S_1^{in} + (1-\eta_l)S_1^{vac} \tag{II.66}$$
$$S_1^{out} = \eta_l S_1^{in} + (1-\eta_l) \tag{II.67}$$

where we used on the second line that the PSD of the vacuum field is unity. We can see that losses brings the squeezed state back to its coherent form as expected : you loose correlation between the photons as you lose them. On figure II.8, we plot the squeezing magnitude of the input field vs the output for different losses value. We can clearly see the drastic effect on large squeezing magnitude. For this reason we won't try to reach extreme value of squeezing because they will immediately disappear as the field propagates through the optics that all have losses. We will use the same model take in account the efficiency of the photodetectors η_{PD}

II.3.11 The quantum Langevin equation

In the quantum description, the time-evolution equation of the field operator becomes:

$$\dot{\hat{a}}(t) = \left(-\frac{\kappa}{2} + i\psi/\tau\right)\hat{a}(t) + \sqrt{\frac{\kappa_{in}}{\tau}}\hat{a}_{in}(t) + \sqrt{\frac{\kappa_0}{\tau}}\hat{a}_{vac}(t) \tag{II.68}$$

where we just replaced α by its quantized version $\hat{a}$ in equation II.19. Note that in the literature some people use $\hat{a}' = \sqrt{\tau}\ \hat{a}$, so that $|\hat{a}'|^2$ corresponds to the number of photons inside the cavity which can then be seen as a harmonic oscillator coupled to an input flux line $\hat{a}_{in}$ and an output flux line $\hat{a}_{vac}$ and then we get the proper quantum Langevin equation derived in the full quantum description:

$$\dot{\hat{a}}'(t) = i\Delta\omega\hat{a}'(t) - \frac{\kappa}{2}\hat{a}'(t) + \sqrt{\kappa_{in}}\hat{a}_{in}(t) + \sqrt{\kappa_0}\hat{a}_{vac}(t), \tag{II.69}$$

where $\Delta\omega = \omega_L - \omega_{cav} = \psi/\tau$ is the frequency cavity detuning. The different terms correspond to different physical mechanisms:

- the first term is the Hamiltonian evolution term. It corresponds to $\frac{-i}{\hbar}[\hat{a}'(t), H(t)]$, i.e. the commutator of $\hat{a}'(t)$ with the Hamiltonian in the rotating frame $H(t) = -\hbar\Delta\omega\hat{a}'^{\dagger}(t)\hat{a}'(t)$
- the second is a dissipation term (optical losses of the cavity)
- the two other terms are fluctuations induced by the two input and output flux lines.

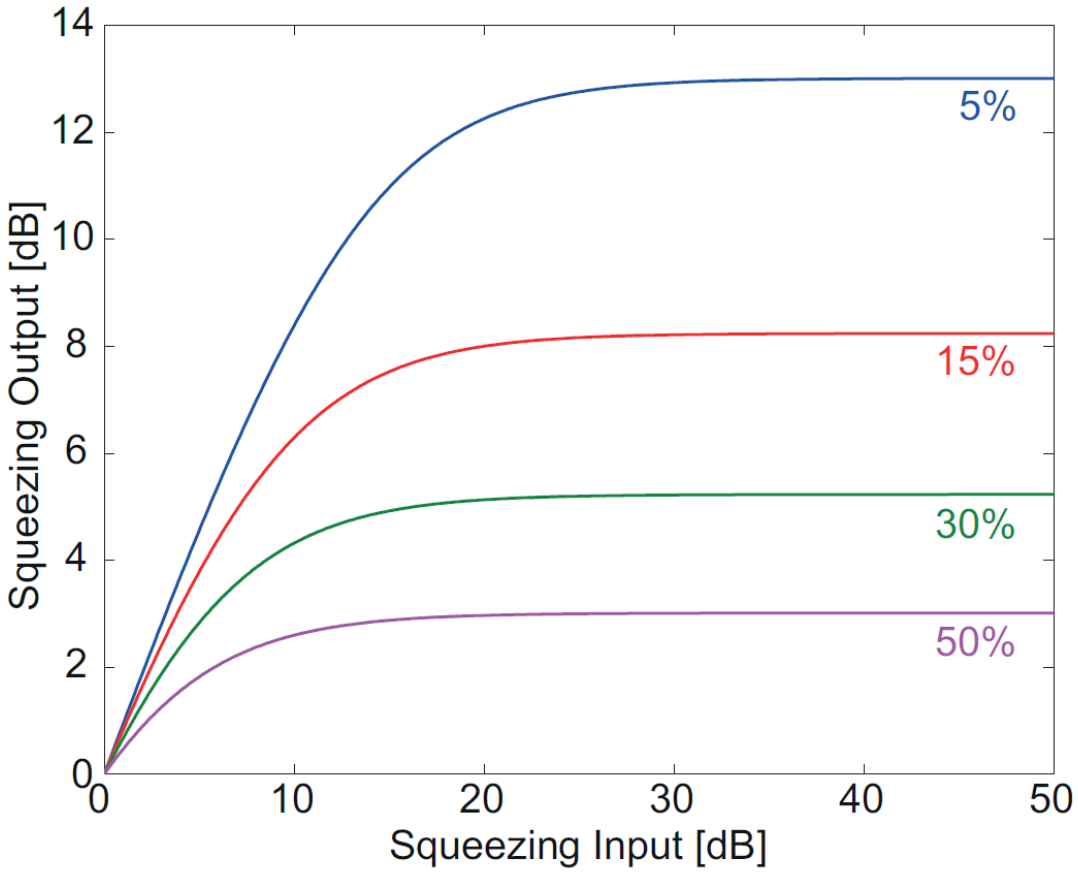

Fig. II.8 *Impact of optical loss on measured squeezing magnitude, as a function of input squeezing magnitude. Optical loss curves of 5%, 15%, 30% and 50% are shown. Figure from [41]*

II.3.12 Cavity with multiple output ports

The experiments discussed in this thesis also involve 3-mirror and 4-mirror cavities. For the field in such cavities, the previous equation can easily be adapted by adding an escape rate κ_i for each of the outputs. Equation II.20 becomes:

$$\left(\frac{\kappa}{2} - i\psi/\tau + i\Omega\right)\alpha[\Omega] = \sqrt{\frac{\kappa_{in}}{\tau}}\alpha_{in}[\Omega] + \sum_{i=1}^{n}\sqrt{\frac{\kappa_i}{\tau}}\alpha^i_{vac}[\Omega], \tag{II.70}$$

where n is the number of output ports, and $\alpha^i_{vac}[\Omega]$ are the vacuum fluctuations entering each port with no correlations between each other. We now have

$$\kappa = \kappa_{in} + \sum_{i=1}^{n}\kappa_i. \tag{II.71}$$

For the end mirror of a mode cleaner cavity, we can replace P by $T_2 + P$, T_2 being the transmission of the end mirror and P representing the overall losses of the cavity. If by

construction we choose $T_1 = T_2$, we get

$$R_{res} = \left(\frac{P}{2T_1 + P}\right)^2 \tag{II.72}$$

With $T_1 \approx 500$ ppm, it is easy to achieve losses $P \ll T_1$ and we still get a theoretical finesse of $\mathcal{F} = \frac{2\pi}{2T_1+P} \approx 6,000$ while having a reflection near zero at resonance, i.e. a maximized transmission which is ideal for a mode cleaner: a cavity with a low bandwidth (to filter out the noise) but still a high transmission (very little optical power lost).

II.3.13 Optical field detections

a) The Pound-Drever-Hall detection (PDH)

In order to keep cavity at resonance, the distance between the mirrors has to be stabilized by a quantity of roughly $\lambda/\mathcal{F}$ but seismic vibrations are order of magnitudes above this quantity. So in order to maintain cavity at resonance, one solution is to apply feedback either on the cavity length or the laser frequency. To do so, an error signal is required but as shown before the response function of a cavity as a zero-derivative at resonance so the measured reflection (or transmission) of a cavity can't be used as an error signal to lock the cavity at resonance. It can however be used to lock the cavity next to resonance using the non-zero derivative on the side of fringe. The idea proposed by Pound [42] and applied by Drever and Hall [43] was to apply a small phase modulation to the field before sending it to the cavity. The measured reflection of the cavity can now be written as

$$R\left[\psi + m\cos(\Omega_{mod}t)\right] \approx R(\psi) + m\frac{\partial R}{\partial \psi}\cos(\Omega_{mod}t). \tag{II.73}$$

If we now demodulate this signal at Ω_{mod}, we obtain a signal proportional to the derivative of the cavity response function which has a very high derivative at zero detuning and therefore is a very good error signal to lock the cavity on resonance(II.9).

b) The homodyne detection

All of our interferometric measurement suppose that we are actually able to measure the phase of the optical field. But when we make a measurement using a photo-diode, we can only access a signal proportional to the average field intensity $|\alpha|^2$ such that we do not get any information on the phase of the field. The most common way to access the phase of the field is to make it interfere with a very bright coherent field a_{LO} with a controllable phase ϕ, called a Local Oscillator (LO). The signal field $\hat{a}$ and the LO are spatially matched with an efficiency η_h, with the remaining LO field interacting with an orthogonal higher-order spatial mode occupied by the vacuum field $\delta\hat{a}_{vac}$ represented on figure II.10.

Placing two photo-diodes and detecting the two output fields of the beam-splitter, we obtain the fields :

$$c = \frac{1}{\sqrt{2}}\left[(\bar{a}_{LO} + \delta\hat{a}_{LO})e^{i\phi} + \sqrt{\eta_h}(\bar{a} + \delta\hat{a}) + \sqrt{1-\eta_h}\delta\hat{a}_{vac}\right] \tag{II.74}$$

$$d = \frac{1}{\sqrt{2}}\left[(\bar{a}_{LO} + \delta\hat{a}_{LO})e^{i\phi} - \sqrt{\eta_h}(\bar{a} + \delta\hat{a}) - \sqrt{1-\eta_h}\delta\hat{a}_{vac}\right] \tag{II.75}$$

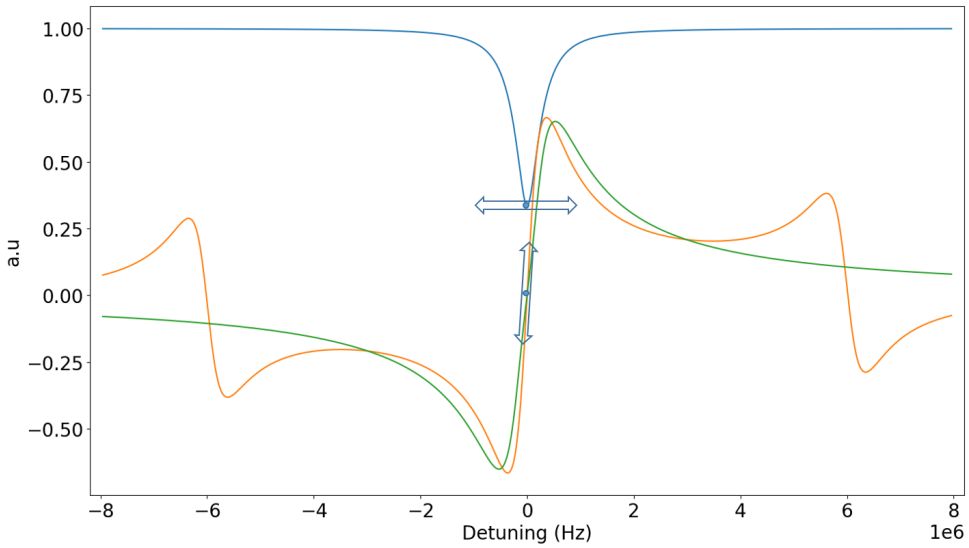

Fig. II.9 *Cavity error signals. In blue, is the cavity reflection that has a zero-derivative at resonance and in orange is the actual PDH signal with its high derivative at resonance. The green curve is the derivative of the cavity reflection rescaled to match the PDH amplitude. The parameters of the cavity are* $T_1 = 0.02$, $T_2 = 0.01$, $L = 1$ *m and the modulation frequency is at 6 MHz.*

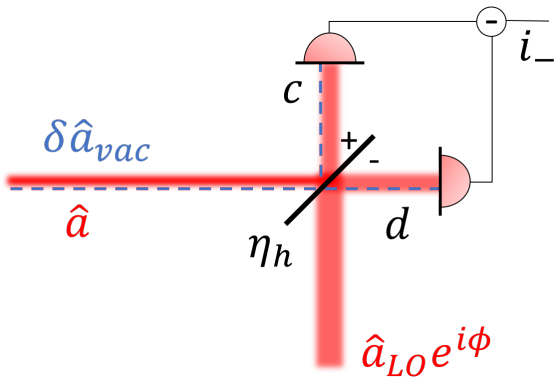

Fig. II.10 *Homodyne detection with spatial mode mismatch, showing the mixing of the LO oscillator* a_{LO} *to the signal field* $\hat{a}$ *with an efficiency* η_h *and to the higher-order mode vacuum state* $\delta\hat{a}_{vac}$ *with an efficiency* $1 - \eta_h$*. The two sides of the beam splitter have opposite phase due to the conservation of energy.*

The subtracted current of the two photo-diodes signal $i_- = d^\dagger d - c^\dagger c$ can then be written as

$$i_- = 2\sqrt{\eta_h}\bar{a}\bar{a}_{LO}\cos(\phi) \tag{II.76}$$
$$+ \bar{a}_{LO}\left[(\sqrt{\eta_h}a_1 + \sqrt{1-\eta_h}a_1^{vac})\cos(\phi)\right. \tag{II.77}$$
$$\left.+(\sqrt{\eta_h}a_2 + \sqrt{1-\eta_h}a_2^{vac})\sin(\phi)\right] \tag{II.78}$$

By tuning the phase of the LO we can then measure the two quadrature of the field but we see that, due to the spatial mismatch we are only going to detect them with an efficiency η_h. In the same way that optical loss mixed vacuum fluctuations with our squeezed state, spatial mode-mismatch mixed higher order mode vacuum fluctuations with the squeezed state. Therefore the spatial mode matching of the squeezed field and the LO is important for effective squeezing measurement.

To assess the spatial mode matching, the fringe visibility or contrast C is measured by

$$C = \frac{P_{max} - P_{min}}{P_{max} + P_{min}} \tag{II.79}$$

where P_{max} and P_{min} are the maximum and minimum value of interference fringes optical power on one of the detector and can be written as

$$P_{max} = \frac{1}{2}\left[(|\bar{a}_{LO}|^2 + |\bar{a}|^2 + 2\sqrt{eta_h}|\bar{a}_{LO}\bar{a}\right] \tag{II.80}$$
$$P_{min} = \frac{1}{2}\left[(|\bar{a}_{LO}|^2 + |\bar{a}|^2 - 2\sqrt{eta_h}|\bar{a}_{LO}\bar{a}\right] \tag{II.81}$$

So for equal optical power of the two beam (i.e $|a| = |a_{LO}|$), we have $C = \sqrt{\eta_h}$ and so the homodyne measurement efficiency can be measured with the fringe visibility, $\eta_h = C^2$.

II.4 Generation of squeezed light with non-linear optics

In this section, I will briefly explain how non-linear processes inside a cavity can be enhanced and used in our experiments to produce squeezed light. We will use α and $\hat{a}$ to describe the field at 1064 nm and β and $\hat{b}$ to describe the harmonic field at $2\omega_L$ and 532 nm.

The Hamiltonian for the non-linear interaction can be written as

$$H_{NL}(t) = \epsilon(\hat{b}^\dagger\hat{a}\hat{a} + \hat{b}\hat{a}^\dagger\hat{a}^\dagger). \tag{II.82}$$

The two terms each corresponding to a different process:

- the first term corresponds to the annihilation of 2 photons at ω_L to create a single photon at $2\omega_L$ ("Second Harmonic Generation")
- the second term corresponds to the annihilation of a single photon at $2\omega_L$ to create 2 correlated photons at $\omega_L \pm \Omega$ ("Parametric Down Conversion").

We will first explain how we are able to generate a bright field at 532 nm using the SHG process and then how this "pump" field allows us to generate squeezing using the second process to create correlations. We will assume the cavity is kept at resonance ($\Delta\omega = 0$). If we consider the Langevin equation, the commutator terms are here:

$$[\hat{a}(t), H_{NL}(t)] = 2\epsilon\hat{a}^\dagger\hat{b} \tag{II.83}$$

$$[\hat{b}(t), H_{NL}(t)] = \epsilon\hat{a}\hat{a}, \tag{II.84}$$

so the quantum Langevin equations become:

$$\dot{\hat{a}}(t) = \epsilon\hat{a}^\dagger(t)\hat{b}(t) - \frac{\kappa^a}{2}\hat{a}(t) + \sum_{i=1}^{n}\sqrt{\frac{\kappa_i^a}{\tau}}\hat{a}_i(t) \tag{II.85}$$

$$\dot{\hat{b}}(t) = \frac{\epsilon}{2}\hat{a}(t)\hat{a}(t) - \frac{\kappa^b}{2}\hat{b}(t) + \sum_{i=1}^{n}\sqrt{\frac{\kappa_i^b}{\tau}}\hat{b}_i(t) \tag{II.86}$$

II.4.1 Quasi-phase matching

The non-linear process occurs along the whole beam path in the crystal, meaning the output field created at the front of the crystal via the non-linearity will propagate and eventually interfere with the output field created at the back. For the SHG process for instance, the conservation of energy yields

$$2\,\omega_{IR} = \omega_G, \tag{II.87}$$

while, if we assume for instance that the input infrared and output green fields propagate colinearly with each other, phase-matching requires:

$$2\,k_{IR} = k_G. \tag{II.88}$$

These two conditions require that the infrared and green fields must share the same value of the optical index:

$$n_{IR} = n_G, \tag{II.89}$$

which seems impossible to fulfill because of the natural material dispersion. A common trick is to take advantage of the birefringent properties of the nonlinear crystals. If the infrared and green fields do not have the same polarization, the optical index follows two sets of curves for the ordinary and extraordinary optical index and it is possible to achieve:

$$n_e(1064\,\text{nm}) = n_o(532\,\text{nm}). \tag{II.90}$$

In the case where the polarization trick is not sufficient to achieve this or when the infrared and green fields share the same polarization, one may use *quasi-phase matching*. The idea is to periodically invert the sign of non-linear coefficient by flipping the material crystal domain structures. This technique called periodic poling allows for the phase of the newly generated field to be quasi-phase matched with the existing generated field (II.11). It is the one used for both of the non-linear crystal in our squeezing experiments.

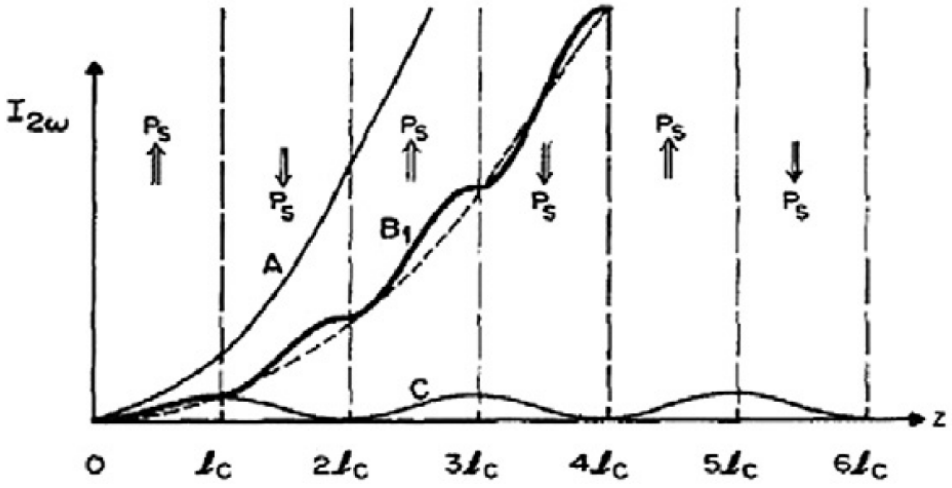

Fig. II.11 *Effect of phase matching on the growth of second harmonic power with nonlinear crystal length. A: perfect phase-matching in a uniformly poled crystal; C: non-phase-matched interaction; B: Quasi-phase matching by flipping the sign of the crystal polarization every coherence length of the interaction of curve C. Curve from [44]*

For a general nonlinear parametric process, we define the wavevector mismatch as

$$\Delta k = \sum_{in} k_i - \sum_{out} k_j. \tag{II.91}$$

To fine tune the crystal to reach the quasi-phase matching condition $\Delta k = 0$ for the precise wavelength of the pump laser, one usually tunes the crystal temperature. The expression for the generated output field power as a function of phase mismatch, derived in [45] can be written as

$$P = P_{max}\text{sinc}^2(\Delta k x/2). \tag{II.92}$$

An example of such a tuning curve is given in the SHG section of Chap. IV.

II.4.2 Second Harmonic Generation (SHG)

For the SHG, we are only interested in the static value of the bright field so we can neglect vacuum fluctuations and just consider the classical fields α and β. We pump the cavity with a bright field α_{in} at ω_L and we want to create a bright field at $2\omega_L$ in reflection (β_{ref}). If we neglect the depletion of the pump α due to the non-linear process we have from II.85:

$$\frac{\kappa^b}{2}\beta = \frac{\epsilon}{2}\alpha^2 \tag{II.93}$$

$$\alpha = \frac{2}{\kappa^a}\sqrt{\frac{\kappa^a_{in}}{\tau}}\alpha_{in} \tag{II.94}$$

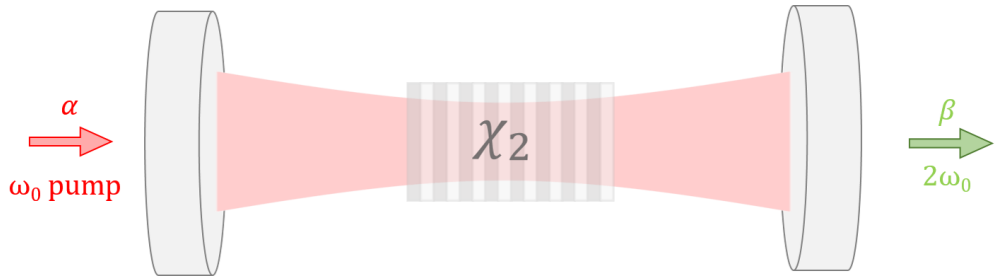

Fig. II.12 *Representation of the second harmonic non-linear process. A bright field at ω_0 pumps a non linear crystal to create frequency-doubled light at $2\omega_0$.*

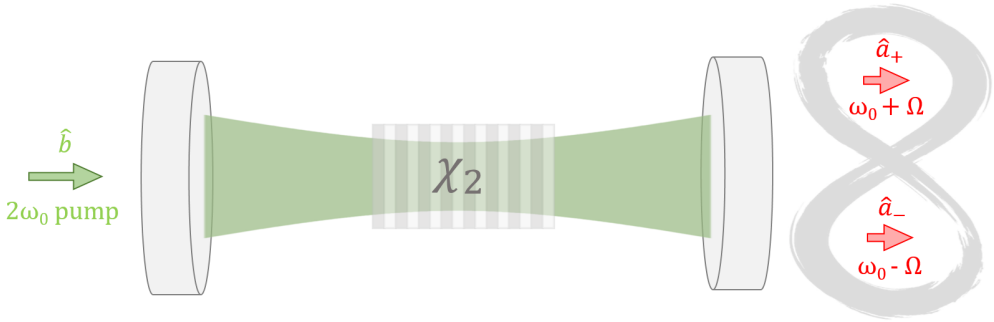

Fig. II.13 *Representation of the parametric down-conversion non-linear process. A bright field at $2\omega_0$ pumps a non linear crystal to create a pair of entangled photons at $\omega_0 + \Omega$ and $\omega_0 - \Omega$.*

Using the input relation of the cavity (II.26), we can find

$$\beta_{ref} = \sqrt{\frac{\kappa_{in}^b}{\tau}}\frac{\epsilon}{\kappa^b}\alpha^2 = 4\sqrt{\frac{\kappa_{in}^b}{\tau}}\frac{\kappa_{in}^a}{\kappa^b(\kappa^a)^2}\epsilon\alpha_{in}^2 \tag{II.95}$$

And we can simplify this awful expression to get the green light power:

$$I_{ref}^b = \frac{2\epsilon\kappa_{in}^b}{(\pi\kappa_b)^2\tau}\eta_a^2\mathcal{F}_a^2(I_{in}^a)^2. \tag{II.96}$$

To optimize the amount of optical power created at 532 nm, we need to have an over-coupled cavity in the infrared where $T_a > P_a$ while keeping a great finesse (i.e. $T_a + P_a \ll 1$). We also see that we need the output rate to dominate for the harmonic field so the SHG cavity design will use a mirror with a low reflectivity at 532 nm and a high reflectivity at 1064 nm to optimize the amount of green power delivered by the system.

II.4.3 The Optical Parametric Oscillator

The optical parametric oscillator (OPO) is the non-linear device that will actually produce the squeezed field. It is pumped with a bright field at 532 nm this time and we will neglect

again the depletion of the pump field, that is this time, the term $\frac{\epsilon}{2}a^2$ in the pump field cavity equation. We will first consider the classical behaviour of the OPO, that we will use in experiments to characterize its efficiency.

a) Classical behaviour of the OPO

The quantum Langevin equation II.85 for the fundamental fields becomes

$$\dot{\hat{a}} = g\hat{a}^\dagger - \frac{\kappa_a}{2}\hat{a} + \sqrt{\kappa_{in}^a}\hat{a}_{in}, \tag{II.97}$$

where we introduced the non-linear gain $g = \epsilon\beta$. Using again the input-output relations and assuming α_{in} real, we can write the ratio between the transmitted output seed power ($P_{out} \propto |\alpha_{out}|^2$) to the transmitted output seed power with no non-linear gain ($P_{out}^0 \propto |\alpha_{out}(g=0)|^2$) as

$$\frac{P_{out}}{P_{out}^0} = \frac{(1+x)^2}{(1-|x|^2)^2} \tag{II.98}$$

with $x = \frac{2g}{\kappa_a} = \frac{2\epsilon\beta}{\kappa_a}$ is the normalized pump parameter. We can see that depending on the pump phase, we either have amplification (for real positive value of β) or deamplification (for real negative value of β) of the seed power. We will only consider the extreme case and write

$$\frac{P_{out}^\pm}{P_{out}^0} = \frac{(1\pm x)^2}{(1-x^2)^2} \tag{II.99}$$

where P_{out}^+ is the amplified value of the seed power and P_{out}^- the deamplified value. We see that P_{out}^+ diverges for $x = 1$ (Figure II.14), so we can define the threshold power of the pump as

$$x = \sqrt{\frac{P^{pump}}{P_{thr}^{pump}}}. \tag{II.100}$$

This divergence comes from breaking down of the assumption of no pump depletion. Above this threshold we can observe spontaneous emission of infrared light inside the cavity. For squeezing purpose, we always want to be below that threshold so it's important to measure it precisely. It's also a good way to make sure the OPO is functioning correctly as it is easier to observe parametric amplification than squeezing.

b) The semiclassical behaviour of the OPO

We will now consider the Langevin equation including vacuum fluctuations with a bright pump β_{in} entering the cavity and no bright seed field. Using the one photon formalism, we get

$$-i\Omega\delta\hat{a}_+[\Omega] = g\delta\hat{a}_-^*[\Omega] - \frac{\kappa_a}{2}\delta\hat{a}_+[\Omega] + \sum_{i=1}^{n}\sqrt{\frac{\kappa_i^a}{\tau}}\delta\hat{a}_+^i[\Omega] \tag{II.101}$$

$$-i\Omega\delta\hat{a}_-^*[\Omega] = g\delta\hat{a}_+[\Omega] - \frac{\kappa_a}{2}\delta\hat{a}_-^*[\Omega] + \sum_{i=1}^{n}\sqrt{\frac{\kappa_i^a}{\tau}}\delta\hat{a}_-^{i*}[\Omega], \tag{II.102}$$

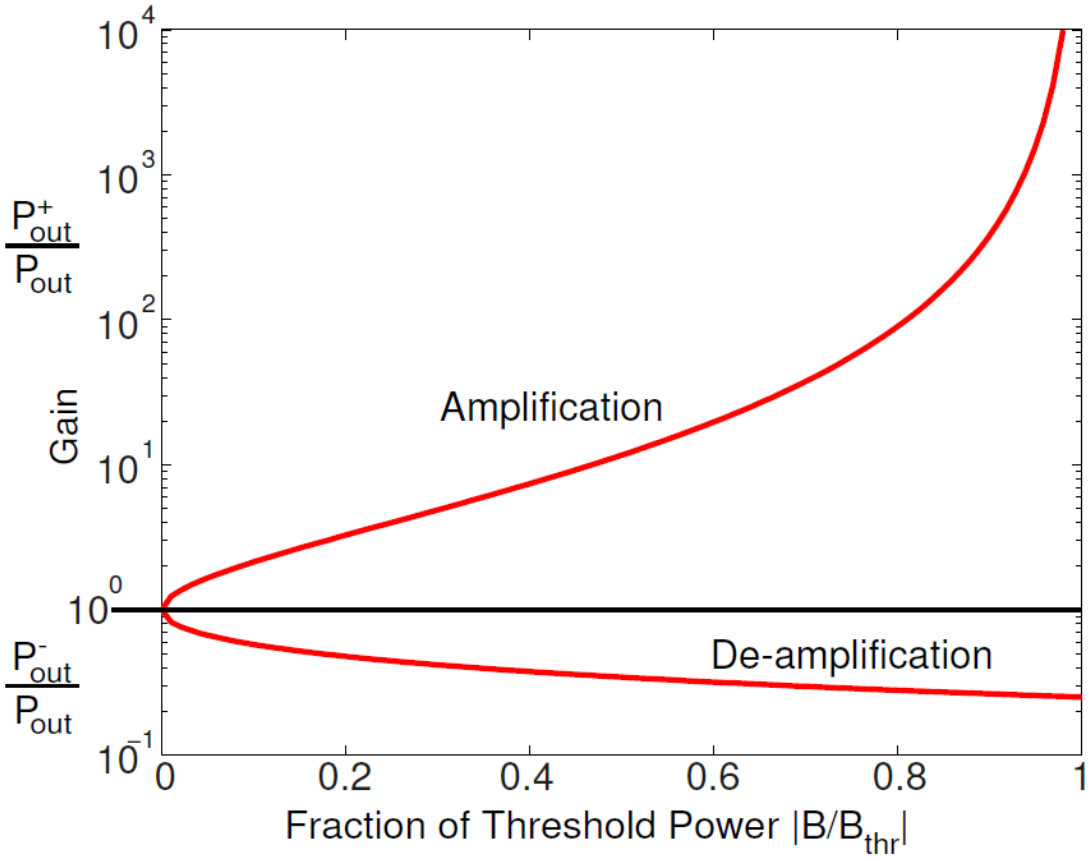

Fig. II.14 *OPO nonlinear gain curves as a function of x. We see that as x goes to 1, the amplification curve diverges, as our assumption of no pump depletion is no longer valid. Figure from [41]*

where we assumed g real and positive. We clearly see in those equations that the non-linearity has coupled the positive and negative sidebands. Going to Fourier space and computing the two quadratures yields:

$$a_1[\Omega] = \sum_{i=1}^{n} \frac{\sqrt{\kappa_i^a} a_1^i(t)}{\kappa_a/2 - g - i\Omega} \tag{II.103}$$

$$a_2[\Omega] = \sum_{i=1}^{n} \frac{\sqrt{\kappa_i^a} a_2^i(t)}{\kappa_a/2 + g - i\Omega}. \tag{II.104}$$

Using the input-output relationship, we find

$$a_1^{out}[\Omega] = \sqrt{\kappa_{out}} \sum_{i=1}^{n-1} \frac{\sqrt{\kappa_i^a}}{\kappa_a/2 - g - i\Omega} a_1^i - \frac{\kappa_{out} - \kappa_a + g + i\Omega}{\kappa_a/2 - g - i\Omega} a_1^{vac} \tag{II.105}$$

$$a_2^{out}[\Omega] = \sqrt{\kappa_{out}} \sum_{i=1}^{n-1} \frac{\sqrt{\kappa_i^a}}{\kappa_a/2 + g - i\Omega} a_2^i - \frac{\kappa_{out} - \kappa_a - g + i\Omega}{\kappa_a/2 + g - i\Omega} a_2^{vac} \tag{II.106}$$

Finally, we can compute the Power Spectral Density(PSD) $S_i^{out} = a_i^{out}(a_i^{out})^\dagger$, assuming all the input fluctuations are vacuum fluctuations from coherent field so that their PSD are unity and we get:

$$S_1^{out}[\Omega] = 1 + \eta_{esc}\frac{4x}{4\Omega^2/\kappa_a^2 + (1-x)^2} \tag{II.107}$$

$$S_2^{out}[\Omega] = 1 - \eta_{esc}\frac{4x}{4\Omega^2/\kappa_a^2 + (1+x)^2}, \tag{II.108}$$

where $\eta_{esc} = 2\kappa_{out}^a/\kappa_a$ is the escape efficiency of the OPO. We can see that the first quadrature is antisqueezed and the second one is squeezed. To maximize the amount of squeezing, we need to make the escape efficiency as high as possible so that the transmission of the output port dominates over the total losses of the cavity. There is, however, a trade-off to consider as a high output transmission increases P_{trh}^{pump}, and one needs a higher pump power to keep x constant. It is also worth noting that the squeezing created by the OPO is not the perfect theoretical squeezed state presented in the theory section:

$$S_1^{out}[\Omega] = e^{2\sigma} \tag{II.109}$$

$$S_2^{out}[\Omega] = e^{-2\sigma}. \tag{II.110}$$

We, however, recover a perfectly squeezed quadrature close to the OPO threshold ($x \to 1$) at the condition of a very good escape efficiency ($\eta_{esc} \to 1$) and for sideband frequencies in the cavity bandwidth ($\Omega \ll \kappa_a/2$).

II.5 Optomechanics and continuous position measurement

In this section, I will introduce specific optomechanical concepts to describe continuous optical sensing of a mirror position and the sensitivity limits related to the quantum nature of light:

- radiation-pressure coupling between the displacement and the optical field
- the fluctuation-dissipation theorem and thermal noise spectrum
- quantum phase noise, quantum radiation pressure noise (QRPN) and the corresponding standard quantum limit (SQL)

.

II.5.1 Radiation-pressure coupling

We now consider a cavity, represented on figure II.16 where the end mirror is supported by a spring and can move along the propagation axis by a small quantity $\delta x(t)$. The cavity length now becomes

$$L_{cav}(t) = L_0 + \delta x(t) \tag{II.111}$$

and the dephasing

$$\psi(t) = 2k(L_0 + x(t)) = \Delta\tau + 2k\delta x(t) \tag{II.112}$$

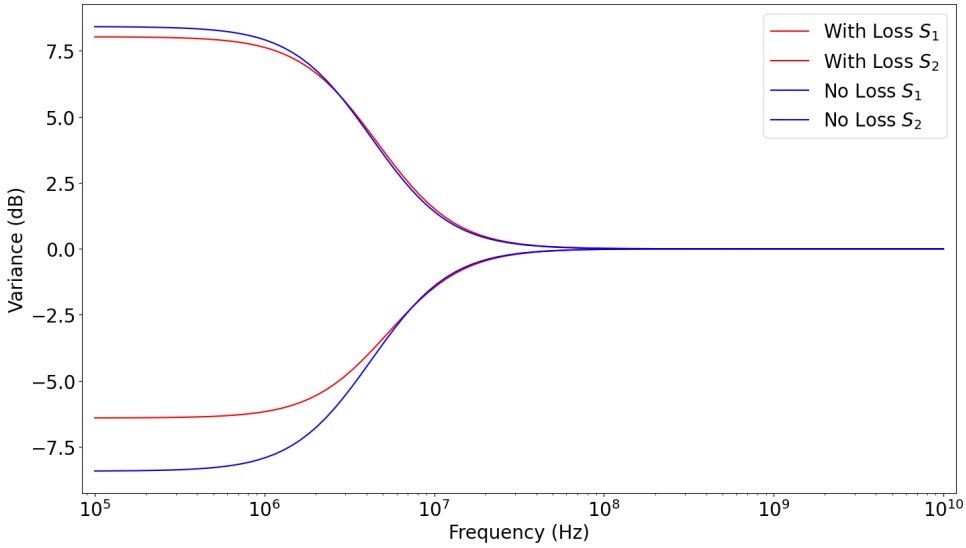

Fig. II.15 *Output noise variance of an OPO cavity, showing the generation of squeezing and anti-squeezing. Cavity parameters* $L_{cav} = 1$ *m;* $\lambda = 1$ μ*m;* $T_{out} = 0.1$*;* $x = 2g/\kappa_a = 0.45$*;* $T_{in} = 0.01$ *and* $T_l = 0.001$*. For the zero-loss case* $T_{in} = T_l = 0$*. We see that losses affect squeezing more than antisqueezing. We also see that we only have squeezing below the cavity bandwidth* $\kappa_a = 2\pi \times 15$ *MHz.*

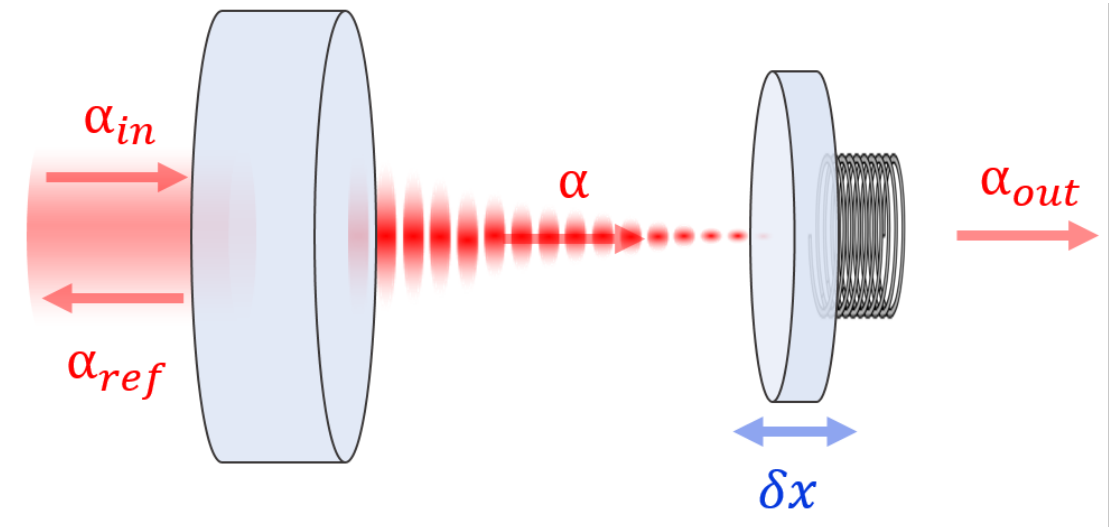

Fig. II.16 *Schematic of the optical fields interacting with a cavity where the end mirror is attached by a spring and can move from its equilibrium position by a small quantity* δx*.*

where $\Delta = \omega_L - \omega_{cav}$ is the frequency detuning of the cavity. The equation of motion for the mirror can be written as

$$m_{eff}\left[\delta\ddot{x}(t) + \Gamma_m\delta\dot{x}(t) + \Omega_m^2\delta x(t)\right] = \delta F_{RP}(t) + \delta F_{th}(t), \tag{II.113}$$

where we model our mirror on a spring as a harmonic oscillator of mass m_{eff}, resonance frequency $\Omega_m/2\pi$ and with a viscous damping rate Γ_m. In reality, the mechanical resonators used in the discussed experiments have numerous vibration modes, with different displacement profiles, different effective masses, different resonance frequencies... We will assume that their mechanical resonances are sufficiently separated in frequency that we can neglect any coupling between them and just use the simple harmonic oscillator model separately for each mode. Here, we will only focus on the main vibration, which is engineered to have a maximum displacement of the mirror (and hence a minimum effective mass m_{eff}) for a given force, and minimal mechanical damping. $F_{RP}(t)$ represents the force due to radiation pressure and can be written as:

$$F_{RP}(t) = -2\hbar k I(t) = -\frac{2\hbar k}{\tau}\bar{a}^2 - \frac{2\hbar k}{\tau}\bar{a}(\delta a(t) + \delta a^*(t)) = \bar{F}_{RP} + \delta F_{RP}(t) \tag{II.114}$$

i.e. the change of momentum of one photon reflected upon the mirror multiplied by the flux of incident photons. We will neglect the static part of the force that is just changing the equilibrium position of the resonator. In all of our experiment, we are tuning the cavity length to the laser so we are not sensitive to such effect.

II.5.2 The Fluctuation-dissipation theorem

Any mechanical object in a thermal bath is subject to a random force $\delta F_{th}(t)$, called the thermal Langevin force. We will just make the assumption that it has no memory, i.e. that its correlation function is a Dirac distribution. So we can write the power spectral density of F_{th}:

$$S_F^{th}[\Omega] = \int_{-\infty}^{+\infty} < \delta F(t)\delta F(t+t') > e^{i\Omega t'}\mathrm{d}t' \tag{II.115}$$

$$= \delta F_0^2 \int_{-\infty}^{+\infty} \delta(t-t')e^{i\Omega t'}\mathrm{d}t' \tag{II.116}$$

$S_F^{th}[\Omega]$ clearly doesn't depend on Ω: it is white noise, with $S_F^{th}[\Omega] = S_F^{th}[0]$. We will also make the assumptions that it dominates over the noise of the laser, so we can write, using the properties of the power spectral density:

$$< \delta x^2 > = \int_{-\infty}^{+\infty} S_{xx}[\Omega]\frac{\mathrm{d}\Omega}{2\pi} = \int_{-\infty}^{+\infty} |\chi_m(\Omega)|^2 S_F^{th}\frac{\mathrm{d}\Omega}{2\pi} \tag{II.117}$$

$$= S_F^{th}\int_{-\infty}^{+\infty} |\chi_m(\Omega)|^2\frac{\mathrm{d}\Omega}{2\pi}, \tag{II.118}$$

where $\chi_m(\Omega) = 1/(m_{eff}\left[-\Omega^2 - i\Omega\Gamma_m + \Omega_m^2\right])$ is the mechanical susceptibility of the mechanical resonator. If we consider a high quality factor resonator ($\Gamma_m \ll \Omega_m$), the modulus of the response function is peaked around Ω_m so we can compute the value of the

integral by restricting ourselves to a small window $\Delta\Omega$ around Ω_m such that $\Omega = \Omega_m + \Delta\Omega$ with $\Delta\Omega \ll \Omega_m$ and the integral becomes a Lorentzian :

$$\int_{-\infty}^{+\infty} |\chi_m(\Omega)|^2 \frac{\mathrm{d}\Omega}{2\pi} = \int_{-\infty}^{+\infty} \frac{1}{m_{eff}^2\Omega_m^2((\Omega_m-\Omega)^2+\Gamma_m^2)} \frac{\mathrm{d}\Omega}{2\pi} = \frac{\Gamma_m}{4m_{eff}^2\Omega_m^2}. \tag{II.119}$$

Finally, we use the equipartition theorem to compute the variance of the displacement,

$$\frac{1}{2} m_{eff}\Omega_m^2 < \delta x^2 >= \frac{1}{2} k_B T \tag{II.120}$$

We can replace both terms in equation (II.117) to obtain:

$$S_F^{th} = 4k_B T \Gamma_m m_{eff} = 4k_B T \gamma, \tag{II.121}$$

where $\gamma = \Gamma_m m_{eff}$ is the physical damping of the resonator which only depends on how its geometry interacts with the thermal bath. We have demonstrated the fluctuation dissipation theorem in the specific case of a high quality factor harmonic resonator but this result can be extended for any mechanical system with a response function $\chi_m(\Omega)$ and would be written

$$S_F^{th}[\Omega] = 4\pi k_B T \,\mathrm{Im}\left[\chi_m(\Omega)\right]. \tag{II.122}$$

If we only take mechanical thermal noise into account, measuring the power spectral density of the displacement will therefore display white noise filtered by the mechanical response of the harmonic oscillator.

II.5.3 Quantum Phase Noise

But the quantum nature of the light field used to probe the displacement eventually adds some additional noise to the measured signal. For a cavity at resonance, the quantum Langevin equation at the first order becomes

$$\dot{\delta\hat{a}}(t) = \frac{2ik\bar{a}}{\tau} x - \frac{\kappa}{2}\delta\hat{a}(t) + \sqrt{\kappa_{in}}\hat{a}_{in}(t), \tag{II.123}$$

where we the phase shift term is now only due to the back mirror's motion. Computing the two quadratures of the reflected field in Fourier space yields:

$$a_1^{out}[\Omega] = \frac{\kappa/2 + i\Omega}{\kappa/2 - i\Omega} a_1^{in}[\Omega] \tag{II.124}$$

$$a_2^{out}[\Omega] = \frac{\kappa/2 + i\Omega}{\kappa/2 - i\Omega} a_2^{in}[\Omega] + \frac{4\bar{a}k}{\tau\sqrt{\kappa_{in}}(1 - 2i\Omega/\kappa)} x[\Omega]. \tag{II.125}$$

We see that at resonance, the mechanical motion of the end mirror has no effect on the amplitude fluctuations of the field. If we now compute the power spectral density $S_2^{out}[\Omega] = a_2^{out}[\Omega](a_2^{out}[\Omega])^*$ of the phase fluctuations of the reflected field, we obtain:

$$S_2^{out}[\Omega] = 1 + \frac{256\mathcal{F}^2 I_{in}}{1 + (2\Omega/\kappa)^2} \frac{S_x[\Omega]}{\lambda^2}. \tag{II.126}$$

We see that the first term corresponds to the phase fluctuations of the field and the second to the actual motion of the resonator enhanced by the cavity finesse and filtered by the

cavity response. From this expression, we can derive S_x^{QSN}, the displacement noise power spectral density that will create a phase noise equivalent to the quantum phase noise of the field (referred to as Quantum Shot Noise, QSN) :

$$S_x^{QSN}[\Omega] = \frac{1 + (2\Omega/\kappa)^2}{256\mathcal{F}^2 I_{in}}\lambda^2. \tag{II.127}$$

For a displacement measurement close to the optical resonance (for mechanical frequencies $\Omega_m \ll \kappa$), this will add a constant background to the thermal peak previously mentioned and will set a fundamental limit to the precision of the measurement (Fig. II.17). We see that this noise power is inversely proportional to the input laser intensity expected, which seems to imply that the measurement sensitivity can be increased at will simply by cranking up the laser power (provided a high laser power is available, and thermal absorption issues stay under control).

II.5.4 Quantum Radiation Pressure Noise

We will, however, see that the displacement sensitivity can **not** be increased at will because of a back-action of the measurement: increasing the laser power does decrease phase noise but amplifies the effect of amplitude fluctuations of the probe beam, which are coupled to the mechanical motion by radiation pressure.

As discussed above, the fluctuating part of the radiation pressure force can be written as

$$\delta F_{RP}(t) = -\frac{2\hbar k}{\tau}\bar{a}(\delta a(t) + \delta a^*(t)) \tag{II.128}$$

which can be written in the Fourier space as

$$\delta F_{RP}[\Omega] = -\frac{2\sqrt{2}\hbar k}{\tau}\bar{a}a_1[\Omega]. \tag{II.129}$$

We will write its power spectral density to compare it to the thermal noise and obtain:

$$S_F^{RP} = \frac{64\hbar^2\mathcal{F}^2}{\lambda^2} I_{in} \tag{II.130}$$

using the input-output relations. We see that radiation pressure fluctuation are proportional to the input laser intensity and will compete with thermal noise as a white noise driving the motion of the harmonic oscillator. If we consider a case where radiation pressure dominates over thermal noise, we can write the total power spectral density of the displacement measurement as

$$S_x[\Omega] = S_x^{QSN}[\Omega] + |\chi_m(\Omega)|^2 S_F^{RP} = S_x^{QSN}[\Omega] + S_x^{QRPN}[\Omega]. \tag{II.131}$$

Plotting this expression on figure II.18 as a function of the sideband frequency Ω (in the limit where $\Omega \ll \kappa$) displays two contributions:

- a constant background due to phase noise (inversely proportional to the input optical power)

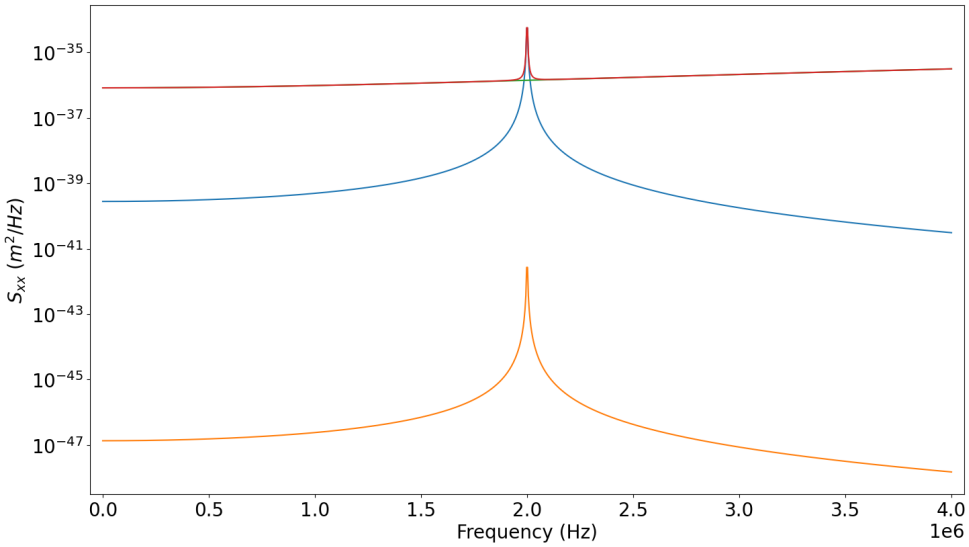

Fig. II.17 **An oscillator dominated by thermal noise. Noises in the position measurement of a macroscopic mechanical resonator with $Q = 1000$, $\Omega_m/2\pi = 2$ MHz and $m_{eff} = 100$ µg. The orange curve represents the displacement noise due to QRPN for an input optical power of $10\,\mu$W at 1064 nm, which is negligible compared to thermal noise (blue curve) for an environment temperature of 1 K. The green curve represents the QSN, which is an almost constant noise background. The red curve displays the total displacement noise.**

- a peak corresponding to the mechanical resonance excited by the amplitude noise of the laser (proportional to the input optical power).

Outside of the mechanical resonance, phase noise dominates while at resonance, amplitude noise dominates. Between these two regimes, there is a frequency band where both noise sources have similar contributions (and a set of two frequencies where both contributions are exactly equal).

We recover here a fundamental concept of quantum mechanics. The optical field used to probe the system has some intrinsic noise from its quantum nature. We may decrease the impact of this noise by increasing the strength of the measurement. But increasing the strength means increasing the number of photons, which will disturb the system so we reach a fundamental limit called the Standard Quantum Limit (SQL). We will call the frequencies at which QSN and QRPN have equal contribution the SQL frequencies.

But as radiation pressure fluctuations are proportional to the amplitude quadrature of the incoming field a_1^{in} and quantum shot noise fluctuations are proportional to the phase quadrature a_2^{in}, sending an input field with reduced fluctuations in one of those quadratures (such as the squeezed beam generated by a sub-threshold OPO) allows us to perform a sub-SQL measurement (see Fig.II.19).

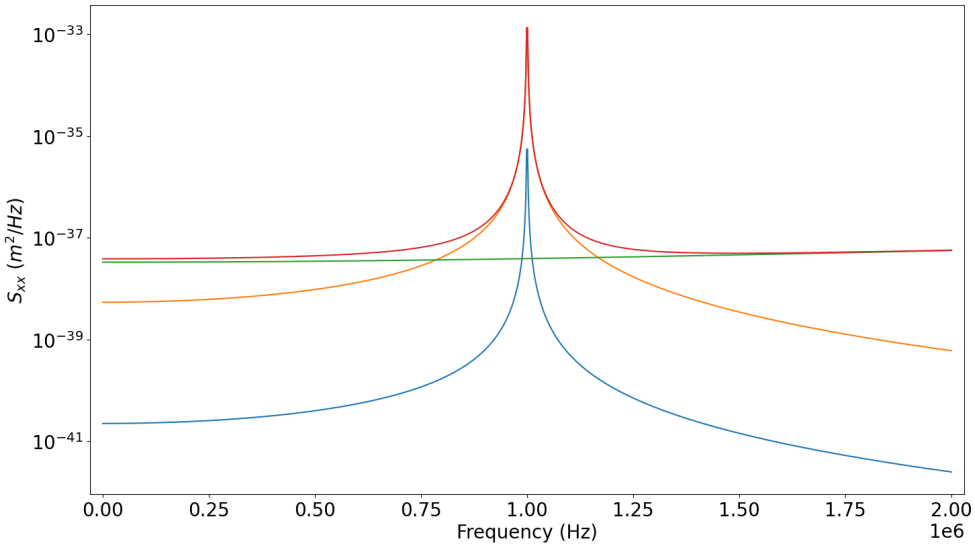

Fig. II.18 **An oscillator dominated by quantum noise. Noises in the position measurement of a macroscopic mechanical resonator with $Q = 10^6$, $\Omega_m/2\pi = 1$ MHz and $m_{eff} = 100$ ng. The blue curve represents the thermal displacement noise for an environment temperature of 10 mK, which is negligible compared to quantum radiation pressure noise (orange curve) for input optical power of $10\,\mu$W at 1064 nm. The green curve represents QSN, which dominates below 750 kHz and above 1.25 MHz.**

II.5.5 The rotation cavity transfer function

We have shown that the measurement of the resonators displacement can be limited by the SQL if thermal noise can be neglected. We have also shown how a squeezed state of light could be created by an OPO and how this state could allow a sub-SQL measurement over a specific frequency range.

Here, I will show how using the phase response of an optical cavity we can rotate the angle of the squeezing ellipse as a function of the mechanical frequency Ω. The goal is to have amplitude squeezing at frequencies close to the mechanical resonance of the oscillator (where QRPN dominates) and phase squeezing at frequencies far from the resonance (where shot noise dominates). Full details on calculations can be found in [46]

Let's consider a perfectly squeezed state represented by the following matrix:

$$v_{sqz} = \mathbf{R}_\psi \begin{bmatrix} e^\sigma & 0 \\ 0 & e^{-\sigma} \end{bmatrix} \mathbf{R}_\psi^\dagger. \tag{II.132}$$

We have shown in section II.3.9 that the effect of a cavity on such state can be written as

$$\mathbf{T}_{rc} = \mathbf{A}_2 \cdot \begin{bmatrix} r_{rc}(+\Omega) & 0 \\ 0 & r_{rc}^*(-\Omega) \end{bmatrix} \cdot \mathbf{A}_2^{-1}, \tag{II.133}$$

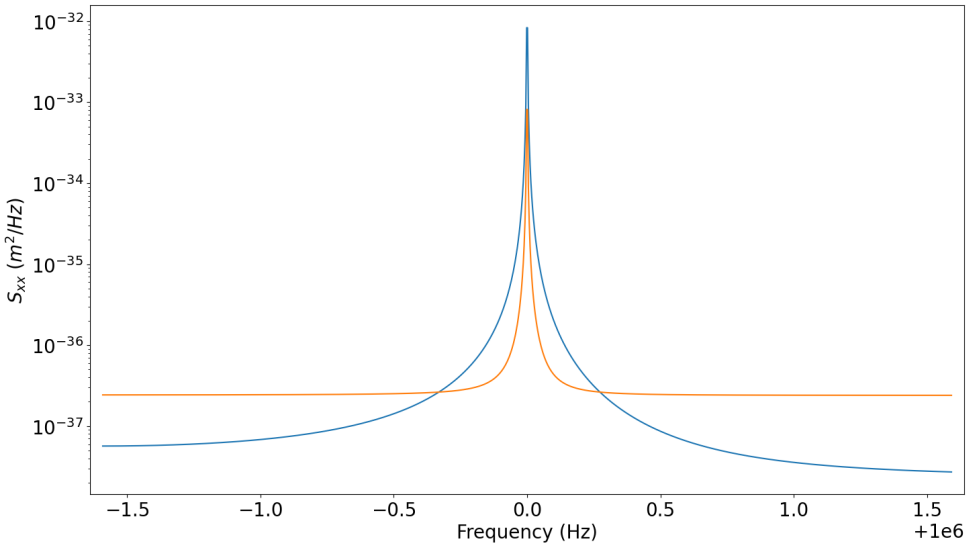

Fig. II.19 *Noises in the position measurement of a macroscopic mechanical resonator for a squeezed input field (7 dB of antisqueezing, 4 dB of squeezing). For the blue curve, the phase quadrature is squeezed so QSN is reduced but QRPN is increased, while for the orange curve, the amplitude quadrature is squeezed: QRPN is reduced while QSN is increased.*

with $r_{rc}(\Omega)$ the frequency-dependent cavity transfer function:

$$r_{rc}(\Omega) = 1 - \frac{2-\epsilon}{1+i\xi(\Omega)} = \frac{\epsilon - 1 + i\xi(\Omega)}{1+i\xi(\Omega)}. \tag{II.134}$$

To write things in a more comprehensible manner, we will define the amplitude and phase of the response function as

$$\rho_{rc}(\Omega) = |r_{rc}(\Omega)| = \sqrt{1 - \frac{(2-\epsilon)\epsilon}{1+\xi(\Omega)^2}} \tag{II.135}$$

and

$$\alpha_{rc}(\Omega) = \arg(r_{rc}(\Omega)) = \arg(-1+\epsilon+\xi^2(\Omega) + i(2-\epsilon)\xi(\Omega)). \tag{II.136}$$

We can now write the transfer matrix as

$$\mathbf{T}_{rc} = e^{i\alpha_m}\mathbf{R}_{\alpha_p}(\rho_p\mathbf{I} - i\rho_m\mathbf{R}_{\pi/2}), \tag{II.137}$$

where

$$\alpha_\pm = \alpha_{rc}(\pm\Omega), \quad \rho_\pm = \rho_{rc}(\pm\Omega), \tag{II.138}$$

$$\alpha_{\substack{p\\m}} = \frac{\alpha_+ \pm \alpha_-}{2} \quad \text{and} \quad \rho_{\substack{p\\m}} = \frac{\rho_+ \pm \rho_-}{2}. \tag{II.139}$$

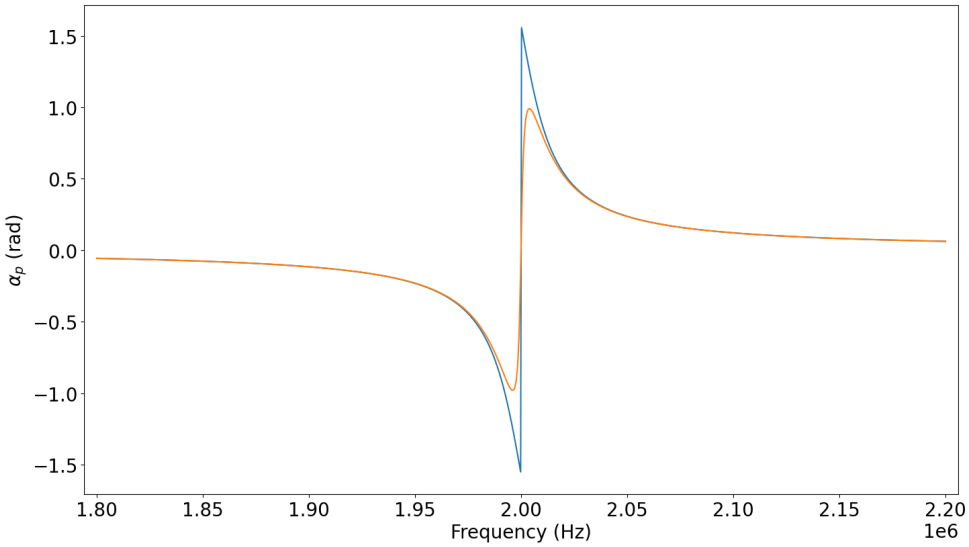

Fig. II.20 *Rotation angle α_p of the squeezing ellipse for a lossless RC detuned by 2 MHz (blue curve, with ($T_{in} = 1,000$ ppm) and for a lossy cavity (orange curve, additional losses $T_{out} = 100$ ppm).*

For a lossless cavity, we have $\epsilon = 0$ so $\rho_p = 1$ and $\rho_m = 0$, so the transfer matrix is just a rotation operation by α_p with the addition of an overall phase for both quadratures.

For a squeezed state, this operation consists of a rotation of the ellipse of squeezing which is exactly what is required. However for a lossy cavity, the second term will mix the quadratures of the squeezed state, adding antisqueezing to squeezing. The angle of rotation of the ellipse can be written as

$$\alpha_p = \text{atan}\left(\frac{(2-\epsilon)\gamma_{fc}\Delta\omega_{fc}}{(1-\epsilon)(\kappa_{fc}/2)^2 - \Delta\omega_{fc}^2 + \Omega^2}\right), \tag{II.140}$$

for small value of ϵ, i.e. low losses II.20. By carefully choosing the detuning of the cavity such that it matches the resonance frequency of the mechanical resonator, we can switch from phase squeezing outside of the mechanical resonance to amplitude squeezing close to the resonance. Finally, if the RC bandwidth matches the SQL frequency interval between the two frequencies at which QSN and QRPN have equal contributions, we can reduce the quantum noise over the entire bandwidth of the measurement as shown on figure II.21.

II.6 Optomechanical cooling of a macroscopic mechanical resonator

Optomechanical coupling, combined with quantum fluctuations of the light field, enforces quantum limits in continuous position measurements, which tends to lower the sensitivity of these measurements in any given experimental configuration. But optomechanics can

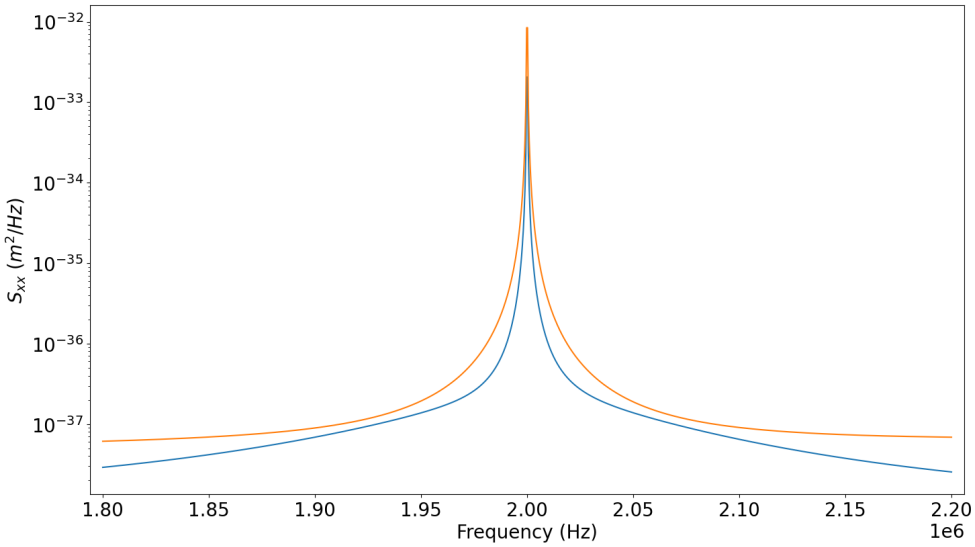

Fig. II.21 *Noise displacement spectrum for a measurement performed on a micro-resonator ($Q = 10^6$, $m_{eff} = 100$ ng, $\Omega_m/2\pi = 2$ MHz) with 10 µW of input optical power at 1064 nm. In orange we see the effect of the two quantum noises for a coherent field and in blue, we see the reduced noise for a frequency-dependent squeezed field. The squeezed field is created by a perfectly frequency-independent squeezed state (6 dB of squeezing) filtered by a RC with a bandwidth matching the SQL frequency interval of the optomechanical system and a detuning matching the mechanical resonance frequency of the resonator. We see an overall reduction of noise over the whole spectrum.*

also be useful in a different context. In an experimental situation where quantum limits are negligible compared to the thermal noise level, it can be used to lower the effective temperature of a mechanical system, either by direct coupling of the resonator to the light field, which corresponds to an additional bath at zero or near-zero temperature, or by taking advantage of the displacement sensitivity of the position measurement to counteract in real time the driving of the resonator by the thermal bath. In this section, I will present both mechanisms.

II.6.1 Radiation pressure cooling

We will see in this subsection how the radiation pressure of the intracavity field in a detuned optical cavity can create an additional damping of the resonator.

Considering the first order of equation (II.68), we get :

$$\delta\dot{\hat{a}}(t) = \left(i\Delta - \frac{\kappa}{2}\right)\delta\hat{a}(t) + \sqrt{\kappa_{in}}\delta\hat{a}_{in}(t) + 2ik\bar{a}\delta x(t). \tag{II.141}$$

Using the one-photon formalism in Fourier space (and giving up the δ for notation simplicity), we get:

$$\left(\frac{\kappa}{2}+i(\Delta-\Omega)\right)\hat{a}_+[\Omega]=\sqrt{\kappa_{in}}\hat{a}^*_{in+}[\Omega]+2ik\bar{a}x[\Omega] \tag{II.142}$$

$$\left(\frac{\kappa}{2}-i(\Delta+\Omega)\right)\hat{a}^*_-[\Omega]=\sqrt{\kappa_{in}}\hat{a}^*_{in-}[\Omega]-2ik\bar{a}x[\Omega] \tag{II.143}$$

$$\chi_m(\Omega)^{-1}x[\Omega]=-\frac{2\hbar k}{\tau}\bar{a}(\hat{a}_+[\Omega]+\hat{a}^*_-[\Omega])+F_T[\Omega]. \tag{II.144}$$

We see from the first two equations that the optomechanical interaction creates two sideband at frequencies $\pm\Omega_m$ on top of vacuum fluctuations of the input field that are white noise present at all frequencies.

We can now write the radiation pressure fluctuations as :

$$\delta F_{RP}[\Omega]=-\frac{4\hbar k^2\bar{a}^2}{\tau}i\left(\frac{1}{\kappa/2+i(\Delta-\Omega)}-\frac{1}{\kappa/2-i(\Delta+\Omega)}\right)x[\Omega] \tag{II.145}$$

$$=-\frac{4\hbar k^2\bar{a}^2}{\tau}\left(\frac{\Delta+\Omega}{(\kappa/2)^2+(\Delta+\Omega)^2}+\frac{\Delta-\Omega}{(\kappa/2)^2+(\Delta-\Omega)^2}\right)x[\Omega] \tag{II.146}$$

$$+i\frac{4\hbar k^2\bar{a}^2}{\tau}\left(\frac{\kappa/2}{(\kappa/2)^2+(\Delta+\Omega)^2}-\frac{\kappa/2}{(\kappa/2)^2+(\Delta-\Omega)^2}\right)x[\Omega] \tag{II.147}$$

Here, we are mainly interested in the effect of radiation pressure close to the mechanical resonance frequency. Since we are dealing with a high quality factor resonator, we can assume that radiation pressure force is constant and equal to $\delta F_{RP}[\Omega_m]$. If we now sweep the cavity detuning Δ, we will see two sideband added to the resonance peak at $\pm\Omega_m$ corresponding to the optomechanical interactions. Those can be seen as photon-phonon interaction process where a photon at ω_0 absorbs a phonon from the oscillator creating a photon at $\omega_0+\Omega_m$, or emits a phonon in the oscillator creating a photon at $\omega_0-\Omega_m$ (II.22).

In our experiments, the mechanical resonant frequency is in the MHz range while the cavity bandwidth is in the 50 MHz range. This is the unresolved sideband regime (also known as the bad cavity limit in quantum optics experiments with atoms), where the two sidebands created by the motion of the mirror are within the cavity resonance linewidth. We then have a force term with a real and complex part that can be seen as an "optical spring" term and an "optical damping" term (II.23). The optical damping term can be written as:

$$\Gamma_{opt}=-g_0^2\frac{P}{\hbar\omega_L}\frac{4\kappa\kappa_{in}\Delta\Omega_m}{(\Delta^2+\kappa^2/4)^3}, \tag{II.148}$$

Where $g_0=Gx_{zpf}$ is the reduced optomechanical coupling which is the product of the optomechanical constant $G=\frac{\partial\omega_{cav}}{\partial x}$ (equal to $\frac{2k}{\tau}$ for a linear Fabry-Perot cavity), and $x_{zpf}=\sqrt{\frac{\hbar}{2m_{eff}\Omega_m}}$ the zero-point displacement fluctuations of a quantum harmonic oscillator. Note the additional damping requires the cavity to be detuned: for a resonant cavity indeed, thermal motion doesn't create any modulation of the intracavity radiation pressure and hence, the damping term cancels.

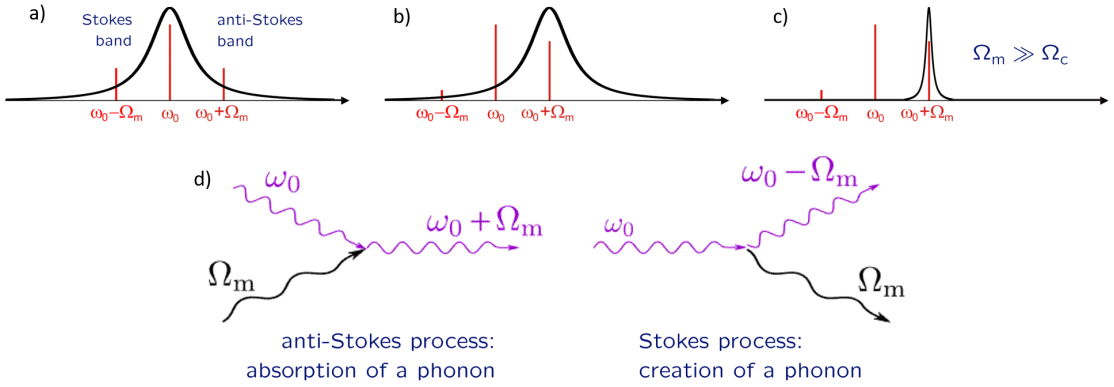

Fig. II.22 *a) Cavity response function represented with the two Stokes and anti-Stokes band for a cavity at resonance. The two processes are present but have no mechanical effect. b) For a detuned cavity, one of the processes is enhanced by the cavity response and has a mechanical effect (here absorption of a mechanical phonon). c) The resolved side-band regime where the cavity response is narrow enough to select only one of the processes. This condition is required to reach the ground state using this cooling principle and is not met for a macroscopical resonator in a standard Fabry-Perot cavity. d) Feynman diagrams of the two optomechanical processes.*

Because of the additional damping term, the resonator is no longer at thermal equilibrium and the equipartition theorem now becomes:

$$\frac{1}{2}m_{eff}\Omega_{eff}^2 < \delta x^2 >= \frac{1}{2}k_B T_{eff} \tag{II.149}$$

where T_{eff} is the effective temperature of the resonator motion and Ω_{eff} the optically-shifted resonance frequency of the oscillator. As the thermal Langevin force is not affected by the optical field, we write:

$$S_F^{th} = 4k_B T_{env} m_{eff}\Gamma_m \tag{II.150}$$

where T_{env} is the equilibrium temperature of the environment. If we use the relation (II.117), we can relate the two temperatures and we get:

$$T_{eff} = T_{env}\frac{\Gamma_m}{\Gamma_m + \Gamma_{opt}}. \tag{II.151}$$

The radiation pressure "cools" the motion of the resonator, as it adds dissipation to the system and reduces the effective temperature of the motion for (at least) one specific mode. The thermal peaks represented on figure II.23 gets lower as the temperature is reduced and wider as the damping is increased. As the thermal energy of this mode is reduced, it gets closer to its quantum-mechanical ground state. To quantify how close it gets, it is useful to compare its thermal energy to the quantum scale of energy of a

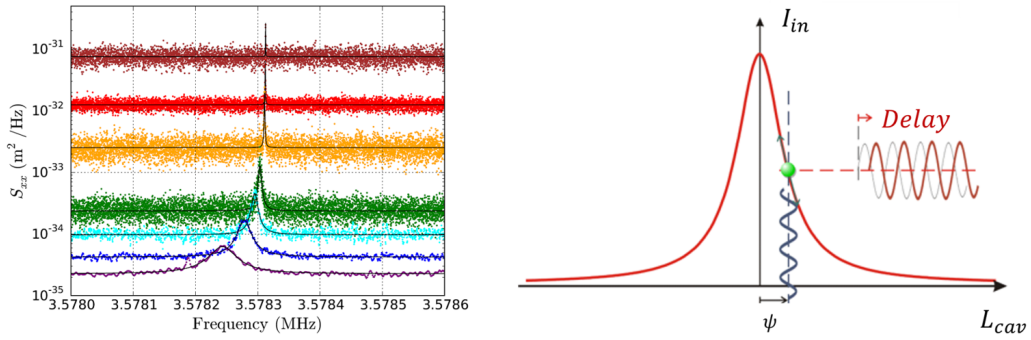

Fig. II.23 *Right : Experimental Noise displacement spectra for a micro-pillar for a detuned cavity. The different coloured curves correspond (from top to bottom) to an incident optical power ranging from 0.2 to 25 µW. We can see as we increase the optical power that the mechanical resonance peak becomes both wider, due to the optical damping, and lower as we are reducing the effective temperature of the mechanical mode. We also see that the resonant frequency is shifted as expected from the optical spring effect. Figure from [19]. Left : Conceptual scheme of side-band cooling. The phase modulation of the cavity due to the mirror's motion induces intensity fluctuations with some delay due to the cavity response function. This delay causes the radiation pressure force to act as a damping force.*

quantum harmonic oscillator and write:

$$\frac{1}{2}k_B T_{eff} = n_{ph}\hbar\Omega_{eff}, \tag{II.152}$$

where n_{ph} is the "number of phonons" of the oscillator. This definition is not rigorous and should mainly be seen as a way to measure how far the system is from its quantum ground state.

It is easy to see on Eq. (II.148) that for a negative detuning, Γ_{opt} is positive so the optical field adds dissipation to the mechanical resonator while adding negligible fluctuations. So it can be used to cool the motion of the resonator. Optimal cooling is reached for $\Delta = -\kappa/2$ and we then have

$$\Gamma_{opt}^{max} = 16 g_0^2 \frac{P}{\hbar\omega_L}\frac{\kappa_{in}\Omega_m}{\kappa^4}, \tag{II.153}$$

which gives us the maximum cooling rate for a given optical power. We will see in the experimental setup description part that the amount of optical power we can inject into the cavity is limited by the optical absorption of the mirrors: at one point, the temperature of the resonator starts to increase with the optical power. I will now present a cooling method with a better efficiency.

II.6.2 Feedback cooling

The calculation presented is this section are based on ref. [47]. The idea of this technique is now to measure the displacement $x(t)$ of the resonator in real time and use this information

to apply a feedback force that acts as a damping term, by modulating the intensity of an additional laser beam such that:

$$F_{RP}(t) = -g m_{eff} \Gamma_m \frac{\mathrm{d}x(t)}{\mathrm{d}t}, \tag{II.154}$$

where g is the feedback gain of the loop. This would be the ideal case but we have to consider that our measurement is not ideal and some noise $x_n(t)$ is going to be added as well when performing our measurement. In that case, the effective equation of motion is:

$$m_{eff}\left[\ddot{x}(t) + (1+g)\Gamma_m \dot{x}(t) + \Omega_m^2 x(t)\right] = F_{th}(t) - g m_{eff} \frac{\mathrm{d}x_n(t)}{\mathrm{d}t}. \tag{II.155}$$

If we now compute the power spectral density, we get:

$$S_{xx}[\Omega] = \frac{1}{(\Omega_m^2 - \Omega^2)^2 + (1+g)^2 \Gamma_m^2 \Omega^2}\left[\frac{2k_B T_{env}}{m_{eff}}\Gamma_m + g^2 \Gamma_m^2 \Omega^2 S_{xx}^N\right], \tag{II.156}$$

where S_{xx}^N is the power spectrum of the measurement noise and we used the Fluctuation-Dissipation theorem to compute $S_{xx}^{F_{th}}$. Here, we can safely assume from our measurements that we are limited by quantum shot noise which is independent from Ω. So we have:

$$S_{xx}^N[\Omega] = S_{xx}^{QSN}[\Omega] = \frac{\lambda^2}{256\mathcal{F}^2(P/\hbar\omega_L)} \tag{II.157}$$

We can use the equipartition theorem to link S_{xx} and T_{eff}, and we get:

$$T_{eff} = \frac{T_{env}}{1+g} + \frac{m_{eff}\Gamma_m \Omega_m^2}{4k_B}\left(\frac{g^2}{1+g}\right) S_{xx}^{QSN} \tag{II.158}$$

Here, the parameter to optimize is no longer the detuning as it was for intracavity radiation pressure cooling but the gain g of our feedback loop. The lowest effective temperature is obtained for:

$$g_{opt} = 2\sqrt{\frac{k_B T_{env}}{m_{eff}\Gamma_m \Omega_m^2 S_{xx}^{QSN}}} \tag{II.159}$$

and we get :

$$T_{min}^{fbc} = \sqrt{\frac{m_{eff}\Gamma_m\Omega_m^2}{k_B} S_{xx}^{QSN} T_{env}} = \frac{\lambda}{16\mathcal{F}}\sqrt{\frac{m_{eff}\Gamma_m \Omega_m^2 T_{env}}{k_B(P/\hbar\omega_L)}}. \tag{II.160}$$

We can now compare T_{min}^{fbc} and T_{min}^{sbc} as a function of the optical power for the characteristics of the two resonators used in this work:

In chapter III, I will present experiments where the detected displacement noise is strongly dominated by thermal noise and such a technique is applied to get closer to the quantum ground state of the resonator.

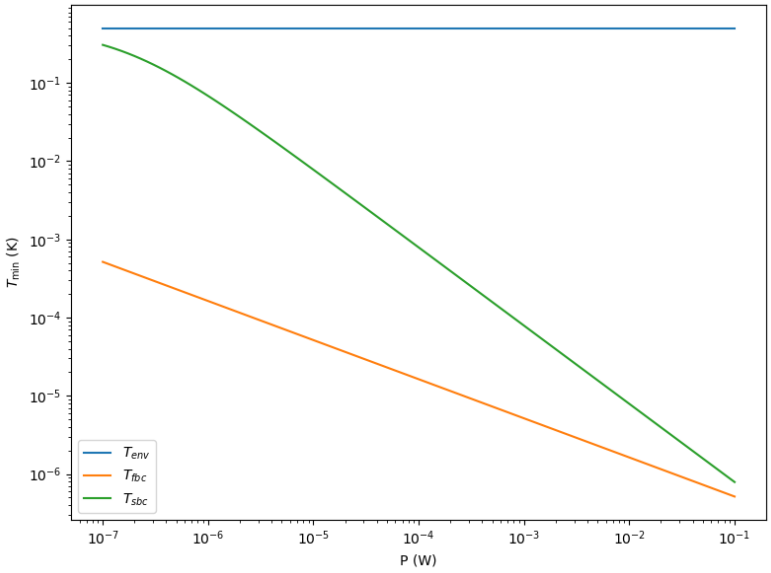

Fig. II.24 *Comparison between the minimal achievable temperature using radiation pressure cooling and feedback cooling as a function of the input optical power. The following parameters are used:* $T_{env} = 0.5\ K$, $\Omega_m/2\pi = 3.6\ MHz$, $\mathcal{F} = 79,000$, $m_{eff} = 33.5\,\mu g$, $\kappa = 205\ MHz$, $\kappa_{in} = 90\ MHz$ *and* $Q = 7 \times 10^7$. *We see that for 25* μW, *we get, with sideband cooling, the same temperature of 3 mK that was experimentally measured in the group by Leonard Neuhaus [19]. For the same amount of optical power, we go to two orders of magnitude below with feedback cooling assuming we are only limited by Quantum Shot Noise in the measurement hence the motivation to go from sideband cooling to feedback cooling.*

Chapter III

Cooling a µg-scale optomechanical resonator close to the quantum ground state

In previous experiments performed at LKB, a 1-mm long quartz µ-pillar (resonance frequency of 3.6 MHz and effective mass of 30 µg) was cooled down to 3 mK, which corresponds to a mode thermal occupancy of 20 phonons, using optomechanical sideband cooling. In the course of Rémi Metzdorff's PhD, the use of feedback cooling pushed this number further down to 6 phonons. Unfortunately, this result was not reproducible so we considered using a new kind of oscillator: a silicon wheel resonator, that I have characterized and with which I have performed the feedback cooling experiments discussed in this chapter. Silicon wheel resonators have much more reproducible mechanical properties than quartz micro-pillars, so they are promising to reach the ground state for macroscopic resonators.

I will begin this chapter by motivating such cooling experiments with µg-scale resonators. I will then describe the different parts of the experiments: the mechanical resonators, the cryogenic moving mirror cavity, the full optical detection setup, and I will eventually present the experimental results obtained.

III.1 Introduction and motivations

Optomechanics has been extremely successful to cool macroscopic (man-made) optomechanical systems but almost all experiments were performed with extremely tiny systems, with mass in the ng range and below. Such systems are indeed very sensitive to radiation pressure and motion is in the MHz band and above, which naturally isolates them from many classical noise sources. Miniaturization is also natural for integrated systems, with possible applications in quantum information.

On the fundamental physics front, a fascinating perspective is the investigation of the decoherence of a quantum superposition of such a mechanical object under the effect of gravity, which is however negligible for most resonators demonstrated in the QGS [10, 49].

If we consider a massive object in a quantum superposition of two states separated

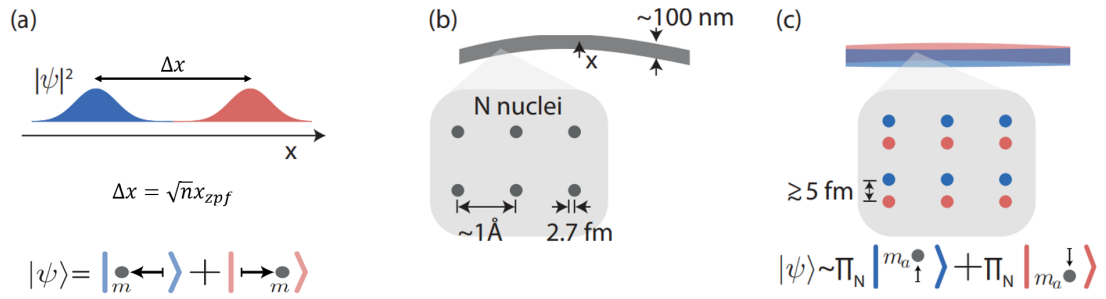

Fig. III.1 **The Diosi-Penrose model for gravitational decoherence of a quantum superposition of a mechanical resonator**. *(a) Probability distribution of a cat state. The resonator is in a quantum superposition between the two x positions, so time is not well defined in the superposition vicinity. (b) For a resonator composed of N nuclei, the macroscopic superposition state can be viewed as a quantum superposition of nuclei states, simultaneously displaced up and down (c). Figure adapted from [48].*

by a distance Δx, there is an ambiguity on how time is defined in the vicinity of that superposition. Indeed, as time is affected by the nearby mass distribution, it should also be in some sort of a state superposition. In the model proposed by Diosi and Penrose (see [48] for an illuminating elementary exposition and [50, 51] for the original papers), the different local time scales give rise to a gravitational decoherence time:

$$t_{GR} \approx 3 \times 10^{-15} \left(\frac{1\,\mathrm{kg}}{m} \right) \mathrm{s}, \tag{III.1}$$

that only depends on the effective mass m of the resonator. This is valid as soon as the distance between the two states is larger than the diameter of the nuclei the resonator is made of. This sets a size limit on the cat state (in terms of mean phonon number n):

$$n \gg \left(\frac{\Delta x}{2 x_{zpf}} \right)^2. \tag{III.2}$$

To create such a non-Gaussian state, QGS is only a starting point: one would also need to couple the resonator to a highly non-linear system, ideally a qubit and such experiments are also conducted at LKB with a nm-scale membrane coupled to a fluxonium qubit.

For a resonator in such a state, the coupling to the thermal bath will also induce decoherence, with a characteristic time

$$t_{coh} = \frac{1}{2(2n_{th}+1)n\gamma_m}, \tag{III.3}$$

where n_{th} is the mean phonon number of the bath and γ_m is the mechanical damping rate of the resonator. One may expect to see some gravitational decoherence effect if the gravitational decoherence time t_{GR} is shorter than the thermal time t_{coh}. Macroscopic resonators with a large effective mass are obviously good candidates. However, the

	Micro-pillar	Micro-disk
Material	quartz	silicon
Effective mass	33 µg	120 µg
Resonance frequency	3.6 MHz	280 kHz
Quality factor at 1 K	3×10^6	10^6

Table III.1: Main mechanical characteristics of the resonators used during the PhD.

required size of the cat state will be large because of the very low value of their QGS position fluctuations x^2_{zpf}. Figure III.2 presents both decoherence times computed for a representative set of optomechanical platforms. Despite its relatively low mass, the most promising platform is by far the SiN nanomembrane because of the incredible success recently obtained in designing ultra-high Q resonators. The µ-pillar is however one of the few promising systems for such experiments as the ratio t_{GR}/t_{coh} is favourable, at least for the $Q = 7.10^7$ highest value demonstrated (see next section). For the wheel resonator, we find a gravitational decoherence time of 23 ns and a thermal decoherence time of 36 ns for a quality factor of 3 millions, to be compared to the common measured value around 1 million, though at a thermalization temperature of 100 mK. The big challenge for such systems would be to create a cat state with a sufficient size, with $n \approx 10^5$. The first step on this experimental journey is however the demonstration of the QGS and I will present in the following sections the progress made during my PhD using both cryogenic and optomechanical cooling.

III.2 Description of the experiment

The experiments discussed in this chapter involve a number of systems. By order of appearance on stage, I will successively describe the mechanical resonators, the high-finesse optical cavity they are encapsulated in, the dilution cryostat where the cavity is housed, the optical measurement schemes and the characterization steps of the whole setup.

III.2.1 The mechanical resonators

I have studied two different geometries of optomechanical resonator, but both consist of high mechanical quality factor resonators carved on thin wafer with decoupling shields to protect them from clamping losses. They are also both eventually coated with very high-reflectively coating (with a residual transmission ≃10 ppm) at 1064 nm. With the input mirror, they constitute a cavity with an optical finesse of 60,000.

a) The micro-pillar resonator

The mm-long micro-pillar is fabricated in quartz, a material with very low intrinsic mechanical loss. An important issue is related to the required etching using hydrofluoric acid (HF) which is not as clean as silicon etching by Deep Reactive Ion Etching (DRIE) for example. The etching has been performed at ONERA and the coatings at LMA. The triangular section of the pillar is imposed by the quartz crystalline structure.

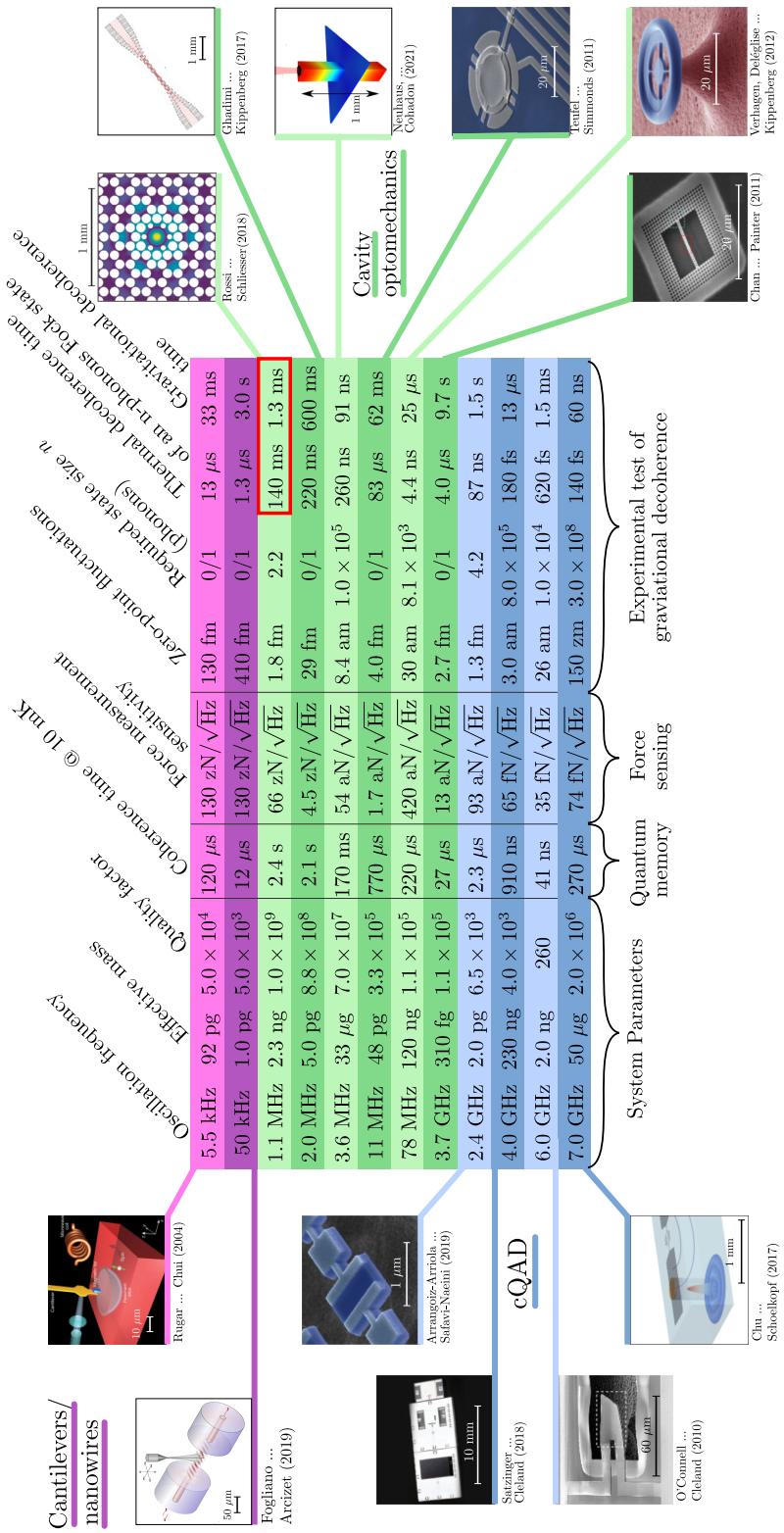

Fig. III.2 *Optomechanical resonators (ordered by increasing resonance frequency) and figures of merit for different applications: quantum memory, force sensing and experimental test of gravitational decoherence. Besides the SiN membrane, the μ-pillar is the only resonator to display a gravitational decoherence time (91 ns) shorter than its thermal decoherence time (260 ns), due to its very high effective mass. Value taken from [52, 53, 54, 55, 56, 57, 58, 59, 19, 29, 49, 60].*

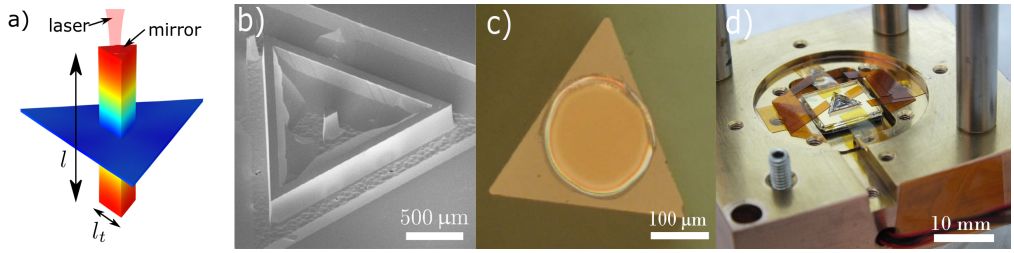

Fig. III.3 ***The micro-pillar resonator***. *a) Finite-element simulation of the fundamental elongation mode. Displacement is represented by the color scale. Mechanical stress is minimized at the mirror location. b) Scanning Electron Micrograph view of the pillar and its isolation frame. c) Optical view of the mirror coated on the top face of the resonator. d) View of the resonator glued on copper pieces coated with gold and ready to be mounted inside the cryostat.*

The elongation mode (see Fig. III.3) of the pillar had the advantage of a high mechanical resonance frequency (typically 3.6 MHz for 1 mm) and a potentially ultra-high mechanical Q. Indeed, this specific mode maximizes the displacement of the mirror coated on the pillar end face, while minimizing the deformation of the mirror.This is ideal because the materials used for the dielectric coating unfortunately have high intrinsic mechanical losses: in this geometry, coated at a vibration antinode where stress is minimal, they only have little impact on the effective damping of the resonator. The demonstrated Q value indeed went up to 70 millions demonstrated, though only on a single sample. The samples indeed had very different properties from one to the other, depending on the details of the etching of the quartz wafer, which was not reproducible. Apart from this great sample, most of the samples displayed medium quality factors (typically $Q \simeq 100,000$) and bad thermalization with the cryostat.

These resonators also displayed low-frequency modes (see Fig. III.4), which were strongly coupled to the optical mode of interest, such that the optical power stored in the cavity would easily start a photothermal parametric instability [61], preventing the cavity locking and adding noise to the displacement spectrum.

Taking into account all these disadvantages, we decided not to re-fabricate such resonators but rather to try the wheel resonator designed by Francesco Marin at LENS, made with a different material, taking advantage of another mechanical mode geometry and benefiting from a standard microelectronics fabrication process.

b) The wheel resonator

The silicon wheel resonator has been adapted from the successive designs (see Fig. III.5) in Francesco Marin's group [62], with the highest possible frequency. For this purpose, resonators five times smaller than the ones originally used have been fabricated, the main limitation being the size of the mirror at the center which needs to be around 100 µm to prevent beam clipping (see Fig. III.6).

The wheel resonators have been fabricated using DRIE, that allows flat etching angle in silicon as opposed to potassium hydroxid (KOH) etching. The resonators have been designed to limit the number and the effect of the parasitic low-frequency modes mentioned

earlier and to maximize the displacement at the center of the wheel while minimizing stress (see Fig. III.5).

Unfortunately, they do have a low resonating frequency by a factor of ten, meaning that for the same temperature, the number of phonons is ten times higher. However, they have much more reproducible properties, and among the 10 samples we have tested, all had a quality factor around one million (see Table III.2). The two resonators that we measured inside the dilution cryostat had the same thermalization temperature around 1 K. With these resonators, we could also inject higher optical power into the cavity, due to the better thermalization.

We have performed ring-down measurement in a small circulation cryostat going down to 5 K as a function of temperature and we were able to measure the quality factors of 10 of those samples. Unfortunately, we believe that this low-cost cryostat doesn't thermalize the sample at 5 K but more probably around 20 or 25 K. When measuring the quality factor as a function of temperature, a maximum was reached at 125 K (see Fig. III.7).

Searching the literature for the value of the mechanical losses in silicon as a function of temperature, I have found that it strongly depends on the thermal expansion coefficient of silicon. At 125 K, there is a crystalline structure change in silicon and its thermal expansion becomes negative [63]. So at this turning point, the thermal expansion is zero and one can approach the losses that we would reach in a dilution cryostat. We used this measurement to obtain a better estimate of the quality factor at dilution temperatures.

III.2.2 Optical Setup

We use a 1064 nm Nd:YAG laser from Coherent. To suppress the relaxation peak of the laser around 1 MHz, we inject the laser through an optical mode cleaner in addition to the built-in noise eater of the laser. The mode cleaner is a triangular Fabry-Perot cavity with a round trip length of 84 cm and a finesse of 6,000, allowing for a low-pass cut-off frequency of 56 kHz (a complete description of an exact replica of this mode cleaner is given in section IV.3). This allows us to be limited only by quantum noise above 200 kHz. The laser is then split along the two polarizations : one will be frequency-shifted and used for PDH detection and the other is going through an amplitude modulator and used with

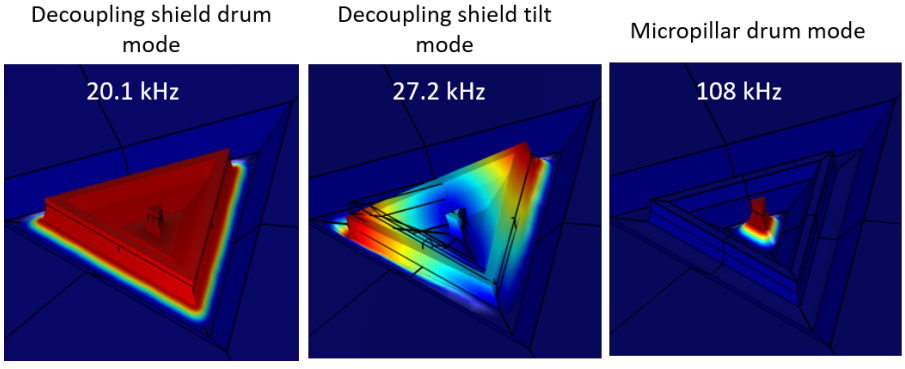

Fig. III.4 *Finite-element simulations of the parasitic low-frequency modes of the micro-pillar. For high optical power, vibrations at these frequencies drastically increase and make the cavity impossible to properly lock at resonance.*

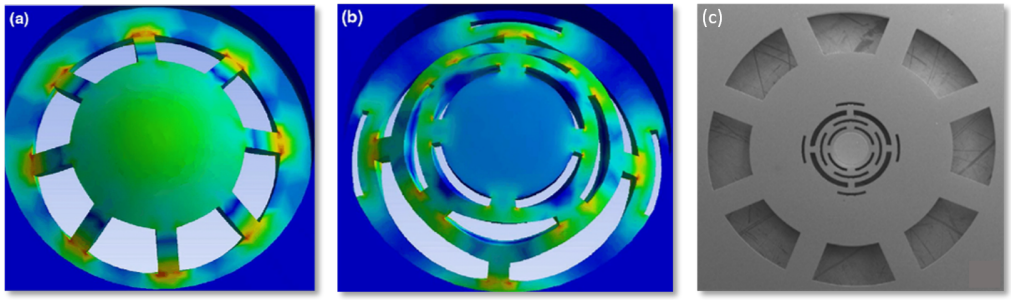

Fig. III.5 ***Design of the wheel resonators.*** *a) FEM of the first design of the wheel resonator: the mirror is supported by radial flexural springs and the central part (mirror location) is strongly bent. b) FEM of the low deformation design: the vertical displacement of the mirror is almost uniform thanks to the structure made of alternated torsional and flexural springs. The main advantage compared to the elongation mode of the pillar is the absence of tilting mode as the one represented in the middle of the figure III.4. c) Optical view of the wheel resonator before the optical coating step. Figure adapted from [62].*

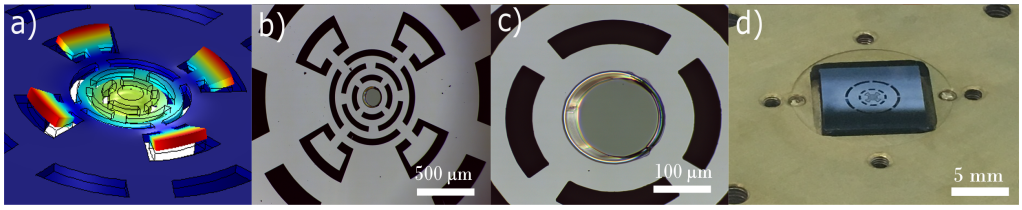

Fig. III.6 ***The LKB wheel resonator.*** *a) Finite-element simulation of the mechanical mode of interest. Displacements are represented by the color scale. b) and c) Views of the resonator taken with an optical microscope for various magnifications. d) View of the resonator glued on copper pieces coated with gold and ready to be mounted inside the cryostat.*

Sample name	Q at 2×10^{-4} mbar	Q at $T = 125$ K	Q at $T_{cryo} = 4.2$ K
W1564N1	71 000	800 000	290 000
W1572N3	76 000	575 000	405 000
W1570N2	76 000	770 000	700 000
W1566N2	78 000	890 000	640 000
W1556N2	76 000	940 000	650 000
W1570N1	60 000	344 000	420 000

Table III.2: **Measured quality factors of vibration mode under study, for various wheel resonator samples.** We use the fact that thermal expansion goes to zero at 125 K to have a better estimate of the quality factor at dilution temperatures. The temperatures indicated correspond to the one displayed by the cryostat thermometer and may differ from that of the samples, particularly at very low temperatures.

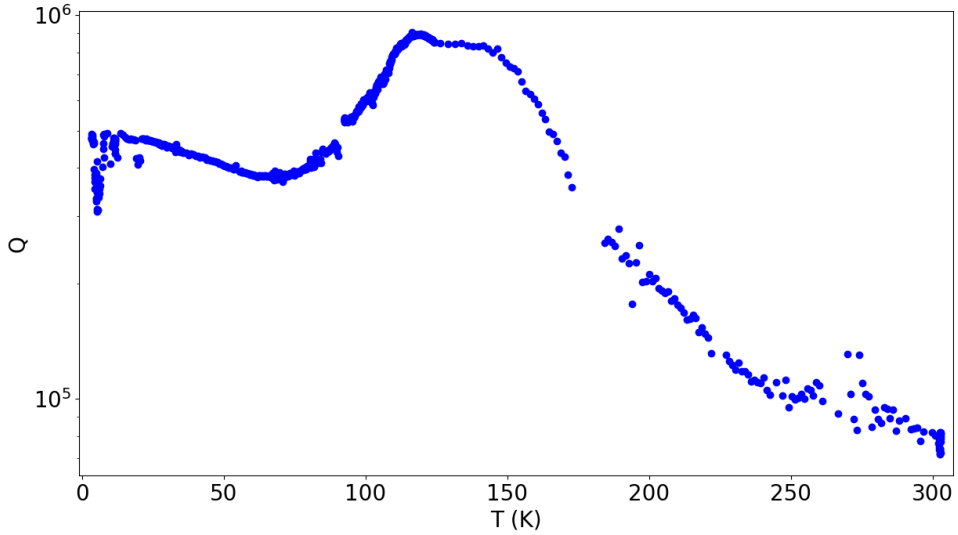

Fig. III.7 ***Variations of the mechanical quality factor of the wheel resonator with temperature***. *The maximum quality factor is reached around 125 K where the thermal expansion cancels. This measurement is performed in a small circulation cryostat, that can quickly reach low temperatures, to get a better idea of the quality factor vaue at dilution temperature. The temperature reported on the plot is the one displayed by the cryostat thermometer, though the resonator is most likely thermalised at a higher temperature.*

a homodyne detection scheme to apply a feedback force to the resonator motion from the displacement signal.

III.2.3 A resonator inside a high-finesse optical cavity

a) The input mirror

The moving mirror cavity is a 100-µm long plano-concave optical cavity. The input mirror is a curved mirror (with a radius of curvature (ROC) $\simeq$ 1 mm) carved in a 1-mm thick Suprasil fused silica sample. The concave spot has a typical diameter of 100 µm, engineered by a pulsed CO_2 laser (see Fig. III.9). It is then coated with a high-reflectivity dielectric coating (with several $\lambda/4$ doublets) with a transmission of 80 ppm. Such a mirror allows a 10-µm waist on the flat mirror of the cavity, compatible with the small transverse size of the mechanical resonator. A short cavity also proves to be more robust against misalignment and potential hybridization between the fundamental optical mode of interest and higher-order transverse optical modes.

b) Mounting an optical cavity inside a cryostat

The cavity design has been developed by two former LKB PhD students: Rémi Metzdorff and Leonhard Neuhaus. It is described in detail in their thesis but I give here a brief

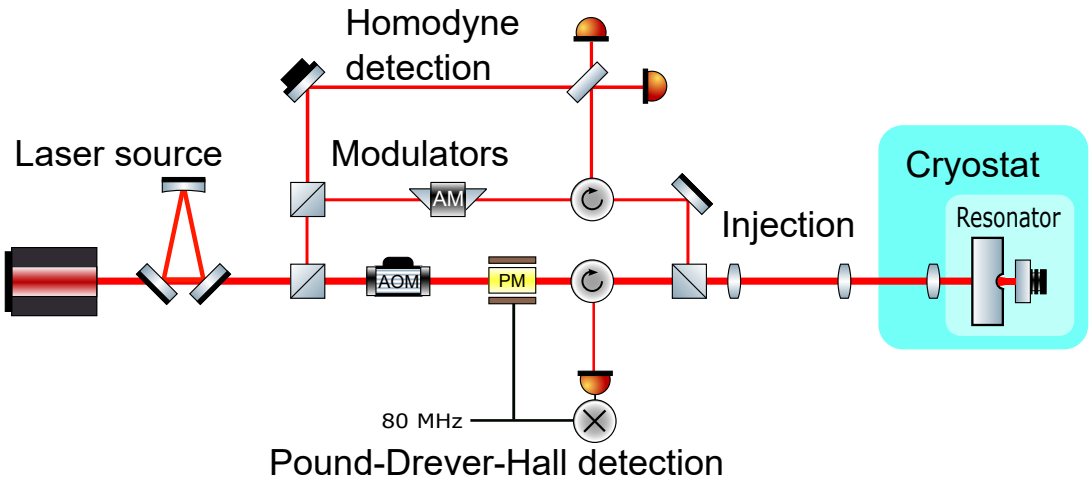

Fig. III.8 *Simplified optical setup. The two beams for the homodyne detection and the PDH detection have orthogonal polarisations and the PDH field is frequency-shifted by the acousto-optic modulator (AOM) to match the cavity birefringence so that both laser beams are resonant with the cavity, each on its own polarization axis. The beam of the homodyne detection is amplitude-modulated to apply the feedback force while the PDH is not and serves as an out-of-loop measurement.*

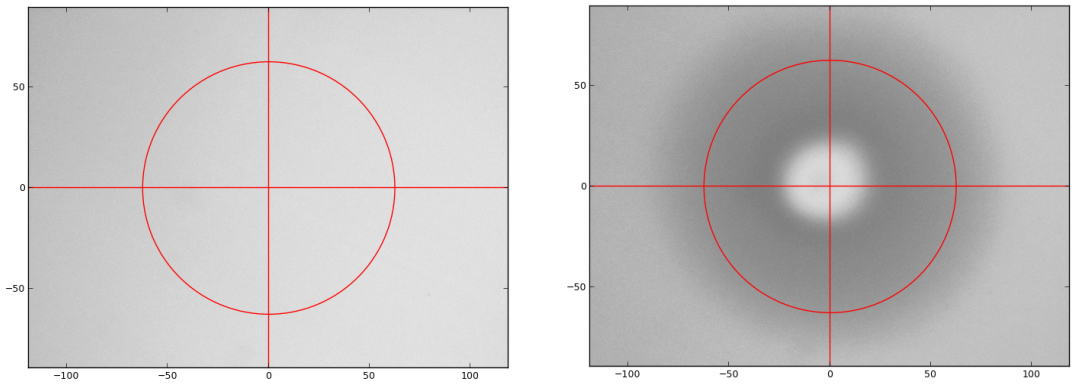

Fig. III.9 *Interferometric profile of a Suprasil sample before and after a CO_2 laser shot of 90 ms. We have obtained a concave structure with a 60-µm diameter and a radius of curvature of 1.3 mm.*

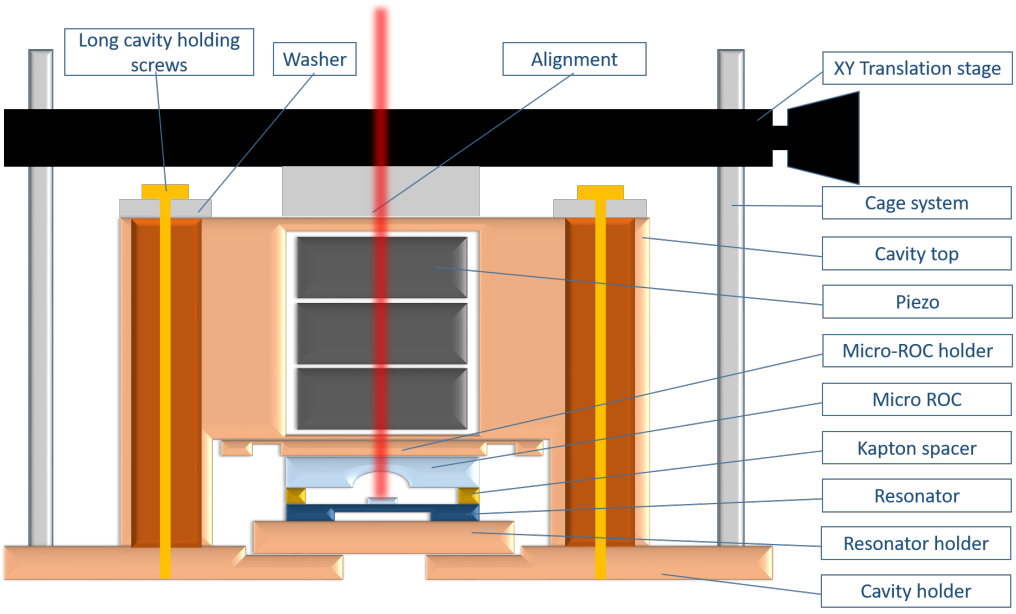

Fig. III.10 *A schematic side view of the moving mirror (FPM) cavity (not to scale).*

summary.

The cavity assembly process starts by glueing the samples onto a small copper piece that can be easily removed from the setup, in order to easily change sample. This is particularly useful because the sample properties can vary quite significantly from one to the other. We want to choose the resonator with the best quality factor and the micro-ROC that makes the highest finesse cavity. We glue the micro ROC on the "µROC support" (see Figs. III.10 and III.11) piece with black Stycast. For the wheel/pillar resonator, we first glue a frame in silcon/quartz on the "resonator support" to ensure a good thermalization of the sample before glueing the actual resonator also with black Stycast. We then mount the three piezos (PD080.3x from PI ceramics) in the "cavity top" piece using the "piezo alignment" piece to ensure that they are properly stacked. These piezos are used to tune the cavity length to resonance. We need to stack three of them to make sure we have at least more than one FSR when operating at dilution temperature (temperature at which their mechanical behaviour and displacement is reduced by the extreme temperature conditions).

We have found it is better to have them behind the mirror than behind the sample in order to avoid any parasitic piezoelectric effect (particularly for the quartz resonator). We then screw the "µROC support" on the "cavity top" and the "resonator support" on the "cavity holder" using 4 M1.6 screws in brass (which has a slightly higher thermal contraction coefficient than copper so it will keep the pieces tight when going to cryogenic temperatures). The cavity top is attached to an XY translation mount from Thorlabs connected to a cage system mounted on the cavity holder piece thanks to the "alignment" piece which is in dural.

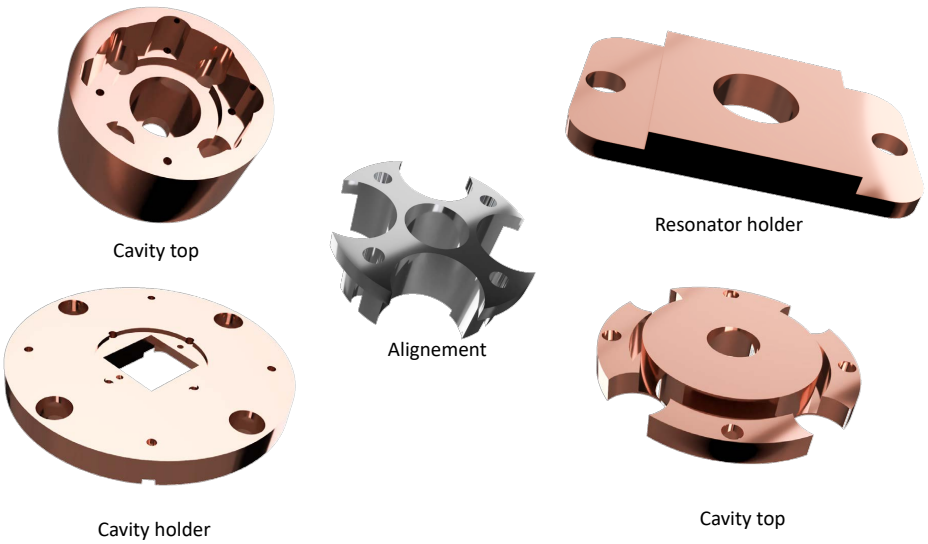

Fig. III.11 *3D views of the mechanical parts of the cavity. The different parts are not to scale from one to the other.*

c) Alignment

This setup allows to move the micro RoC with respect to the resonator while injecting a laser beam inside the cavity. In this way we can make sure that the two mirrors are on top of each other and that we are maximizing the finesse of the cavity. When the finesse is optimal, we can tighten the 4 long M2 screws that hold the cavity top with stainless steel washers (see Fig. III.12). To make sure we keep the alignment and the cavity length constant while going down in temperature, we place 137-µm thick Kapton spacers (seen on Fig. III.3(d)) between the two mirrors. The Kapton will only very slightly deform between room and cryogenic temperatures and will maintain the cavity aligned and the length around 100 µm.

The three piezoelectric transducers (PZT) ensure a displacement up to roughly 4 free spectral ranges (FSR) of the cavity at room temperature and just over 1 FSR at dilution temperature. To make sure that the Kapton is not too tight, we first mount the cavity without it and measure its length by measuring the FSR of the cavity. We aim for a length just under 127 µm to make sure that the Kapton is just slightly tight. This system allows us to have a cavity of finesse 60,000 inside the dilution fridge, with just 50 ppm of excess optical loss, and ensures an easier locking of the cavity length by the PZT by reducing the uncorrelated vibrations of the two mirrors. We end up with a cavity aligned with the proper length, optimized finesse and properly tightened Kapton spacers. We can then remove the XY translation mount to obtain a compact, high-finesse and dilution-robust cavity that we can mount in the dilution cryostat (see Fig. III.13).

d) The Horizontal dilution cryostat

Description The horizontal dilution cryostat has been built by Cryoconcept with custom specifications planned by Aurélien Kuhn. More details on the specifications and the

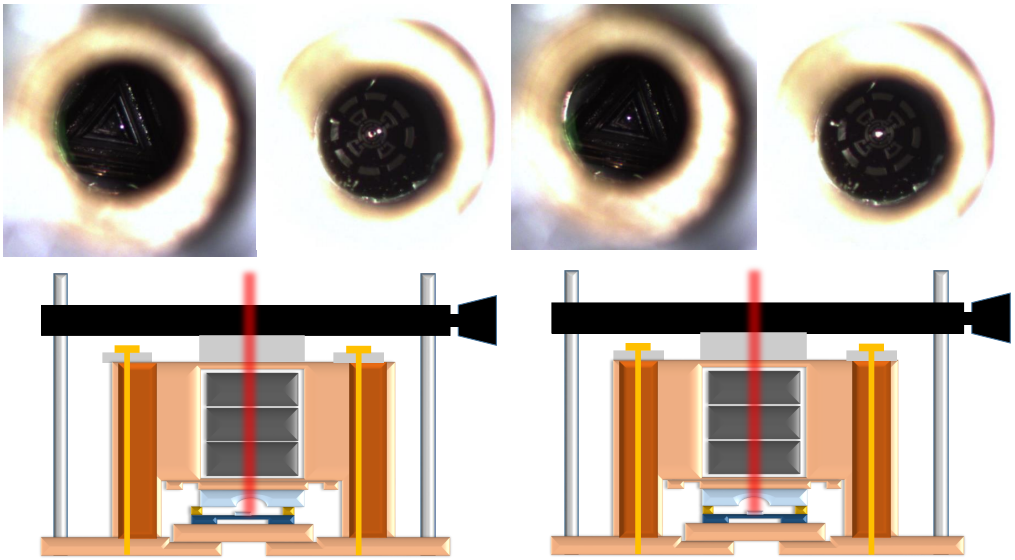

Fig. III.12 **Alignment procedure**. *On the left, the cavity is misaligned: two bright spots can be seen, which corresponds to the situation where the mirrors are not on top of each other for both the micro-pillar and the wheel resonator (see the picture below). The bottom part shows that the top part of the cavity can be moved with respect to the bottom part thanks to the XY translation mount. On the right, the cavity is "pre-aligned": the mirrors are visually on top of each other. This is sufficient to see optical modes, required for further alignment optimization.*

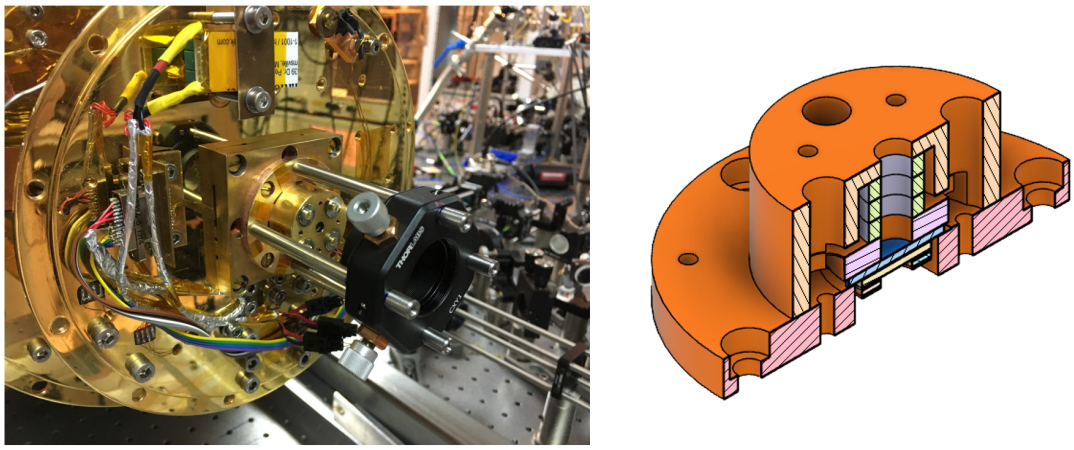

Fig. III.13 *Left : Picture of the cavity mounted in the cryostat with the mode-matching lens on the Thorlabs mount. Right : Sectional view of the mounted cavity, ready to be installed in the dilution cryostat.*

design of the cryostat can be found in [64]. A dilution cryostat uses a mixture of ^{3}He/^{4}He to reach a temperature well below 4 K, the boiling point of liquid Helium.

To reach 4 K, the cryostat has a liquid ^{4}He circulating circuit connected to a 20-l tank. When in dilution operation, the tank needs to be refilled after 27 hours maximum. The dilution circuit is a closed circuit that undergoes compression and decompression cycles that takes heat from the sample part and cools it down to 100 mK. Usually, dilution fridges are vertical to use gravity. In the LKB cryostat, an important constraint is to minimize the effect of the vibrations due to the boiling helium. With an horizontal cryostat, such vibrations are localized along the propagation axis of the beam inside the cavity. The two cavity mirrors and the mode-matching lens are all attached to the sample part of the cryostat (see Fig. III.13) so the vibrations affect as little as possible the beam position inside the cavity. The cryostat has 5 shields isolating the different stages, respectively at 300 K, 200 K, 100 K, 4 K and 100 mK (see Fig. III.14). The vacuum chamber has to be pumped below 10^{-4} mbar before starting the cool-down. The cool-down usually takes 14 hours to reach dilution temperature. While in dilution operation, the mixture is constantly filtered through an active carbon trap kept in liquid nitrogen. This keeps the mixture clean from impurity and parasitic gas, that will be liquefied in the trap, before sending it to the dilution circuit. The trap is in a tank of liquid nitrogen that has to be refilled every week. All the details on the dilution cryostat operation can be found in Rémi Metzdorff's thesis (in french) [65] and Leonhard Neuhaus's thesis [66].

Issues The base temperature used to be below 100 mK, but it has increased in recent runs. We are not sure yet if it comes from clogging of the dilution circuit or from losses of mixture. There is most likely a leak in the dilution circuit because it systematically clogs after one week of cryostat operation. But even after extensive leak tests we haven't been able to find it. I haven't had the time to make this final test but by plugging the leak detector to the vacuum chamber and letting the mixture circulate inside the cryostat, we should immediately see if some helium of the mixture goes inside the vacuum tank and is detected by the leak detector. The other possibility would be the presence of hydrogen in the mixture that won't be liquefied in the trap but that would liquefy in the dilution circuit. If this is a the case, a solution would be to add a filter in the dilution circuit. Another issue we faced was the clogging of the ^{4}He circuit at the exit of the cryostat. This happened randomly, made the liquid ^{4}He transfer impossible and caused the pressure of gaseous helium to rise inside the tank. After some leak test, we found several leaks in the circuit that we fixed and we also added a check valve at the exit of the cryostat to make sure that no impurities from the ^{4}He provided by the Low Temperature service of the university could enter in the cryostat circuit.

III.2.4 Temperature measurements and resonator characterization

a) Calibration of the data

To measure the effective temperature of the mechanical mode we send an optical beam on the other polarization of the cavity. We use a PDH detection scheme to have another phase sensitive measurement outside of the feedback loop. To ensure the absence of cross-talk between the two beams, one beam is frequency shifted using AOMs. The frequency

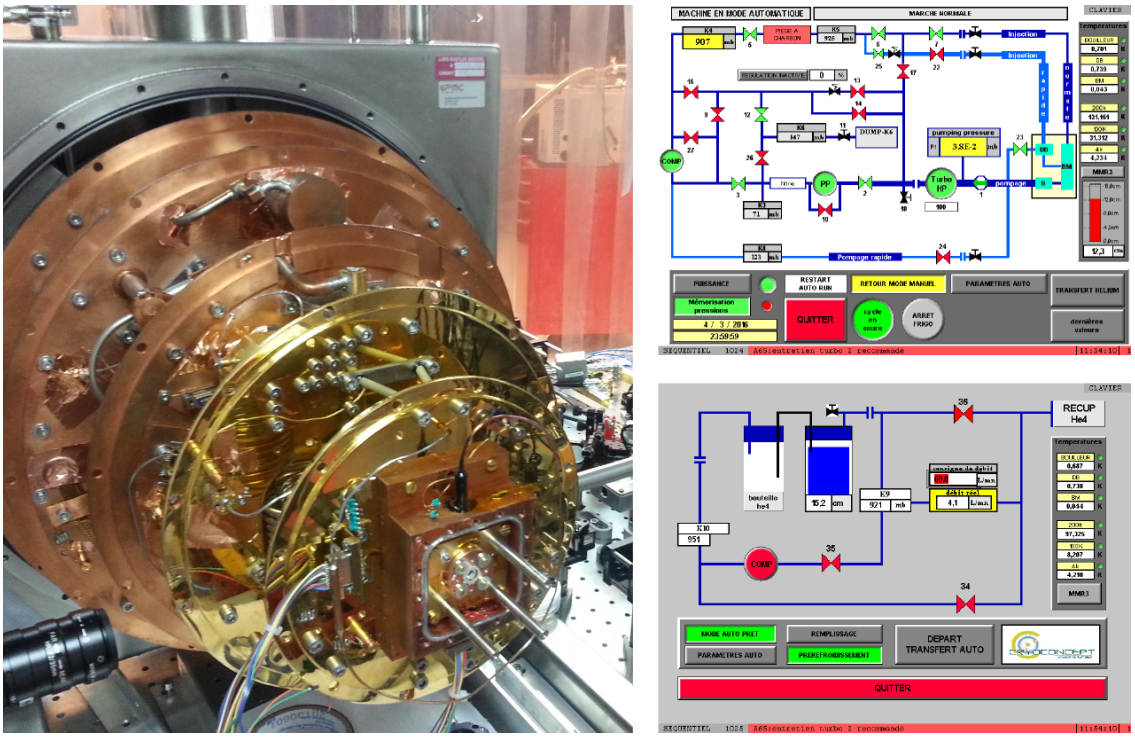

Fig. III.14 *Left: Photograph of the dilution refrigerator with all heat shields removed. Mounted on the square steel frame in the back, one can see the various plates on which the shields are fixed that are named after their nominal temperatures: 200 K, 100 K, 4 K, 1 K and 100 mK. At the center of the mixing chamber plate, a previous version of the Fabry-Perot cavity is mounted. Right: Screenshot of the touchscreen interface of the cryostat controller. The upper screen shows the controls of the 3He - 4He mixture circuit on which we can see the mixture tank (DUMP K4) and the trap (PIEGE A CHARBON), the lower screen the controls of the 4He circuit where a gauge tells us the tank of the cryostat is filled here with 15.2 cm of liquid helium. A full 20-l tank corresponds to a gauge at 15.7 cm while an empty one corresponds to a gauge at 2.3 cm.*

shift matches the birefringence of the cavity due to asymmetry of the input mirror along the two polarization axes. To calibrate the obtained spectrum we use a calibration tone generated by a phase modulator whose V_π has been calibrated beforehand. We can then convert the measured voltage of the spectrum analyzer in a phase variation. Given that we are using a linear Fabry-Perot cavity, we know that the amplitude $\delta\phi$ of a phase modulation at Ω_{mod} is equivalent to a displacement δx :

$$\delta x = \frac{L}{\nu_L}\Omega_m \delta\phi. \tag{III.4}$$

This relation depends on the cavity length that we need to measure precisely. To do so, we use a laser with a tunable wavelength and a λ-meter to monitor precisely its frequency, and record the value of the resonant frequencies of the cavity for four consecutive modes. We can then deduce the FSR value from the slope of the curve and thus the length of the

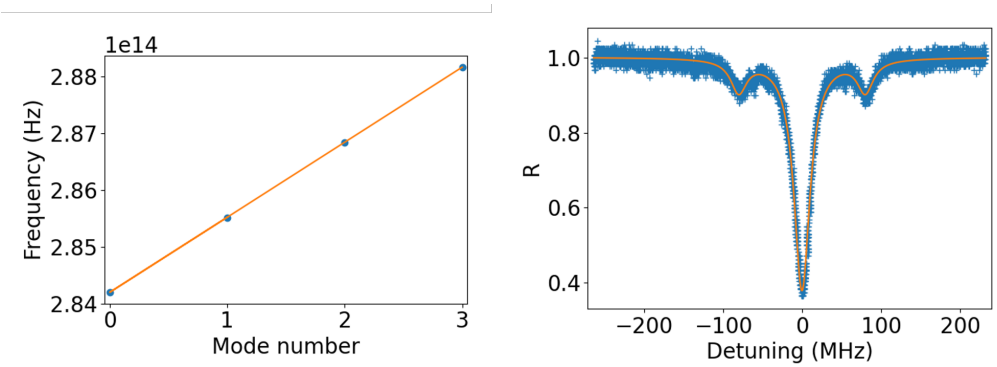

Fig. III.15 *Left : Cavity length calibration. The points mark the values of four consecutive resonance frequencies of the cavity. The slope yields an FSR of 1323 GHz corresponding to a cavity length of 113.4 µm. Right : Cavity bandwidth measurement. The cavity resonance is scanned using a PZT while applying a 80-MHz phase modulation to the optical field. The modulation creates sidebands at 80 MHz, allowing to calibrate the scan in frequency units and to measure the resonance peak bandwidth.*

cavity with a great precision (see Fig. III.15), which allows us to convert the spectrum in m^2/Hz. Using the fluctuation-dissipation Theorem we know that the area A under the thermal peak is proportional to the temperature of the mode:

$$\pi A \Gamma_{eff} = \frac{1}{2} k_B T. \tag{III.5}$$

b) The effective mass

The effective mass is calibrated at room temperature by doing the same process and assuming that the mechanical mode is at thermal equilibrium at room temperature. To minimize radiation pressure effect, we perform the measurement at ambient pressure where the quality factor is around 10^3, in such a way that the optical damping is negligible compared to the thermal damping (see Fig. III.16). We have performed such measurements for different values of the input optical power, ranging from 0.2 µW to 5 µW, to make sure there is no correlation between the measured value of the mass and the power injected into the cavity. The measured values are 112 ± 3 µg for the 1556N1 sample and 134 ± 3 µg for the 1556N2 sample. The effective mass of the mode can also be estimated using finite-element simulations, that yield a value of 110 µg, which matches the value measured experimentally even though the large difference between the effective mass value for the two different samples is a bit surprising.

c) The intrinsic quality factor

Even in the absence of feedback, as the cavity slightly shifts around the exact resonance, there is some cooling/amplification optomechanical effect: the quality factor and the tem-

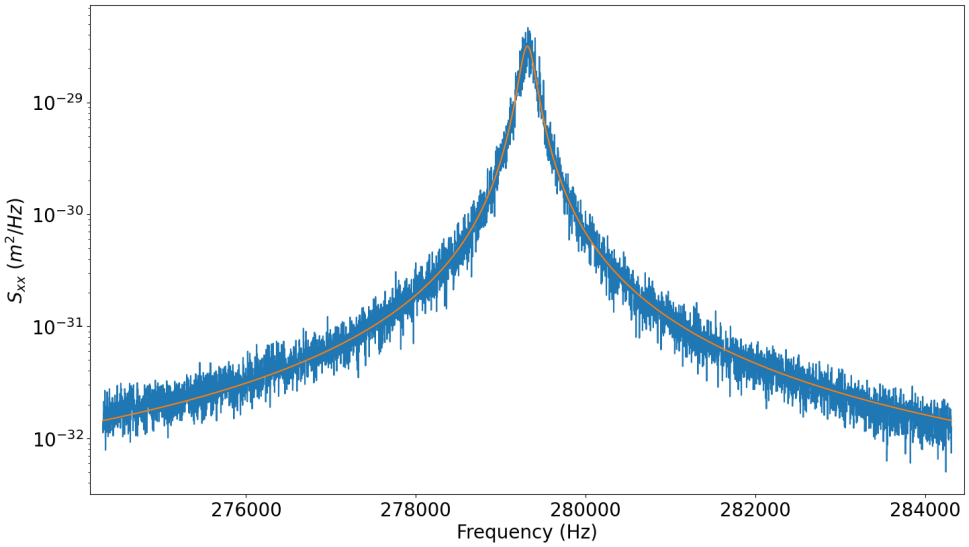

Fig. III.16 *Noise displacement spectrum of the mechanical mode at room temperature and ambient pressure with 1.9 µW of input optical power (blue curve). The Lorentzian fit (orange curve) corresponds to a mechanical quality factor* $Q = 1360$ *and yields and effective mass of 134±3 µg.*

perature measured by fitting the displacement spectrum are neither the intrinsic quality factor of the resonator nor the real temperature of the sample inside the cryostat.

To measure the intrinsic quality factor, we have to perform a measurement with the cavity unlocked: we sweep at low frequency the length of the cavity using the PZT and we send a small additional modulation (at the resonance frequency of the resonator) onto the PZT. Even though the PZT are behind the input mirror, this is sufficient to drive the resonance of the resonator. The reflection peak oscillates at high frequency, mimicking a larger peak for the optical resonance. By measuring the width of the peak as the drive is turned off, we perform a ring-down measurement of the mechanical mode. We know the curve is proportional to $e^{-\Gamma_m t/2} = e^{-\Omega_m t/(2Q)}$, so we can deduce a quality factor of 1.6 million here. We estimate the error by repeating the measurement, we obtain $\Delta Q = 30,000$. By comparing the intrinsic quality factors obtained with the one deduced from the spectra, we can measure how much the resonator is cooled and estimate the environment temperature, i.e. the temperature of the thermal bath inside the cryostat.

d) The feedback loop

The feedback is performed using the homodyne detection signal as an error signal. It is analogically filtered around the mechanical resonance using an LC filter then amplified and phase detuned before being sent to the fibered amplitude modulator (III.8). If the phase is not correctly tuned, we excite the resonator's motion instead of cooling it. To fine tune it, we add extra cable length l in our loop that phase shift the signal by $\Delta\phi = \frac{c}{2\pi\Omega_m}$. Finally,

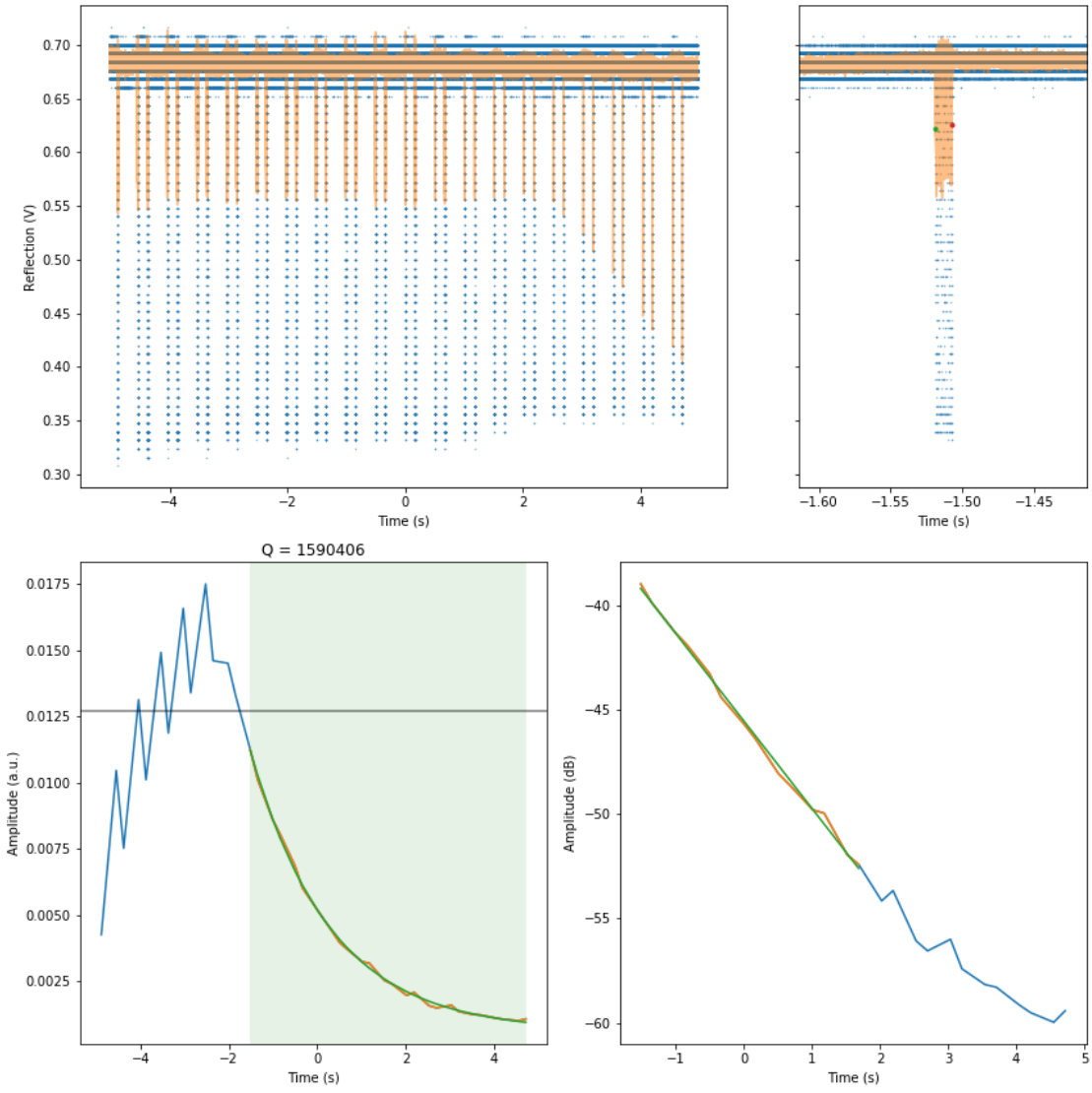

Fig. III.17 ***Ringdown measurement of the wheel resonator at dilution temperature.*** *Top left: Cavity optical resonance peaks (blue curve) with a drive of the oscillator. The width of the resonance peaks is directly related to the amplitude of motion of the resonator, which allows to perform a ringdown measurement. The orange curve is a down-sampled version of the blue curve. Top right: zoom on one of the resonance peaks with the green and red point corresponding to numerical evaluation of the width of the resonance peak. Bottom: width of the resonance peak as a function of time in linear (left) and logarithmic scales (right). The oscillator motion is driven for about 2 seconds before performing the measurement.*

to fine tune the feedback gain, we add attenuation blocks before the phase modulator. We find the optimal phase by looking at the thermal peak's height and frequency, the optimal value is reached when the height is at a minimum and when there is no shift in frequency when the feedback is applied. A shift in frequency, means a part of the force is real and act as an optical spring and we want to have it purely imaginary. Once the phase is optimised, we can start removing attenuation blocks. As we increase the feedback gain, we are getting more unstable so this part has to be done carefully.

e) Experimental feedback cooling results

We can now measure the resonator's effective temperature looking at the PDH detection but it can be measured as well with the homodyne detection. Calibration is performed in a similar manner as for the PDH scheme: we send a small modulation to the PZT of the cavity at a frequency close to the resonance frequency, creating a phase modulation. As the corresponding modulation peak can be monitored on both the PDH and the homodyne spectrum, the calibration of the PDH spectrum can be used to calibrate the phase modulation and the homodyne spectrum. This way we have two independent measurements, one being extracted from the error signal of our feedback loop and the other being the out-of-loop measurement.

We observe that for high feedback gains, the temperature of the environment, and the effective temperature that we deduce from the measurements, start decreasing faster than the temperature calculated with the out-of-loop measurement. This can be explained by the fact that feedback is actually driven by measurement noise. Using the method described in section II.6.2, we can take this effect into account and correct the value of temperature. The different temperatures we measure with the PDH and the homodyne detections are now in agreement. The results for the µ-pillar, which I have reanalyzed based on Rémi Metzdorff's measurements, are presented on Figure III.18: an effective temperature of 1.1 ± 0.1 mK was reached, which corresponds to a residual number of phonons of only 6.4 ± 0.8.

Similar results for the wheel resonator are presented on Figure III.19: a similar limit temperature of 1.16 ± 0.05 mK was reached, but because of the lower resonance frequency of the resonator, this only corresponds to 87 ± 3 phonons.

f) Computing the uncertainties

To compute the uncertainties on our fitting parameters, we cannot use the covariance method because our fitting function is non-linear. Instead we use the bootstrap method ([67]) where we generate artificial data-sets by doing a random sampling with replacements on the points of our initial data-set. Using this method, we generate 5000 new data-sets that will each contain a subset of the initial points with some of the points having an extra "weight" if they have been sampled more than once and some of the points having no weight at all if they haven't been sampled. Average over all the 5000 data-sets each points has the same weight. We then fit all the data-sets individually with the same Lorentzian function, which yields 5000 values for each fit parameter. On each data-set, depending on the weight of every point, the fit will be slightly different, giving an idea of how sensitive the fit is to each of the measurements. We can now do statistics on each of the values of the fit parameters and measure the standard deviation. We then define the

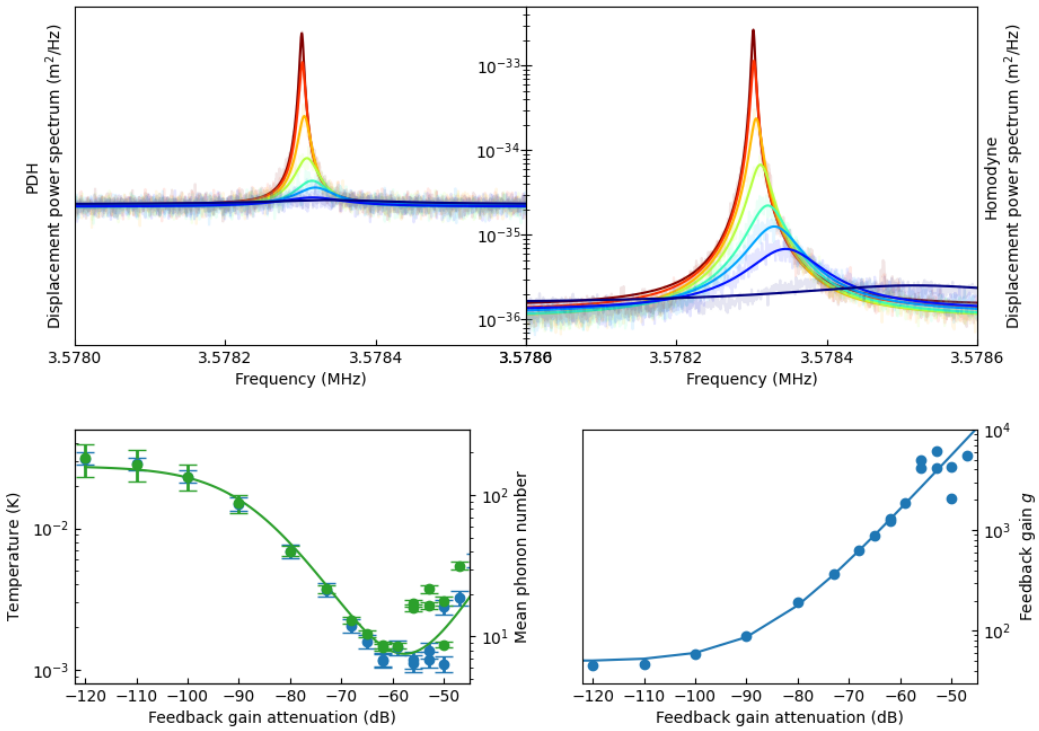

Fig. III.18 **Feedback cooling of the µ-pillar resonator**. *Top left: noise spectra from the PDH detection. Top right: same from the homodyne detection. Note that the sensitivity of the homodyne detection is much higher because it is quantum limited even for low signal intensity, thanks to the high intensity of the local oscillator beam. Bottom left: temperature curves extracted from the PDH (blue), which corresponds to the out-of-loop measurement. Curves extracted from the homodyne detection (green), taking into account the fact that it is an in-loop measurement. The uncertainties are computed using a bootstrap method on the fit parameters, detailed in section f). The solid line represents the theoretical temperature expected for the amount of feedback attenuation in the loop. Bottom right: feedback gain g extracted from the fitted curve as a function of the attenuation in the loop.*

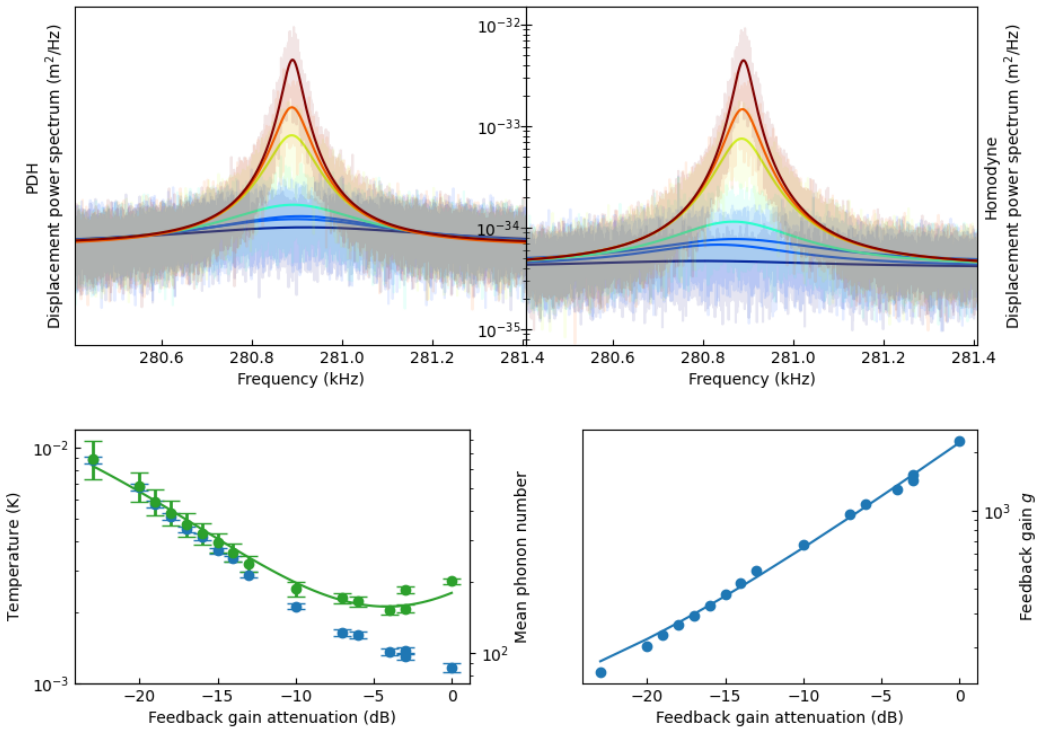

Fig. III.19 **Feedback cooling of the wheel resonator**. *Top left: noise spectra from the PDH detection. Top right: same from the homodyne detection. Note that the sensitivity of the homodyne detection is much higher because it is quantum limited even for low signal intensity, thanks to the high intensity of the local oscillator beam. Bottom left: temperature curves extracted from the PDH (blue), which corresponds to the out-of-loop measurement. Curves extracted from the homodyne detection (green), taking into account the fact that it is an in-loop measurement. The uncertainties are computed using a bootstrap method on the fit parameters, detailed in section f). The solid line represents the theoretical temperature expected for the amount of feedback attenuation in the loop. Bottom right: feedback gain g extracted from the fitted curve as a function of the attenuation in the loop.*

Relative error	$\frac{\Delta\Gamma_{eff}}{\Gamma_{eff}}$	$\frac{\Delta L_{cav}}{L_{cav}}$	$\frac{\Delta m_{eff}}{m_{eff}}$	$\frac{\Delta A}{A}$	$\frac{\Delta\omega_m}{\omega_m}$
Value	2 %	0.8 %	2 %	3 %	0.0005 %

Table III.3: Typical value of the relative errors estimated from the fit using a bootstrap method.

error as three times the value of this standard deviation in order to have 99.7 % chance that the fit parameter is in the error interval, assuming it distribution follows a normal law. The total error on the temperature measurements is then computed by taking the quadratic sum of all the error sources:

$$T_{eff} = \frac{\Gamma_{eff} A \pi m_{eff} \Omega_m^2}{k_B}, \tag{III.6}$$

where A is the calibrated amplitude of the thermal peak (in m^2/Hz). The total error is then:

$$\Delta T_{eff} = \sqrt{\left(\frac{\partial T_{eff}}{\partial \Gamma_{eff}}\Delta\Gamma_{eff}\right)^2 + \left(\frac{\partial T_{eff}}{\partial A}\Delta A\right)^2 + \left(\frac{\partial T_{eff}}{\partial m_{eff}}\Delta m_{eff}\right)^2 + \left(\frac{\partial T_{eff}}{\partial \omega_m}\Delta\omega_m\right)^2}. \tag{III.7}$$

Typical value of the relative errors can be found in Table III.3.

III.2.5 Current limitations

It is clear on Figures III.19 and III.18 that for large feedback gains, the thermal peak is fully suppressed and the environment temperature starts to increase, which means we are adding noise to the measurement. So it is no longer the cooling method that limits the experiment but rather the sensitivity floor of the detection. This floor gets lower with increasing power (see Fig. III.21)but for high optical power, we start to see an increase of the environment temperature due to optical absorption of the resonator (see Fig. III.21). It is also worth noting that the feedback loop becomes unstable for high feedback gain, causing the cavity to unlock. This is probably related to the excitation of low frequency modes of the resonators or the input mirror.

III.3 Conclusion

Feedback cooling has clearly allowed to reach temperatures substantially lower than the environment temperature and quite close to the QGS, but the experiment is now limited by other technical difficulties. We believe that reproducing the micro-pillar geometry in silicon using DRIE etching techniques would be the way to go, as the fabrication process is better mastered with silicon, as demonstrated by the repeatability of the wheel resonator characteristics. Silicon has roughly the same mechanical properties as quartz, so frequencies in the MHz range but with constant high quality factors should be recovered across different samples, as well as good thermalization.

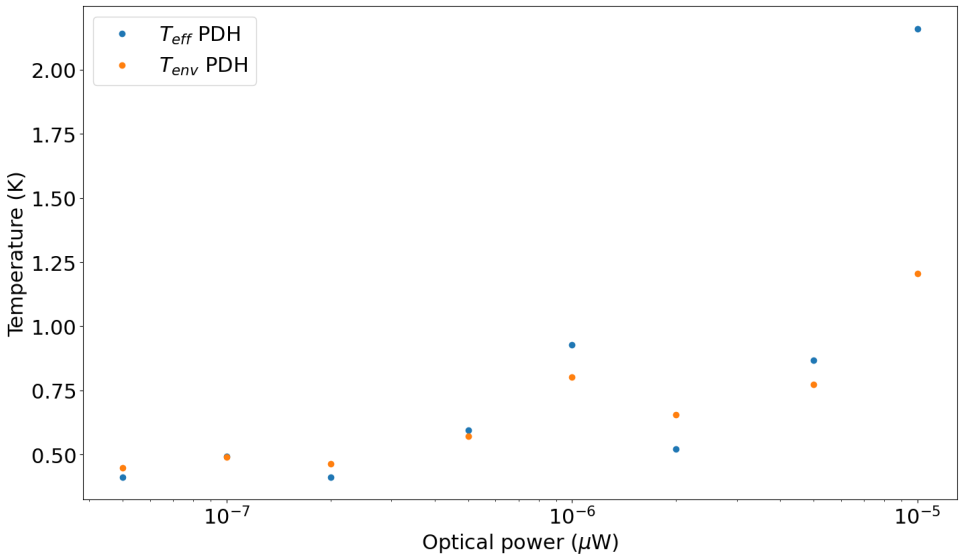

Fig. III.20 *Temperature from the mode without feedback as a function of optical power. For optical power above 1 µW, the temperature increases due to heat absorption of the sample and possibly low-frequency mode excitation.*

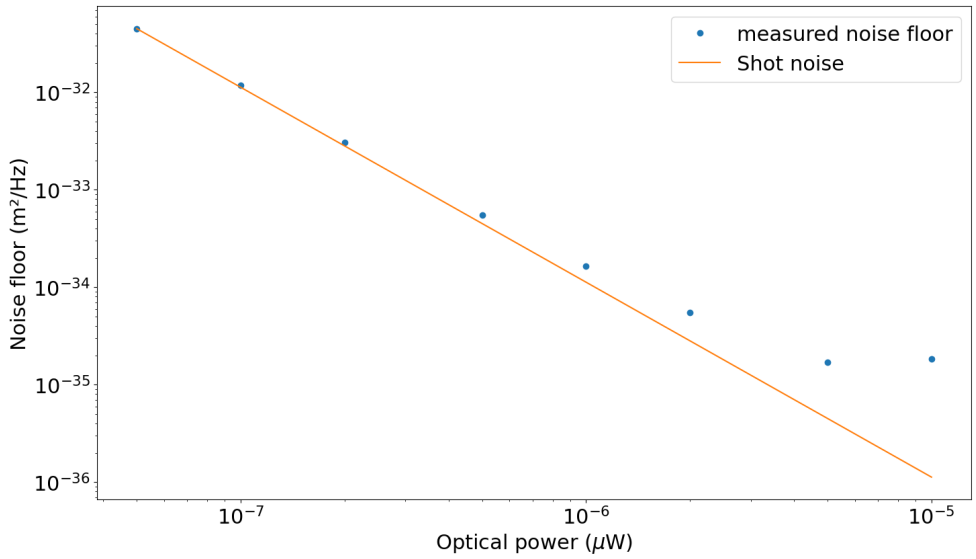

Fig. III.21 *Noise floor of the detection as a function of optical power. Above 1 µW, the detection sensitivity leaves the shot-noise limited regime (that scales as the inverse of the optical power) to reach a plateau. This is most certainly due to the thermal noise of the input mirror or a low-frequency mode of the resonator.*

Chapter IV

The squeezed light sources

In this chapter I will present in detail both the High Frequency (HF) squeezer developed and operated at LKB and briefly its Low-Frequency (LF) counterpart, that is operated at the CALVA 50-m long cavity at IJCLab in Orsay.

IV.1 General view of the HF squeezed light source

Our goal here was to design, assemble, characterize and operate a robust frequency-dependent bright squeezed light source at 1064 nm, to demonstrate reduction of the various types of quantum noise encountered in a continuous position measurement, and ultimately to demonstrate a position measurement on a mechanical oscillator with a resonant frequency in the MHz range, with a sensitivity better than the SQL over a broad frequency range.

The bright squeezed light source consists of:

- a CW infrared laser source (at ω_0), that is used to pump a Second Harmonic Generator
- a mode cleaner cavity in the infrared (MCIR), that is mainly used to suppress the classical noise of the laser
- a Second Harmonic Generator (SHG), that delivers a bright green field (at $2\omega_0$), made of a nonlinear optical crystal embedded in a resonant cavity
- an Optical Parametric Oscillator (OPO), also made of a nonlinear crystal embedded in a doubly-resonant cavity, which delivers a squeezed vacuum field at ω_0 when pumped below its threshold of oscillation
- a rotation cavity, that transforms the frequency-independent squeezed field delivered by the OPO into a frequency-dependent squeezed state.

The optical setup also includes a number of polarization optical components to split and recombine the different fields, various detectors both to monitor optical signals used to tune and lock the different cavities and ultimately to detect the produced squeezing, and modulators to create modulation sidebands also used to lock the different systems.

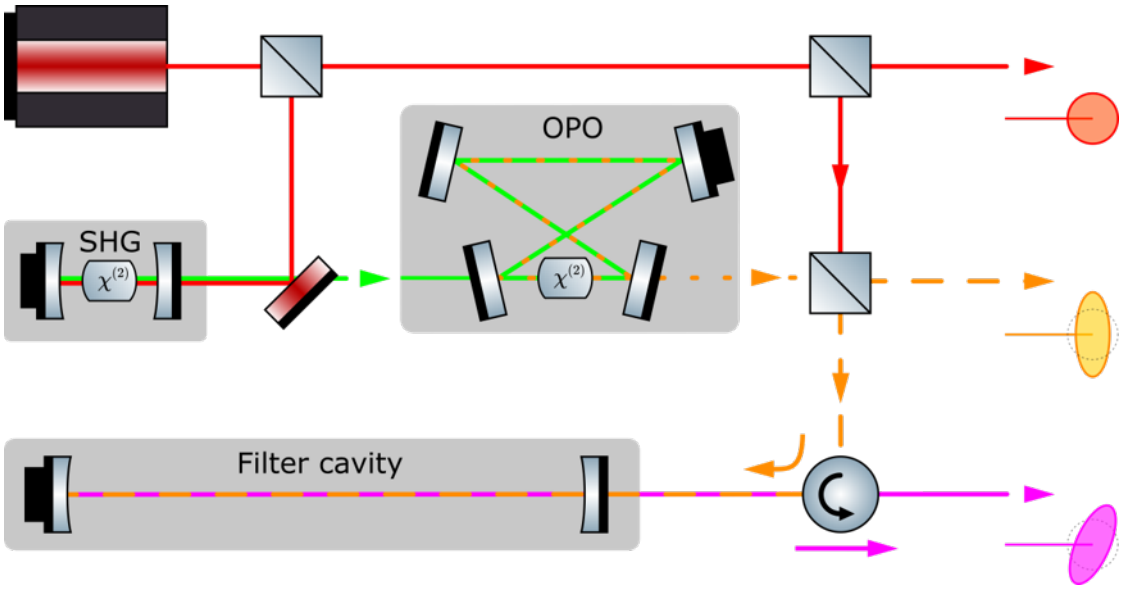

Fig. IV.1 *Schematic view of the main squeezer components. The squeezer is designed such that it can output either a bright coherent field (red), a bright frequency independent squeezed field (yellow) or a bright frequency independent squeezed field (pink).*

The setup is mounted on two optical breadboards so that it can easily be moved. At first, it was supposed to be mounted on top of the cooling experiment optical table to be injected directly in horizontal dilution cryostat. Eventually it was decided to bring it in the new experiment room next to the new dry dilution cryostat on a dedicated optical table. The squeezing would then be injected in a fiber and send to the fibered cavity with a membrane at the edge, as described in the next chapter. I will now proceed to a description of the different elements of the setup.

IV.2 The laser source

For stability reason, we use a Mephisto Nd:YAG laser from Coherent. This CW laser delivers up to 2 W of optical power and is shot-noise limited at 4 MHz and above (see Fig. IV.2). Around 1 MHz, the intensity noise spectrum of the free-running laser exhibits a broad peak related to the relaxation oscillation of the laser. This noise peak can be suppressed by a combination the noise eater system of the laser (with a feedback loop that directly acts upon the internal pump diode power) and a mode-cleaner cavity (see Fig. IV.3). The classical noise is then completely suppressed using an homodyne detection.

We use a New Focus resonant electro-optic phase modulator to generate a 20-MHz phase modulation, which is used to perform Pound-Drever-Hall (PDH) locking schemes for the SHG cavity and the MCIR cavity.

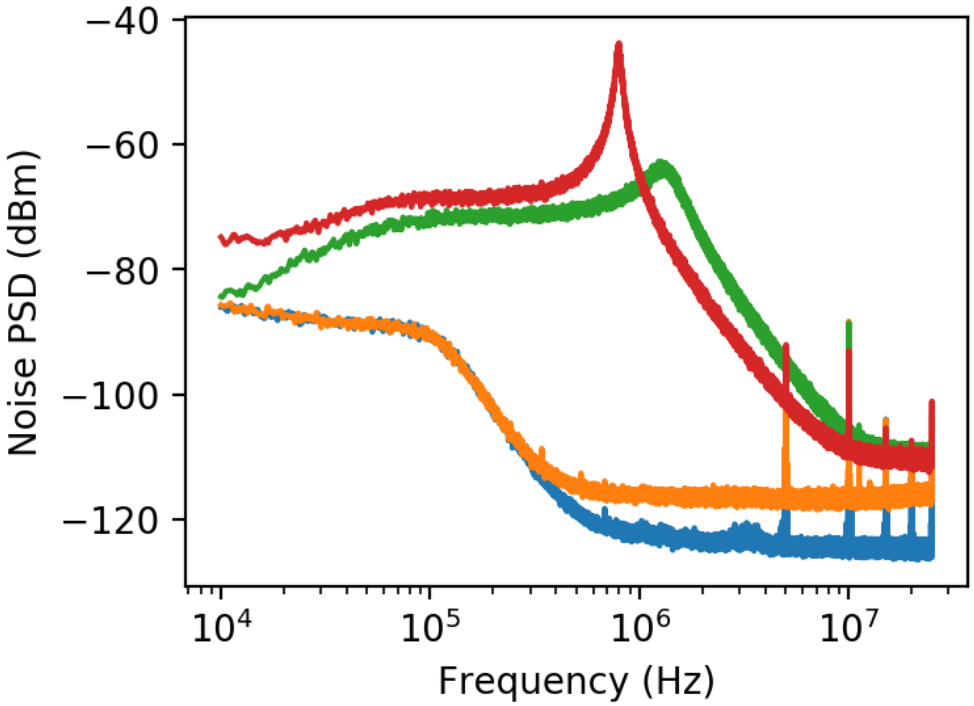

Fig. IV.2 *Amplitude noise of the laser measured by one of the detectors of the homodyne detection (no subtraction is performed). The green curve shows the amplitude noise for a 5 mW beam with the noise eater on and the red curve with the noise eater off. the orange curve is the dark noise from the photodetector and the blue curve is the noise floor from the spectrum analyzer.*

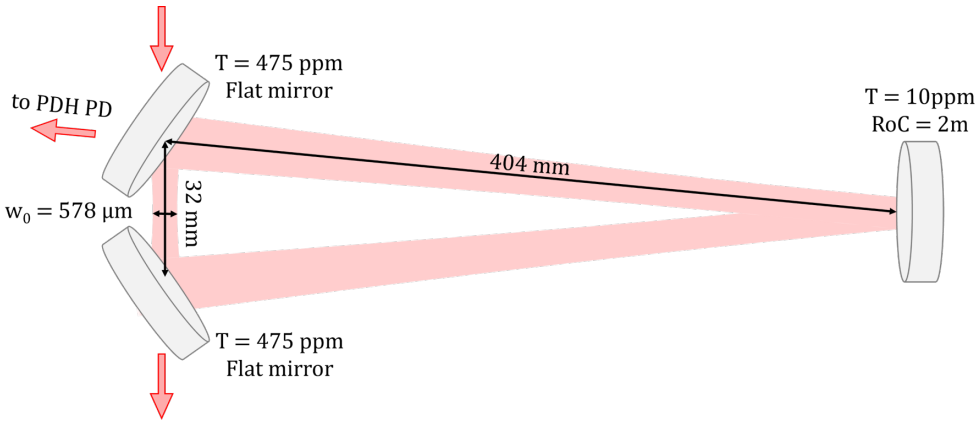

Fig. IV.3 *Schematic view of the triangular mode cleaner cavity.*

Fig. IV.4 *Picture of the MCIR cavity*

Cavity Parameter	Symbol	Value	Units
Round-trip Length	L	84	cm
Free Spectral Range	FSR	357	MHz
Optical Bandwidth	$\kappa/2\pi$	60	kHz
Finesse	$\mathcal{F}$	6000	
Reflectivity at resonance	R_0	0.47	
Curved Mirror's Radius of Curvature	RoC	-2	m
Input Mirror's Transmission	T_{in}	475	ppm
Output Mirror's Transmission	T_{out}	475	ppm
Excess Loss	P	718	ppm
Cavity waist	w_0	578	µm

Table IV.1: Parameters for the MCIR. The excess losses are computed using equation II.72. This, however, assumes a perfect mode matching of the laser with the MCIR cavity. The waist are computed using the formula in [68].

IV.3 The Mode Cleaner InfraRed cavity (MCIR)

This cavity has an isosceles triangular ring shape with a base of 3.2 cm composed of the two input and output mirrors. The peak mirror is a 2 m curved mirror with a transmission below 10 ppm. The input and output mirrors have a transmission of 475 ppm and are mounted with a 45° angle. This gives us a cavity with an optical finesse designed to be around 6,000 and a round-trip length of 84 cm, which corresponds to a linewidth of 60 kHz. As we saw in II.2.4, such an optical cavity acts as a low-pass filter with a cut-off frequency given by its linewidth: it suppresses classical noise of the laser up by 30 dB above 50 kHz as we can see on the figure IV.7.

The full parameters of the cavity (including additional optical losses) can be deduced by a whole set of measurements of its optical properties, as seen in section II.2.5: free spectral range, bandwidth, reflection at resonance... A sweep revealing the cavity resonances which is a classical measurement is shown on figure IV.5 and the table IV.1 summarizes its main characteristics.

Fig. IV.7 presents the intensity noise delivered by the full laser source, including the internal noise eater and the MCIR cavity. The four upper curves show the intensity noise of the beam that is available to the following stages of the squeezed light sources. We see that we have no classical noise left and we check that the noise floor scales linearly with

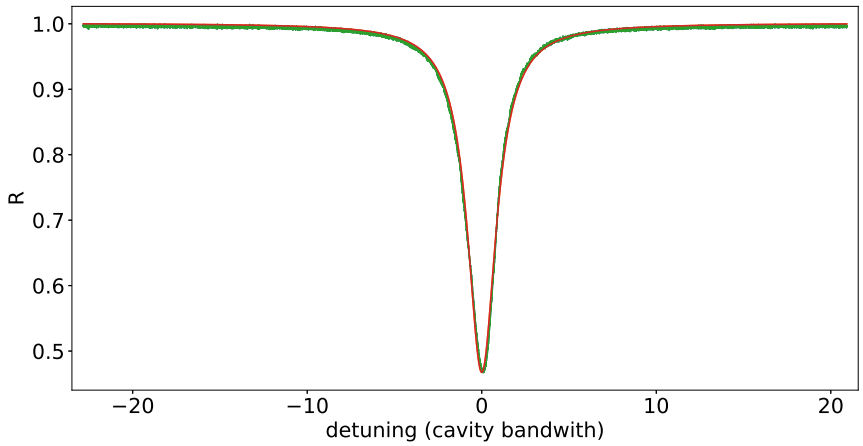

Fig. IV.5 *Reflection signal of the MCIR cavity obtained upon scanning the length of the cavity using the piezoelectric transducer glued to one mirror. We can extract R_0 using a Lorentzian fit of the data.*

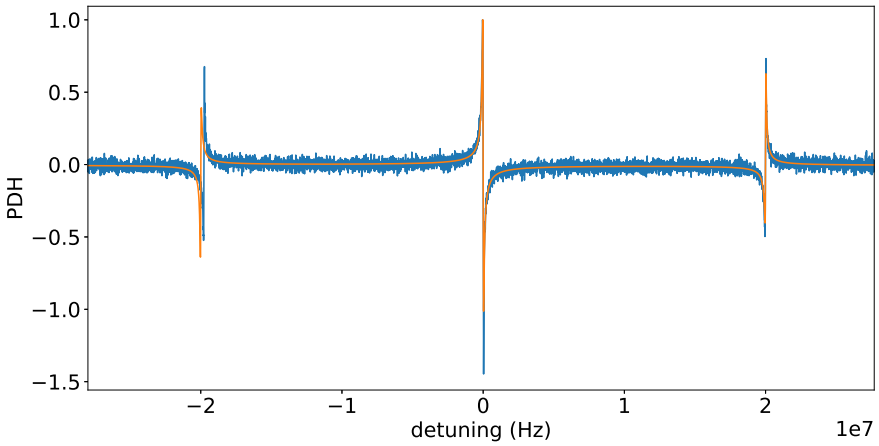

Fig. IV.6 *PDH signal of the MCIR for a 20-MHz modulation. The frequency calibration of the curve takes advantage of the knowledge of the modulation frequency. We extract then the optical bandwidth of the cavity. The FSR is computed from the value of length of the cavity (known to a very good accuracy). The finesse can then easily be deduced.*

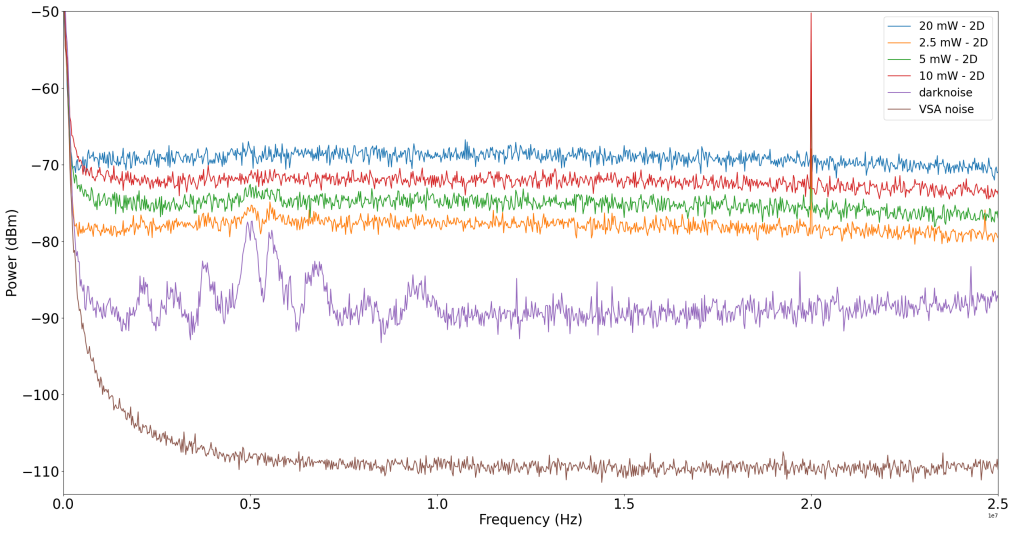

Fig. IV.7 *Shot noise of the laser source, measured with the homodyne detection (with a subtraction of the two photocurrents). The four upper curves show the amplitude shot noise with the noise eater turned on and after filtering of classical noise by the MCIR. The purple curves correspond to the dark noise from the photodetectors and the brown curve is the noise floor of the spectrum analyzer.*

the power sent on the detector (noise floor increased by 3 dB when doubling the optical power), which is characteristic of quantum shot noise.

IV.4 The Second Harmonic Generator (SHG)

Pumping our non-linear crystal to generate squeezing at 1064 nm requires a strong and stable pump laser source at 532 nm. Commercial solutions exist but as they are very expensive and lack flexibility, we opted for a homemade solution. The design was then copied for the two SHGs used at the Calva cavity (see Section IV.11).

IV.4.1 The Non-linear crystal

The core of the SHG is a non-linear crystal. We use a commercial Magnesium Oxyde doped Periodically poled Lithium Niobate (Mg0:PPLN) crystal from Covesion placed inside an oven regulated by a temperature controller. In a PPLN crystal, the crystal axis is regularly flipped to compensate for the fact that phase-matching between the different fields at ω_0 and $2\omega_0$ is not achieved. The crystal used in our experiment is actually composed of 5 different crystals with different phase-matching conditions for various wavelengths. We use the second one which is supposed to have a phase matching condition at 52°C (middle of the range of the temperature controller) for a 1064 nm pump. We will see that this temperature condition is altered by the crystal's pumping optical power.

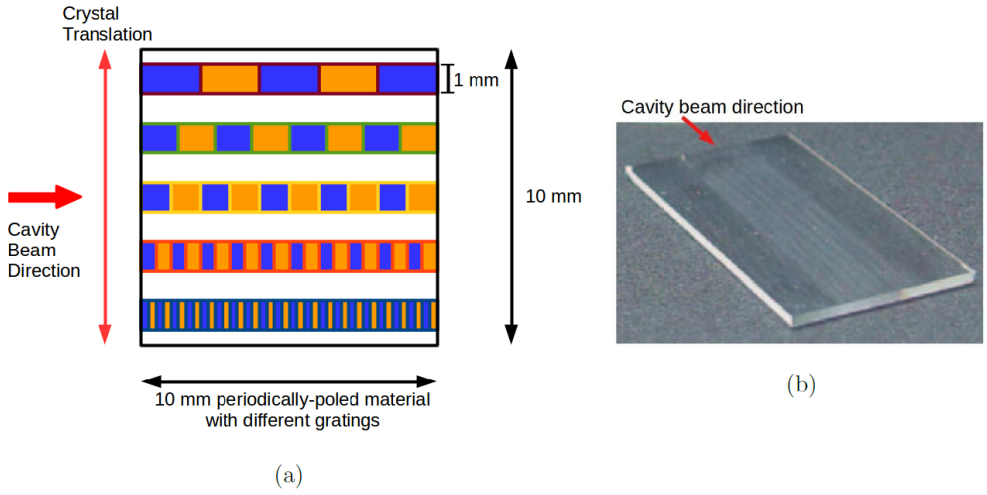

Fig. IV.8 *(a) The scheme of the PPLN crystal showing the 5 gratings that can be used as Second Harmonic Generators.(not to scale) (b) Picture of a PPLN crystals showing the gratings. Figure adapted from [69]*

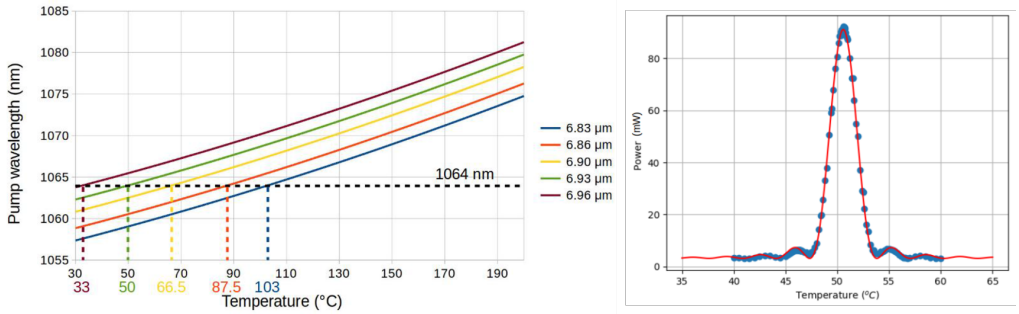

Fig. IV.9 *Left is the quasi-phase matching curves for each of the gratings. The pump wavelength is fixed by our main Nd:YAG laser at 1064 nm but we can choose between the three gratings depending on the temperature at which we prefer to operate. We chose 50°C which is not to close to room temperature but not too far either so the temperature stabilization is easier. Right is green power produced as a function of temperature using the 50°C grating, we recover the sinus cardinal curve of the quasi-phase matching condition. Figure adapted from [69]*

Cavity Parameter	Symbol	Value	Units
Round-trip Length	L	9	cm
Free Spectral Range	FSR	3.3	GHz
Optical Bandwidth	$\kappa/2\pi$	133	MHz
Finesse	$\mathcal{F}$	25	
Curved Mirrors' Radius of Curvature	RoC	-25	cm
Input Mirror's Reflectivity at 1064 nm	R_{in}^{1064}	0.9	
Input Mirror's Reflectivity at 532 nm	R_{in}^{532}	<0.01	
Output Mirror's Reflectivity at 1064 nm	R_{in}^{1064}	0.995	
Output Mirror's Reflectivity at 532 nm	R_{in}^{532}	>0.999	
Cavity waist at 532 nm	w_0^{532}	50	µm
Cavity waist at 1064 nm	w_0^{1064}	70	µm

Table IV.2: SHG's parameter

IV.4.2 The optical cavity

To enhance the non-linear effect we use an optical cavity of finesse 50 at 1064 nm. It's composed of two 1/2-inch concave mirrors with a radius of curvature of 25 mm. The front mirror has a reflectivity of 90 % at 1064 nm and below 1 % at 532 nm. The back mirror of the cavity has a reflectivity of 99.9 % at both wavelengths and is mounted on a piezoelectric transducer (PZT) used to lock the cavity at resonance, using a signal monitored by a photodiode in transmission. Due to the different properties of the coatings of the input mirror at 532 and 1064 nm, most of the green beam is reflected by the cavity and ready to be sent to the OPO.

For stability reasons, the two mirrors are mounted on a 60-mm Thorlabs cage system ensuring their solidarity. This mechanical arrangement leads to a very robust setup but still allows fairly easy alignments. We start by aligning the cavity without the crystal, maximizing the intensity peak in transmission while scanning the length of the cavity using the back piezoelectric. When we have only a TEM_{00} mode, we remove the rod of the cage system and place the crystal inside the cavity with the temperature set by the controller around 52°C. Flashes of green light indicate that the crystal approaches a good position and we tight it in place when the perfect position is reached. We then optimize the signal using the two input mirrors of the cavity and the focusing lens right in front of it. We can then lock the cavity and optimize the temperature of the crystal to get the maximum amount of green output power. The intracavity power is quite high so the ideal temperature will vary depending on the pump power sent inside the cavity. At the end we get a 36-% green power conversion efficiency and up to 300 mW of green light. With a greatly optimised setup, Zhou et al. have measured 52 % of conversion efficiency and a maximal output power of 1.6 W [70].

IV.5 The Optical Parametric oscillator (OPO)

This is the main and most crucial part of the squeezer as it is where the squeezing is created. The design was made by Sheon Chua and is an adaptation of the design he did during his PhD thesis at Australian National University [41]. The goal was to have

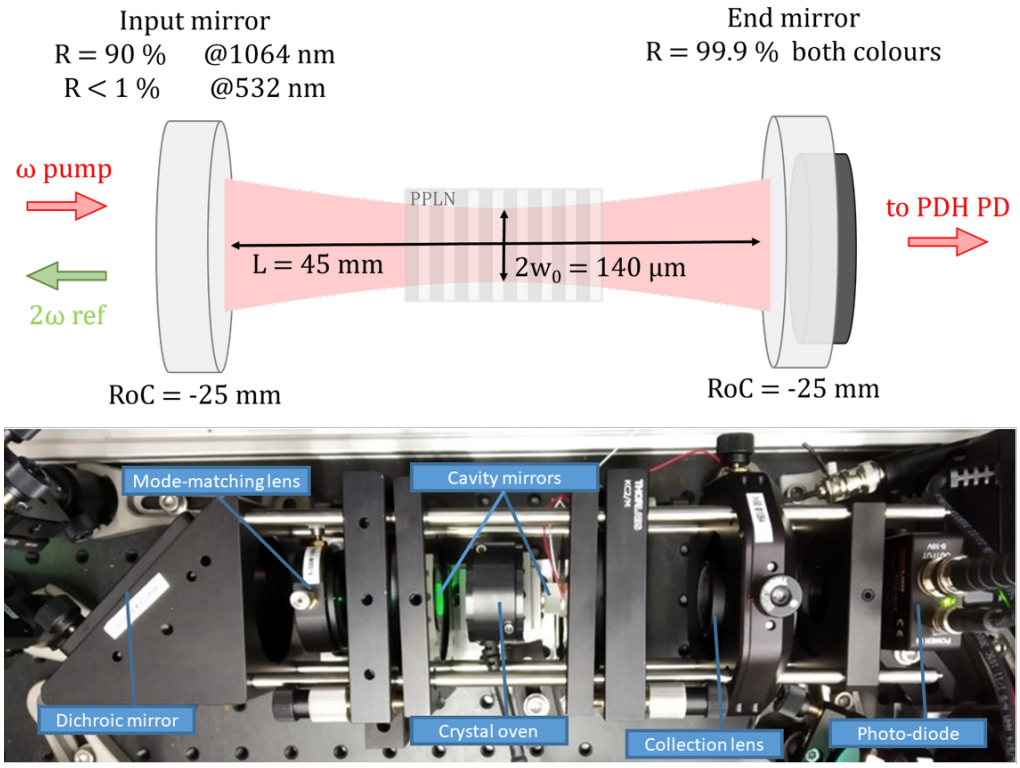

Fig. IV.10 *Schematics of the SHG confocal cavity geometry and top view of the SHG cavity*

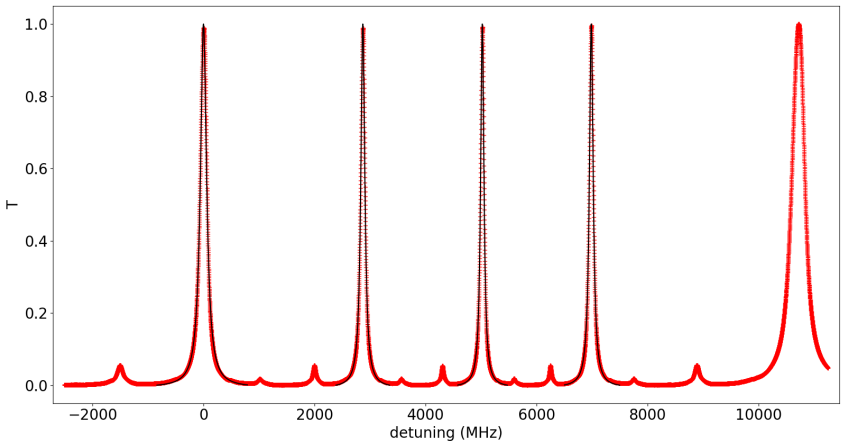

Fig. IV.11 *Transmission signal of the SHG as we scan the length of the cavity using the PZT. We can extract the finesse by measuring the ratio between the width of the resonance peaks and the distance between them.*

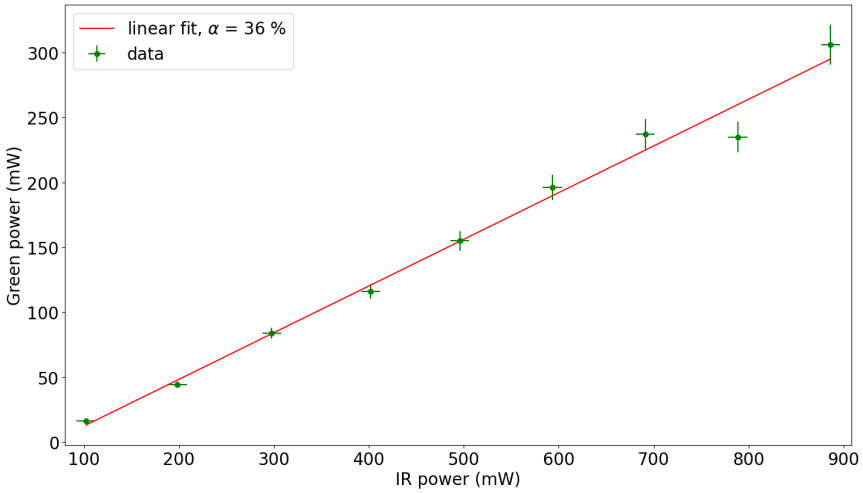

Fig. IV.12 ***Green power conversion as a function of the IR pump power.*** *As a comparison, the Prometheus laser from Coherent can only provide a maximum output of 100 mW of green power.*

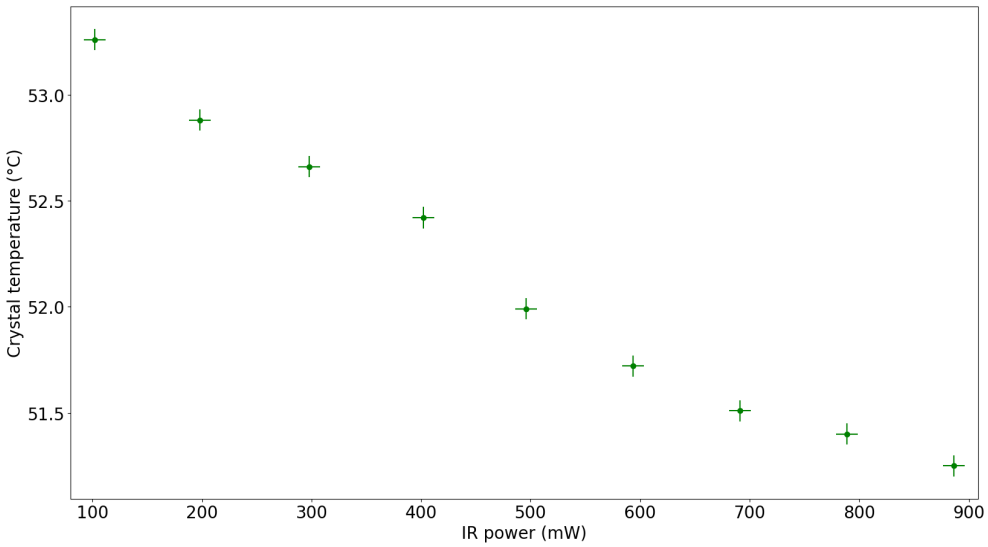

Fig. IV.13 ***Optimal set-point temperature of the temperature controller for non-linear gain as a function of the IR pump power.*** *We can see that as we increase the amount of IR power inside the cavity, we heat up the crystal and we need to compensate with the temperature controller. We observed that those values tend to also depend on the temperature of the room.*

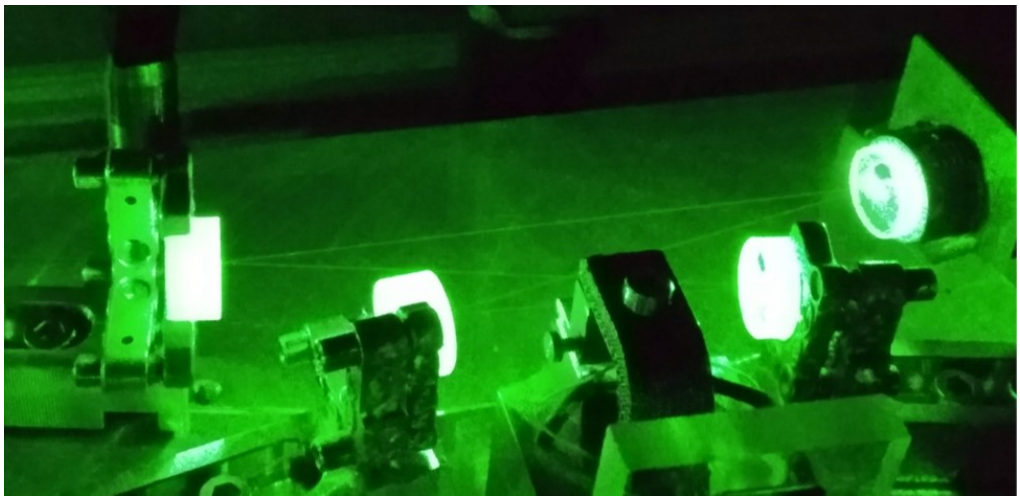

Fig. IV.14 *The OPO butterfly cavity at resonance with 200 mW of intra-cavity power*

a similar design as the OPO at Calva for the Low-Frequency squeezing experiments, so some of the characteristics were adjusted here to avoid noise at low frequency even though it should not affect us in the MHz range where we plan to use the squeezing produced.

IV.5.1 The Non-linear crystal

The crystal is here a Periodically-Poled Potassium Titanyl Phosphate (PPKTP). The crystals are bought from Raicol, a company specialised in crystal growth. They have been polished by Photon Laser Optik with a micro-roughness $< 0{,}15$ rms and finally coated by Laser Optik Gmbh with an anti-reflective set of layers giving R<0.5 % at 532 nm and R<0.1% at 1064 nm. The crystals are created with an extra buffer of material, with no non-linear property but the same index as the rest of the crystal, at the edge (Fig.IV.15). The crystal is dispersive so the effective path for the pump (532 nm) and the seed (1064 nm) is not guaranteed to be the same. But to enhance the non-linear effect we need to ensure that the two wavelengths are both resonant inside the cavity so the buffer is carved into a wedge. By laterally translating the crystal, we can adjust the length of the crystal where the beams propagate and tune the cavity to achieve co-resonance at 532 and 1064 nm. This adjustment is sensitive and tricky because it also relies on the temperature of the crystal which is tuned to achieve the best phase-matching condition possible. As a consequence, these two parameters (crystal temperature and position) need to be tuned together.

IV.5.2 The bow-tie cavity

The major feature of a bow-tie cavity in our case is to gain spatial separation of the inputs and outputs of the cavity which is very useful, particularly for a doubly resonant cavity. The other advantage is the fact that the resonant wave is travelling and not stationary, which prevents coupling of back-scattered light into the cavity. This effect is particularly problematic at low frequency so it's more of an issue for squeezing in the Hz to kHz range,

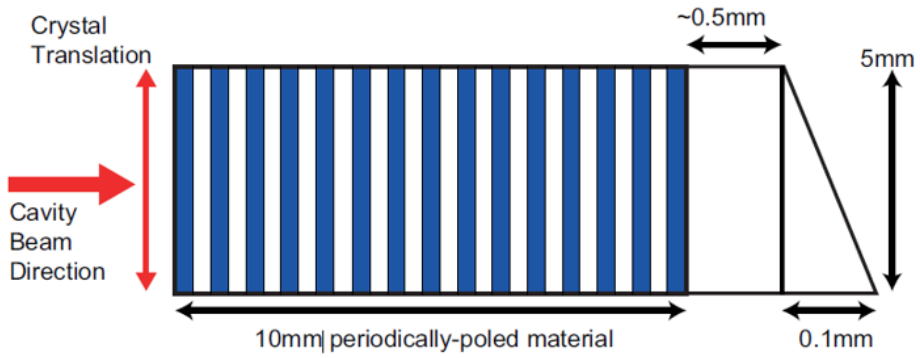

Fig. IV.15 *Illustration of the OPO nonlinear crystal of PPKTP, with an angle-polished wedge in a non-poled KTP material. Figure from [41].*

but with the constrain of having similar experiments at LKB and Calva, we have chosen to keep the same OPO design on the two squeezers. A detailed description of the cavity design and back-scattering light effects is given in [41].

IV.5.3 OPO threshold

To test that the OPO is functioning well and in good condition to deliver squeezing, we first check that we see amplification of the seed beam at 1064 nm. This can be first observed by sending around 50 mW of 532 nm pump power inside the OPO and sweeping the cavity length. We then send the seed beam inside the OPO via the fiber coupler. By monitoring the cavity resonances simultaneously, we can tune the correspondence of the cavity: when the two optical resonances (at 532 and 1064 nm) overlap, we see that the

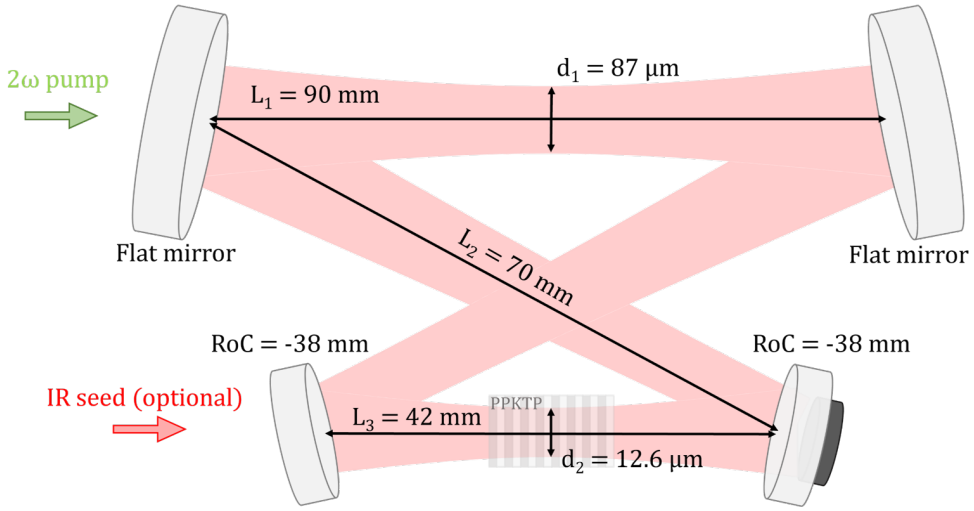

Fig. IV.16 *Schematics of the OPO bow-tie cavity geometry*

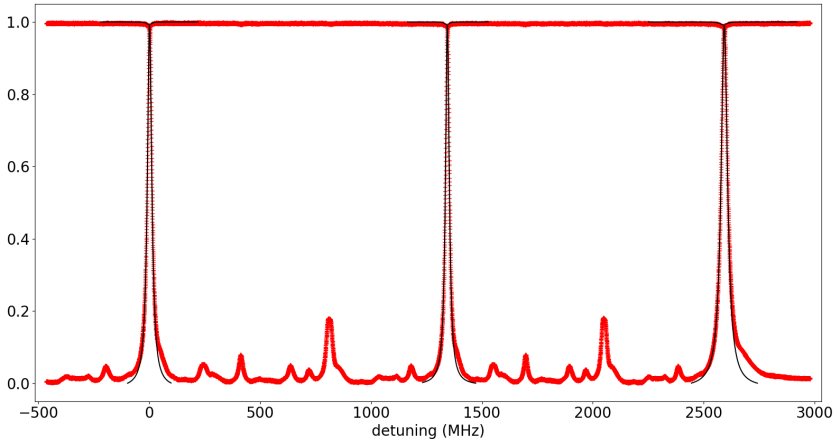

Fig. IV.17 *Reflection and transmission signal of the OPO cavity at 1064 nm. The transmission signal has been re-normalized neglecting internal losses ($T + R = 1$). Lorentzian fit are in black. The slight irregularity in the peak's spacing is due to the piezo non-linearity. Here we see that despite our best effort the mode matching is not perfect and we can see some higher order modes.*

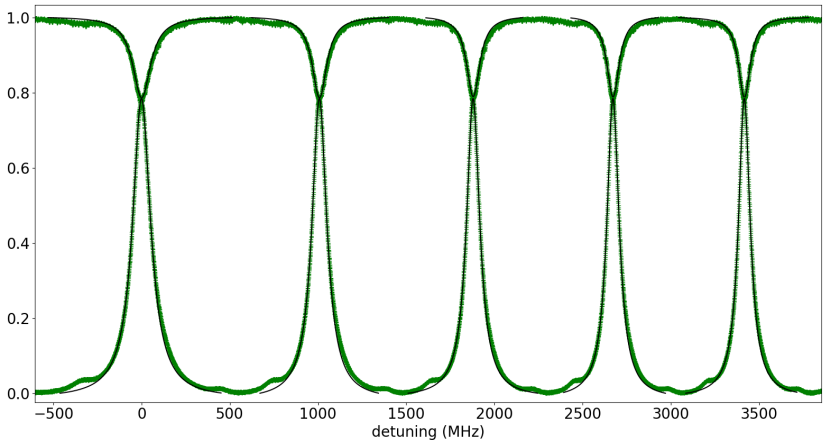

Fig. IV.18 *Reflection and transmission signal of the OPO cavity at 532 nm. The transmission signal has been re-normalized neglecting internal losses ($T + R = 1$)*

.

Cavity Parameter	Symbol	Value	Units
Round-trip Length	L	27.2	cm
Free Spectral range	FSR	1.1	GHz
Curved Mirrors'Radius of Curvature	RoC	-38	mm
Input Mirror's Reflectivity at 1064 nm	R_{in}^{1064}	0.84 (specs) vs 0.88 (meas)	
Input Mirror's Reflectivity at 532 nm	R_{in}^{532}	0.72 (specs) vs 0.54 (meas)	
Output Mirror's Reflectivity at 1064 nm	R_{out}^{1064}	>0.9999	
Output Mirror's Reflectivity at 532 nm	R_{out}^{532}	>0.9999	
Excess Loss at 1064 nm	P^{1064}	3	ppm
Excess Loss at 532 nm	P^{532}	2.75	%
Finesse at 1064 nm	F^{1064}	50	
Finesse at 532 nm	F^{532}	9	
Bandwidth at 1064 nm	$\kappa^{1064}/2\pi$	22.4	MHz
Bandwidth at 532 nm	$\kappa^{532}/2\pi$	123	MHz
Reflectivity at resonance at 1064 nm	R_0^{1064}	0.99	
Reflectivity at resonance at 532 nm	R_0^{532}	0.785	
Escape efficiency	η_{esc}	94	%
Waist at 1064 nm inside the crystal	w_0^{1064}	13	µm
Waist at 532 nm inside the crystal	w_0^{532}	9	µm
Waist at 1064 nm outside the crystal	w_0^{1064}	87	µm
Waist at 532 nm outside the crystal	w_0^{532}	62	µm

Table IV.3: OPO's parameter. The input mirror's reflectivity value measured (meas) differ significantly from the specified value (specs). We are not entirely sure how to explain this discrepancy but the changes don't affect the squeezing so much as the finesse at 532 nm is not very important its rather the escape efficiency that matters and this is still sufficiently high. The finesse in the infra-red being higher than 36 which was specified is surprising but not a problem in itself. The waists are computed using calculations specific to the bow-tie geometries in [71].

seed resonance amplitude fluctuates as a function of the phase of the pump. In order to see this phenomenon, the temperature of the crystal must be tuned at the phase-matching value and the pump and the seed need to be vertically polarized. We then lock the OPO at the co-resonance using a Redpitaya (see below). Once the OPO is locked, we scan the phase of the pump using the piezo (Fig.IV.22) and we see on the infrared fringes where we switch from amplification to de-amplification of the seed beam.

IV.6 The Rotation Cavity (RC)

The rotation cavity consists of a plano concave linear cavity of length X. It's built in a tube of Invar to ensure long-term thermal stability. The concave mirror has a radius of curvature of 2 m and is mounted on a piezo to ensure its length control. It's bandwidth needs to be tuned depending on the SQL frequency of our measurement. For now on it's designed to loose as little squeezing as possible, so to have a minimal transmission.

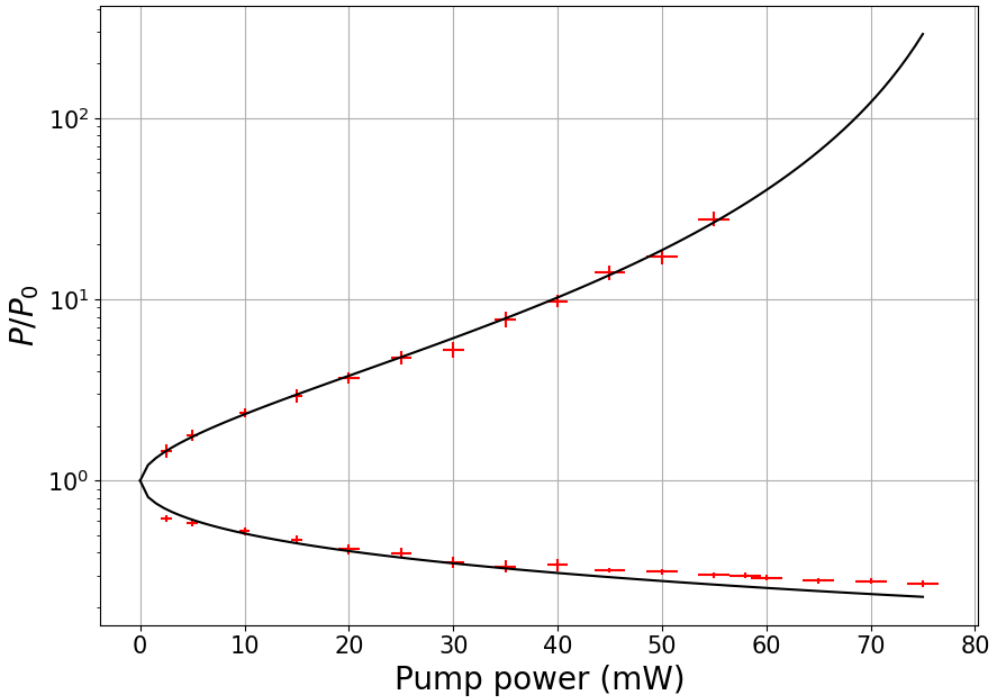

Fig. IV.19 *OPO's infrared amplification (g^+ and de amplification g^- gain as a function of pump power P_p.We find a threshold of 85 mW for the amplification curve and a threshold of 63 mW for the de-amplification curve but this could be caused by a systematic error on the infrared power measurement (we are measuring very low power).*

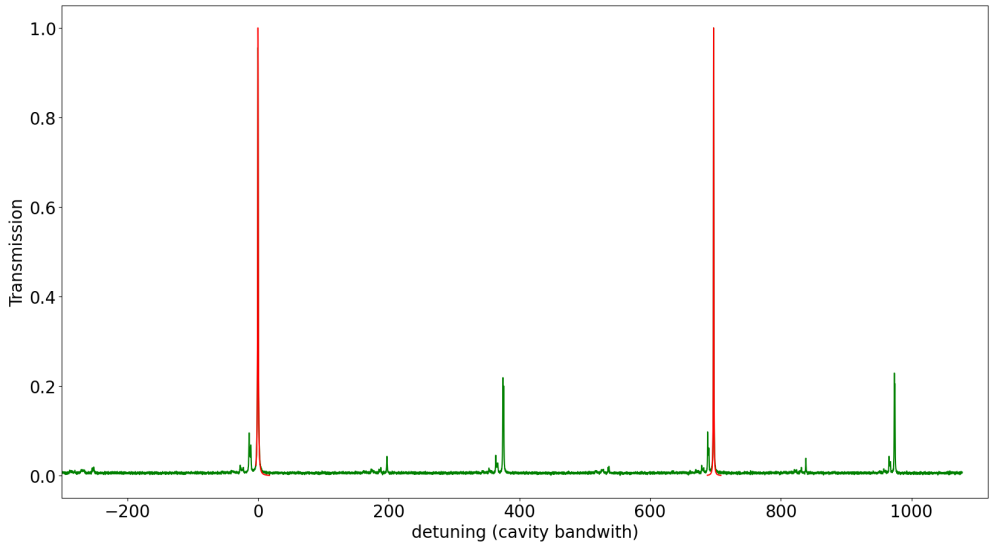

Fig. IV.20 *Transmission signal of the RC cavity. The transmission signal has been re-normalized.*

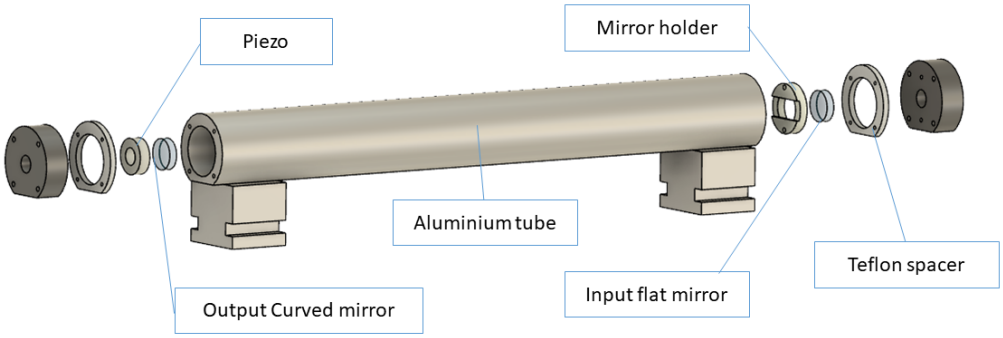

Fig. IV.21 *3D exploded view of the rotation cavity. The input mirror can easily be switched to change it's bandwidth and make sure it matches the SQL frequency of our optomechanical system.*

Cavity Parameter	Symbol	Value	Units
Round-trip Length	L	2× 49	cm
Free Spectral range	FSR	306	MHz
Curved Mirrors' Radius of Curvature	RoC	-2	m
Input Mirror's Reflectivity	R_{in}	99,993	%
Output Mirror's transmission	T_{out}	<1	ppm
Finesse	F	870	
Bandwidth	$\kappa/2\pi$	352	kHz
Cavity waist	w_0	540	µm

Table IV.4: RC's parameter

IV.7 Cavity locking

The locks are all done using Redpitayas which are FPGA's programmable boards with two 14 bits analog inputs and outputs clocked at 125 MHz. We then use a home-made Python library Pyrpl, to control those boards. A complete description of Pyrpl's architecture and functioning can be found in [72].

For the SHG and the MCIR we use Pound-Drever-Hall (PDH) locking schemes : The Redpitaya generates a phase modulation signal that is added to the laser thanks to a New Focus IR 20 MHz resonant phase modulator. We then demodulate the reflection signal from the MCIR and the transmission signal from the SHG to generate our two PDH error signals. The two locks are performed on the same Redpitaya board so we use a bias-tee on one of the outputs using the high frequency part to generate the 20 MHz modulation and the low frequency part to apply feedback on the SHG's cavity piezo. The Redpitaya's output signals are then amplified using High-Voltage amplifiers that were custom-made by the LKB's electronics workshop. To filter this High-voltage signal, we add a resistor right before the piezo so that with its internal capacity we get a low pass RC-filter with a cut-off frequency in the 100 Hz range (The piezo capacity being in the 100 nF range, we typically use a resistor in the 10 kOhm range)

The OPO is locked with another PDH schemes. The phase modulator is also a New focus 532 nm 20 MHz resonant phase modulator. It's driven at 21 MHz to avoid any

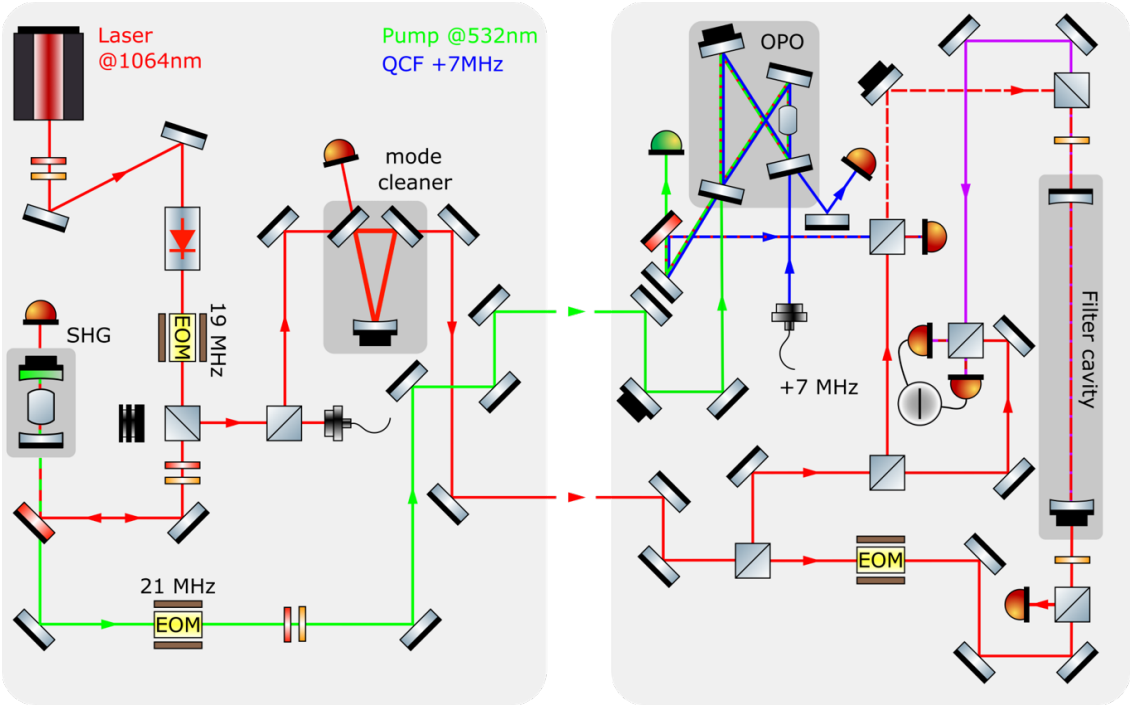

Fig. IV.22 ***Simplified optical setup with all the principal elements.*** *EOM stands for Electro-Optic Modulator. Those are used to generate phase modulation for the PDH locks mentioned in section IV.7. The detuned coherent control field is represented in blue, the vacuum squeezed field is represented in dashed red and frequency dependent squeezing is represented in purple.*

cross talk with some residual modulation. Because of the bow tie geometry we can access both the reflected and the transmitted signal of the OPO at 532 nm but we found that the transmitted signal gave a much cleaner PDH error signal.

The rotation cavity is for now locked on the side of a fringe using the transmitted signal. On the long term, depending on the detuning we would need to achieve to ensure proper rotation of the squeezing ellipse we might want to lock it on higher order modes which would be easily doable using a Redpitaya.

IV.8 First squeezing measurement

Once we are sure that the OPO is functioning correctly, we can try to see vacuum squeezing. For this we just lock the OPO at coresonance and mix the vacuum squeezing at the output with the LO onto the homodyne detection while scanning the phase of the pump. When looking at the high-frequency channel with a zero Hz span on the spectrum analyzer, we obtain the arches on figure IV.24.

As we scan the phase of the pump, we are rotating the ellipse of vacuum squeezing and so as we are recombining it with the LO, we are seeing amplitude noise squeezing and anti-squeezing. In order to maximize the squeezing level, we need to make sure that the LO and squeezing beams are mode-matched as best as possible and align on the same

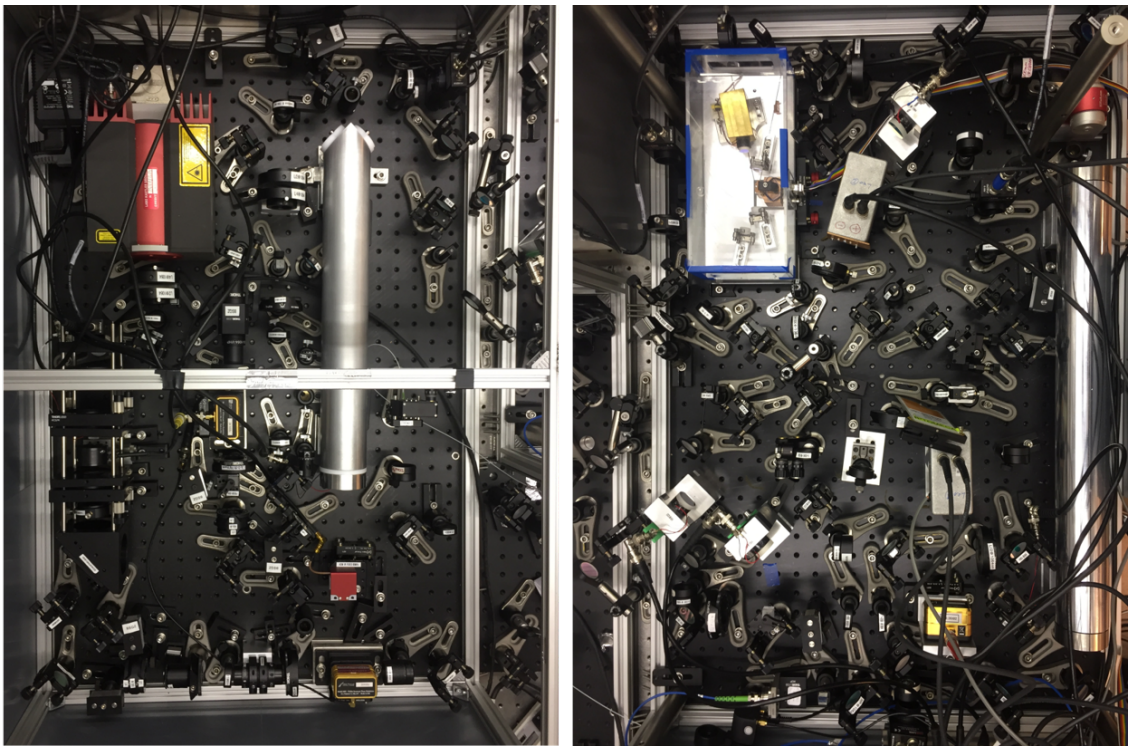

Fig. IV.23 ***Picture of the optical table*** *The setup is mounted on two breadboards so that it can easily be moved.*

polarization. To perform this optimization we use the seed beam which has the same polarization and mode shape as the squeezing. When alignment and polarization are optimized, we block the seed beam and measure the squeezing.

IV.9 Controlling the angle of squeezing

To perform an actual measurement with our squeezing we need to have bright squeezing and to be able to control the angle of the ellipse of squeezing which we were scanning in the previous measurement. To do this we use a coherent control scheme developed by [73] and adapted in our case for bright squeezing. This method allows us to control the angle of the squeezing ellipse without destroying the non-coherent state.

IV.9.1 Coherent control locking

a) Generating an auxiliary detuned field

To do this, we first need an auxiliary beam, i.e. an optical field detuned by a fixed and controlled frequency Ω from our main laser frequency ω_0. We first tried using an Acousto-Optical Modulator (AOM) resonating at 40 MHz. Unfortunately, the shift in frequency was too big compared to the OPO bandwidth and the shifted beam didn't interact with the OPO sufficiently to see any creation of the second side-band at $-\Omega$. So we did a second trial with a 20 MHz resonant AOM but when trying to demodulate the signal at

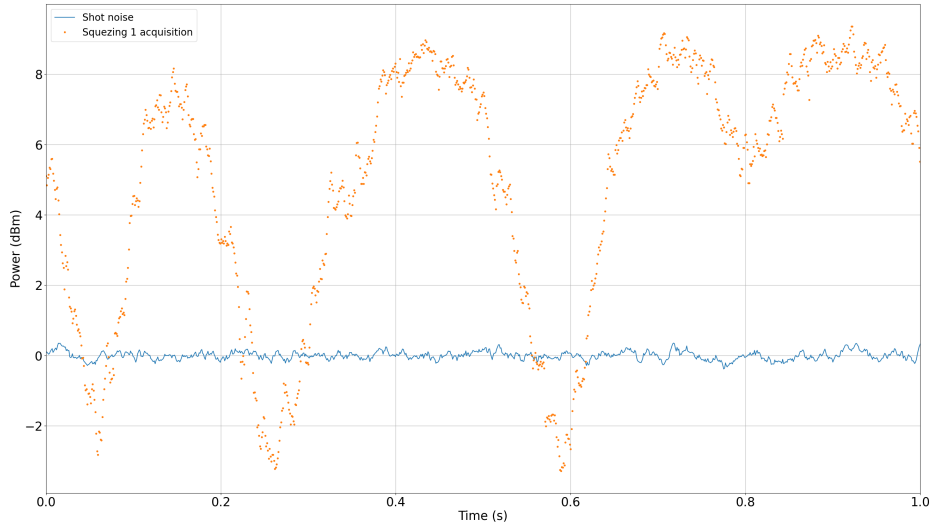

Fig. IV.24 *Here we scan the phase of the pump and we measure the laser phase noise by looking at the high frequency output of the homodyne detector at 500 kHz and 0 span on the spectrum analyzer. We see that we have 8 dB of antisqueezing and 3 dB of squeezing.*

2Ω we were actually seeing second order interaction from the main field with AOM that we couldn't filter out and that prevented us from seeing the actual error signal. So we decided to use a second laser that we would lock with Phase Lock Loop (PLL) to the MAIN laser (Fig. IV.25). It is a more expensive option but it is more flexible (you can choose Ω as you like and you have plenty of spare power compared to an AOM which is not very efficient) and this solution was also going to be implemented on the low frequency squeezer at Calva so it was a good way to test it. So we bought a Mephisto S laser from coherent which is exactly the same laser as the MAIN laser but with 200 mW of power.

b) The Phase Lock Loop

The AUX laser is directly injected inside a fiber and a small pick-up is sent to a mixer. On the other part, we send a small pick-up of the fibered seed beam and we send the two mixed beam on a photodiode (PLL PD). On this photodiode we get the beatnote signal of the two beams. However, we need to extract a suitable error signal for the lock (Fig. IV.26).

c) The error signal

We need this signal to be both precise (give a good estimation of the phase difference when the lasers are at the same frequency) and robust (give a coherent error signal even when the beating frequency between the two lasers is completely off). The first thing we did was to send the beating signal to the RedPitaya and use the IQ module from

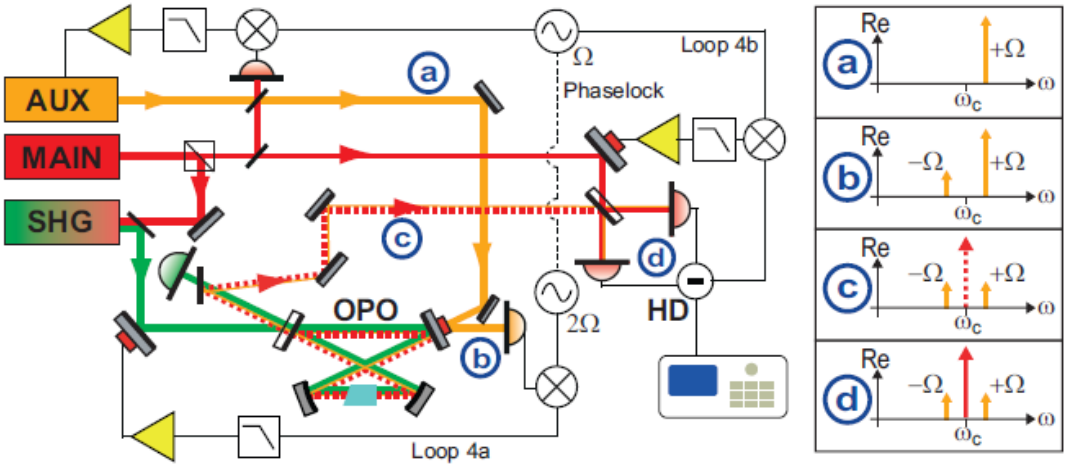

Fig. IV.25 ***Coherent control scheme***. *(a) The AUX laser is detuned by a frequency Ω from the MAIN laser frequency at ω_c and can be viewed as a single side-band (b) After the non-linear interaction in the OPO (which as we saw in part b) creates correlation between the side band at $+\Omega$ and $-\Omega$) , we see on the reflected beam the other side band at $-\Omega$ being created or not depending on the phase of the ellipse of squeezing. Demodulating this signal at 2Ω gives us an error signal to lock the phase of the pump with the phase of the AUX field. (c) In transmission of the OPO we have vacuum squeezing at ω_c and the two side-bands at $\pm\Omega$. (d) When recombining with the bright field, if we demodulate at Ω we obtain an error signal to lock the phase of the bright field with the AUX field. The later being locked in phase with the pump at (b) we have locked the phase of the bright field with the phase of the ellipse of squeezing.*

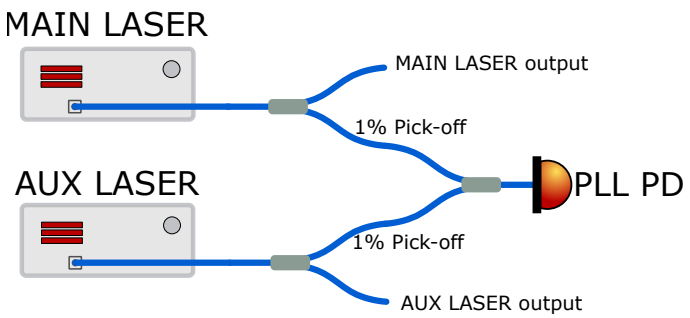

Fig. IV.26 *Schematics of the fiber-ed setup for the PLL. A small pick-off of each laser is sent to the PLL photodiode to measure the beatnote frequency between the two lasers*

Pyrpl that will give you the "In phase" component at a frequency f of your signal and the "Quadrature" component by demodulating it with an internal reference. On the basic Pyrpl there is a PFD (Phase Frequency difference) option in the IQ output that acts as an integrator. The integrator is incremented by one bit when the internal reference changes sign and is decremented by one bit when the input signal changes sign. This is actually quite a good error signal because it's very robust even if the two signals are very far in frequency. The integrator is coded on 14 bits so if the two signals are separated by 10 kHz the integrator will increase by 10 000 every second and so it would take 1.6 seconds to saturate the integrator. The only issue is when you are at the same frequency, you can have a phase difference of π and your error signal would be oscillating by 1 bit so it's not very precise. If we just take the quadrature signal, we would have a very precise value of the phase difference between the two but as soon as we are not at the same frequency there is no way of distinguishing if our input signal is oscillating too fast or too slow.

So we had to build our own error signal that would be a combination of both : We use the CORDIC (COrdinate Rotation Digital Computer) algorithm to compute the phase between the input signal and the reference with a full 2π range. This algorithm uses a type of dichotomy characterisation to find the angle so with only 9 steps of calculation we are able to compute our angle with a precision of 0.1°. Its simplicity is very useful to implement it on an FPGA board like the RedPitaya. This angle is then encoded on the 12 least significant bits of our error signal while the number of turns is coded on the two most significant bits. Compared with the PFD error signal that we had before it saturates much quicker but it will still give the proper "direction" for the lock.

d) Controlling the laser frequency

The laser offers two ways of controlling the frequency : you can control the temperature of the crystal which gives you a slow tuning over a few GHz and you can control the piezo that acts on the crystal which gives you a fast tuning over 100 MHz. We use the two digital output of the RedPitaya to do Pulse Width Modulation to control the temperature and send a high-voltage signal (the RedPitaya output is amplified by a Tegam amplifier) to the piezo. The high-voltage is low pass filtered at 10 Hz with a first order RC filter. To do the fast fine-tuning we use one of the fast outputs of the RedPitaya (125 MHz sample rate, 2 V range) that we plug directly on the floating mass of the piezo, the high voltage being plugged on the positive port of the piezo. Then using the RedPitaya we perform three locks simultaneously :

- The fast piezo out is locking the phase error signal to zero
- The slow piezo is using the fast piezo signal as an error signal and are locking it to 1 V i.e., the middle of their range so we can have robust and precise locking over a 100 MHz range.
- We use again the slow piezo signal as an error signal for the temperature output so we can keep the high-voltage signal in the middle of its range. This last lock is optional if you don't have big temperature drifts while keeping the lock.

e) Results

Using the techniques presented above, we were able to keep the lasers locked at 20 MHz from each other over the course of a full weekend with an RMS error of 2°. The lock was also implemented at Calva where they are an RMS error of 2°. The frequency can be arbitrary chosen on the RedPitaya. On Fig. IV.27, we monitored the different error and control signals during the lock acquisition. On (c) we see spectra of the beat note signal between the two laser during lock acquisition. The two beams are initially detuned by -5 MHz and after the lock sequence is switched on they are locked at +9 MHz in 0.4 s. On this measurement we are not able to differentiate positive and negative frequency difference. (d) The error and output signals during the lock acquisition : initially, the Cordic error is oscillating between -0.5 and -1 V because the phase is encrypted over 4 turns (from -4π to $+4\pi$) so when the phase difference between the actual beating and the target frequency is greater than 4π turn counter bits are saturated. However, in post process we can unwrap this signal and compute the actual phase difference as you can see on (e) which is a time zoom of the actual lock moment. When the lock is switched on, the fast piezo are the first to react but we see that they are immediately saturated, this triggers the slow piezo that will counter-react to put the fast piezo in the middle of their range and the cordic error at zero. The temperature slowly counteracts the slow piezo fluctuations. After 10 second, we are changing the phase set-point to generate figure (f) where we plotted the two quadrature values in the complex plane for various phases set-point showcasing the phase precision of the lock.

f) Syncing multiple RedPitayas

Now that we have locked out AUX laser at a frequency Ω from the MAIN laser, comes another difficulty : We need to demodulate the signal from two other photodiodes at the same frequency and perform feedback on those error signal, but the RedPitaya we are using only has one fast analog input available left. If we just use another RedPitaya, we would have a slow frequency drift coming from the fact that their internal references are not synced. To sync them, you can use the external clock input from the RedPitaya which requires a soldering modification on the board IV.28.

We then need an external clock source, we use a VersaClock 6E Programmable Clock Generator (5P49V60) mounted on a SparkFun board. The board is programmable via I2C code using an Arduino library. After correction of the code, we were able to generate four 125 MHz clock signals with LVDS level (the standard needed for the RedPitayas clock signal). You then just have to connect the RedPitayas clock inputs to the board and you can synchronize up to 4 RedPitayas (In our case we only needed to synchronize two). The last step is to make sure that the demodulation modules all start with the same phase. Even if the clocks are synchronized, the relative phase between the IQ module depends on the timing at which they were started. So we add a connector between two digital Input/Output of the RedPitayas, and when one of the RedPitays starts its IQ module it will send a signal to the other so that their internal reference at Ω always have the same phase relationship.

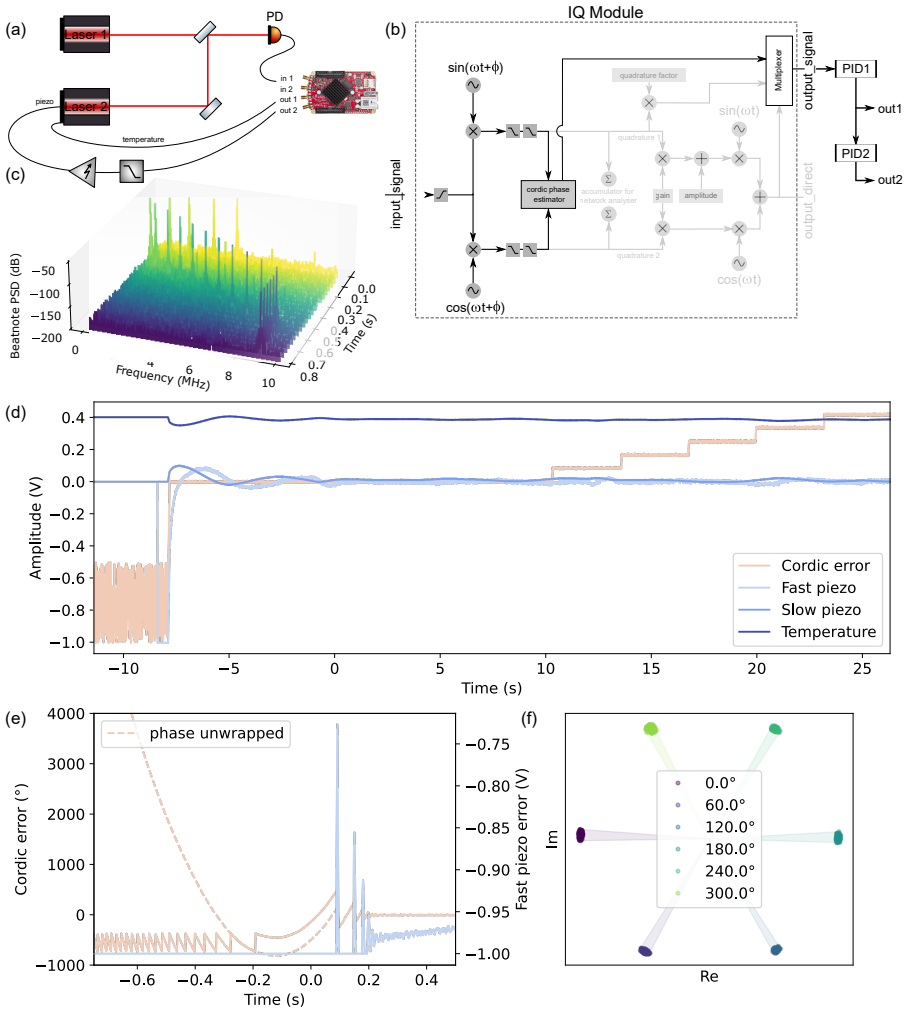

Fig. IV.27 *(a) Schematic of the optical setup and the laser frequency controlled by the RedPitaya : out1 is connected to the fast piezo output, out2 to the slow piezo, and the analog output is connected to the crystal temperature controller. The beating of the two lasers is acquired on the photodiode connected to in1. (b) Schematic of the IQ module used to compute the phase difference between the two lasers. The two quadratures are required to compute the angle via the cordic phase estimator. The error signal is then sent to PID1 that will control the fast piezo output. To ensure that we stay in the narrow tuning range of the fast piezo this fast piezo output signal is used as an error signal for PID2 that will control the slow piezo and ensure the fast piezo are always in the middle of their range. Finally, we do the same trick again and use the slow piezo output signal as a signal error for PID3 that will control the temperature of the laser crystal and ensure that the slow piezo also stay in the middle of their range over long duration.*

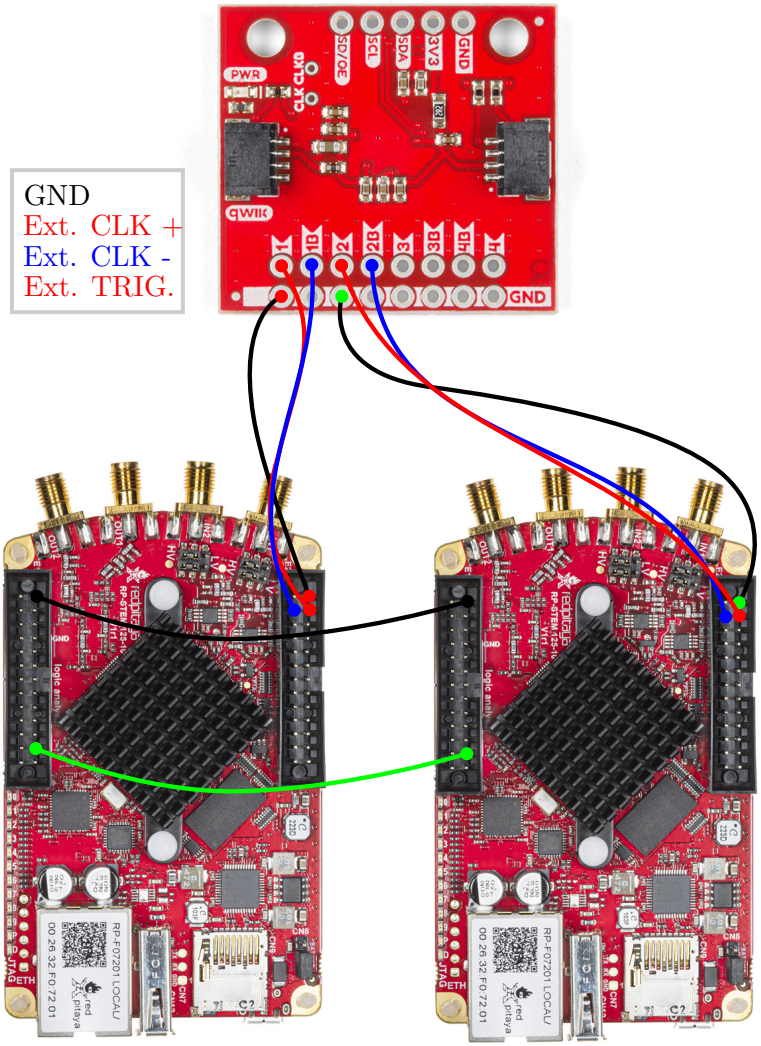

Fig. IV.28 ***Two synced RedPitayas***. *The small red board generates the external clock signal and the green cable between the two RPs ensure that the IQ modules keep a constant phase relationship.*

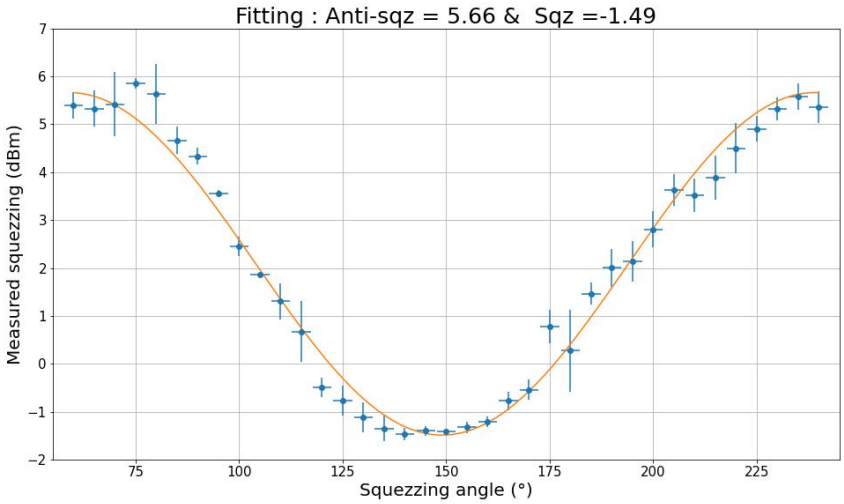

Fig. IV.29 *Level of phase noise as a function of the angle of the ellipse of squeezing. From the fit we can extract a maximum squeezing magnitude of 1.5 dB and a maximum anti-squeezing magnitude of 5.7 dB. This measurement was performed with 17 mW of pump power and the level of squeezing is measured on a 10 kHz bandwidth around 500 kHz.*

IV.9.2 Results

Once these technical problems were fixed, we can fully control our angle of squeezing using the two synchronized RedPitayas. They are two lockboxes on each RedPitaya : One locks the two lasers at a frequency Ω and performs the demodulation at 2Ω for the lock of the pump with the AUX beam while the other performs the demodulation at Ω for the lock of the bright field with the AUX beam and the lock of the homodyne detection (lock of the phase of the bright field with the local oscillator). We then obtain this first graph IV.29 where each point is taken separately because we can choose the phase relationship with the ellipse of squeezing.

And finally we can look at the broadband spectrum of our squeezed light for different values of the angle of squeezing on IV.30.

IV.10 Limitations and improvement

IV.10.1 Losses

As we saw in part II.3.10, optical losses degrade squeezing extremely quickly. The main source of loss in our setup is the optical circulator composed of a Faraday rotator and a PBS. Here is an estimation of the total loss on the optical path from the output of the OPO to the homodyne detection :

- Bright Field Beam splitter : 2.5 % (measured)

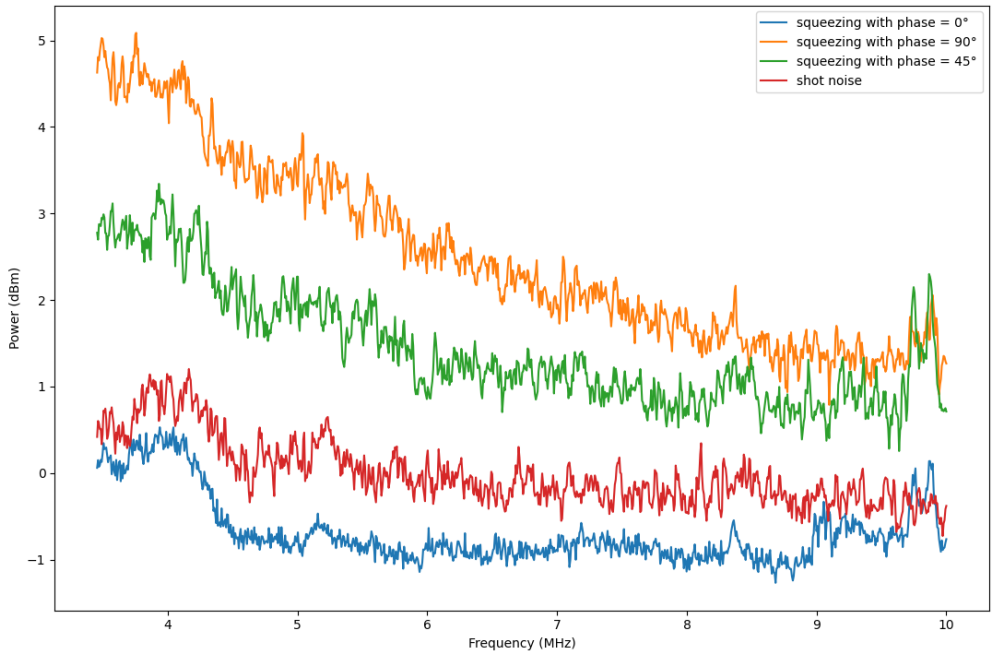

Fig. IV.30 *Spectrum of the phase noise measured on the homodyne detection for different values of the squeezing angle. At a null angle we have, in blue, a phase squeezed state slightly below the shot noise, in blue. For an angle of 90°, we see the anti-squeezed component of the field and at 45°, we see a mixture of the two quadratures. We see that the noise is not exactly flat due to excess phase noise.*

- 8 HR mirrors : 8 x 0.1 % (theoretical)
- 1 small mirror not HR coated : 1 % (measured)
- 4 λ-plates : 4 x 0.1 % (theoretical)
- 3 lenses : 3 x 0.5 % (theoretical)
- PBS : 0.2 % (measured)
- Optical rotator : 10 % (measured)
- Rotation cavity : 0.1 % (theoretical)

This gives us a total of 16.5 % of losses over all the optical path which corresponds to what we can measure. Most of these losses cannot be avoided but can be minimized by keeping clean optics and making sure that the polarization of the beam is optimal when hitting the bright field beam splitter (Reflectivity is very dependent on polarization) and going through the optical circulator. We also optimised the homodyne fringe visibility and reached $C = 95\%$. The estimated escape efficiency from the OPO is 94% and the

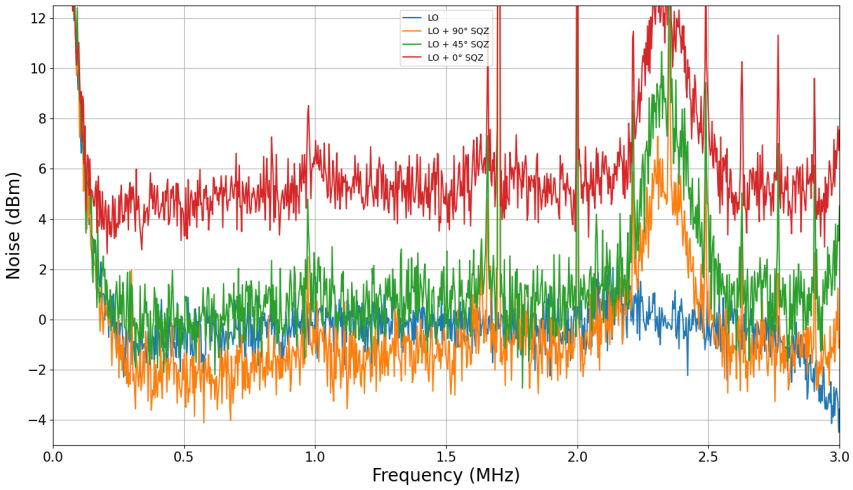

Fig. IV.31 *Same figure as IV.30 but with an optimized amplifying circuit for the photo-diode so we are shot noise limited from 300 kHz to 3 MHz which corresponds to the bandwidth where the resonance of our oscillator will be. We see that when we add the squeezed beam there are a lot of technical noise coming from the coherent sideband locking field. We are working on eliminating them but we do see 2 dB of squeezing around 500 kHz.*

efficency of the photodiode of our homodyne detection are specified to be higher than 99%. So we can compute the total efficiency of our squeezer

$$\eta_{tot} = \eta_{prop}\eta_h\eta_{PD} = 0.71 \tag{IV.1}$$

With this efficiency, using the formula II.107 we should see 5 dB of squeezing and 13 dB of antisqueezing for $x = 0.5$. We were never able to see such level squeezing but we were able to see such level of antisqueezing. So we suspect that we have parasitic phase noise that artificially degrades our level of squeezing.

IV.10.2 Phase noise

If we consider a phase noise of amplitude $\delta\theta$, the change in the measured quadrature can be written

$$S_{1,2}^{out} = S_{1,2}\cos^2\delta\theta + S_{2,1}\sin^2\delta\theta \tag{IV.2}$$

So for high level of antisqueezing, the squeezing is almost completely destroyed by the antisqueezing. This correspond well to our situation where we have been able to record high level on antisqueezing (up to 15 dB) but no more than 4 dB of antisqueezing. On figure IV.32 we can see the effect of phase noise for the two quadratures. We are currently investigating potential source of parasitic phase noise.

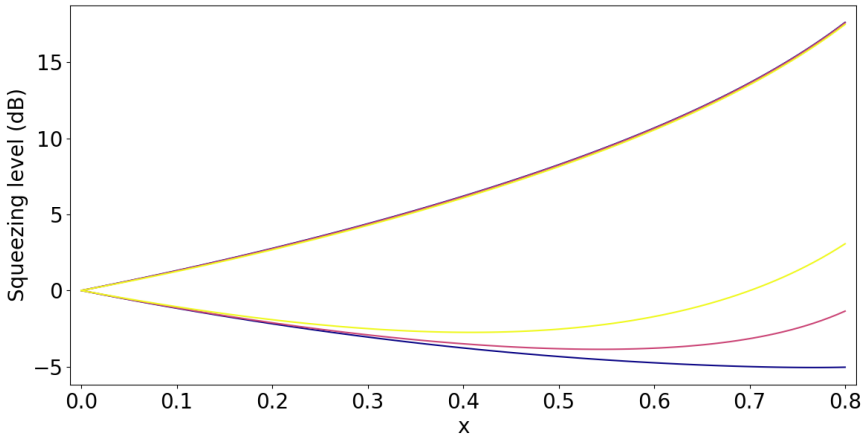

Fig. IV.32 **The effect of phase noise on squeezing**. *The squeezing/antisqueezing magnitude is plotted for* $x = \sqrt{P_{pump}/P_{thr}}$ *going from 0 to 0.8 (for values closer to unity, our formula is no longer exact since the assumption of no pump depletion starts to break down). The blue curves are for a phase noise of 1° rms, the pink ones for 5° rms and the yellow ones for 10° rms. Antisqueezing is mostly unaffected and the corresponding curves appear superimposed. We see that for 10° rms, there is no more than 2 dB of squeezing, which corresponds to our situation.*

IV.10.3 Temperature stability

The amount of squeezing produced by the OPO is very dependent on the temperature of the crystal. Right now we are using a Thorlabs TED 350 temperature controller with a precision of 0.03 °K and a stability of 0.003 °K but in practice we see some slow fluctuation of 0.02°K. Better tuning of the PID coefficients of the temperature controller could help but we struggled to do better given the lack of precision in the tuning of the coefficients (controlled by small knobs). We are considering using an homemade temperature controller to improve the temperature stability.

IV.10.4 Phase tuning

To control the phase of the various optical field we use a mirror mounted on a piezo glued on an aluminium piece. The error we made was to put the mirror at 45° so when the phase drifts a lot and the piezo has to compensate by doing a large displacement we start to deteriorate the beam alignment (moving the beam by a few microns). This effect starts to be problematic for long-term lock. The solution would be to change the beam path and have a much smaller angle of incidence on the moving mirror to limit beam displacement. Because it required a compete realignment of half the optical table we didn't take the time to do this improvement.

Fig. IV.33 *The clean room at the CALVA facility. The red vacuum chamber (called Ferrarix) houses the in-vacuum OPO, the homodyne detection and the telescopes used to mode-match the squeezed beam to the 50-m cavity. The grey vacuum chamber houses the input mirror suspension of the rotation cavity.*

IV.11 The Low-Frequency squeezer

While still working on the High-Frequency squeezer, I have also collaborated with the Virgo group at IJCLab in Orsay on a low-frequency frequency-dependent squeezer project, for a possible application to Advanced Virgo.

Advanced Virgo already has a squeezer, built by the Albert Einstein Institute in Hannover but it is frequency-independent. Indeed, for now, Advanced Virgo is only limited by QSN at high frequency but for the next runs, optical power will be increased and seismic noise further reduced, so it is expected that it will be limited (at least to some extent) by QRPN at low frequency as well. Consequently, a full frequency-dependent squeezer, including a 285-m long rotation cavity has been installed along the North arm of Advanced Virgo and will be operational for O4. But the OPO at the core of this squeezed light source is operated in air, and there are concerns that this will at some point limit the performance of the system (light scattering...). The experiment in Orsay, which takes advantage of the CALVA facility, a 50-m long cavity, uses an in-vacuum OPO and is a prototype of what could be a frequency-dependent squeezer for Advanced Virgo in a few years, after O5. Full details on this experiment can be found in Angélique Lartaux's thesis [69] but I will briefly present the setup and the current status of the project here.

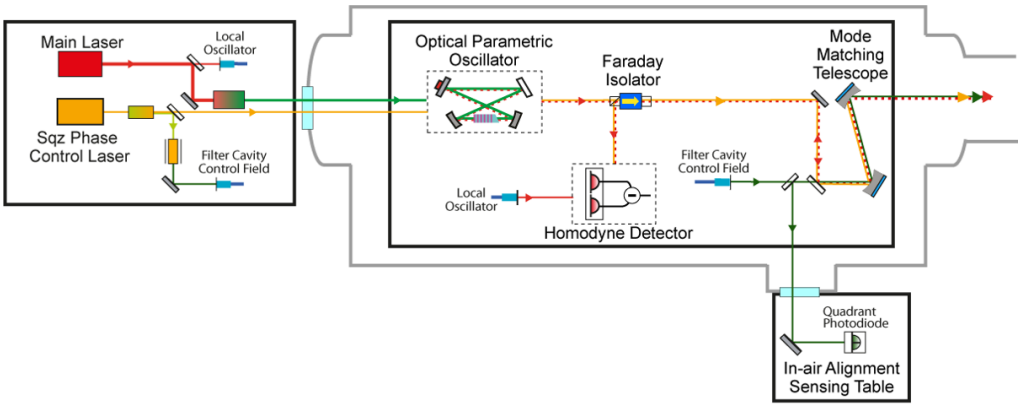

Fig. IV.34 *Experimental setup. On the left is the in-air bench where we have the main laser, the two SHGs and the Mach-Zender interferometer (not represented here). Then, under vacuum, we have the OPO, the homodyne detector and the 50-m long rotation cavity. Maintaining the alignment of such a long cavity requires extra-control fields and a quadrant photodiode detection.*

IV.11.1 The experimental setup

The experimental setup is quite similar to the one for the HF squeezer presented in the previous sections. The OPO, pumped by the green light produced by the SHG, creates frequency-independent squeezing that becomes frequency-dependent after reflection on the rotation cavity. The main differences are:

- The OPO and the detection photodiodes are in vacuum to reduce the beam path fluctuations caused by air motion, which has a non negligible effect under 1 kHz.
- The green pump is stabilized in intensity using a Mach-Zender interferometer to reduce very slow intensity fluctuations.
- It uses of modified coherent sideband locking instead of standard coherent sideband locking, which produces an error signal of better quality to control the ellipse of squeezing.
- And finally, it takes advantage of a 50-m rotation cavity with a bandwidth of 1 kHz to match an SQL frequency of 1 kHz (still to high for Advanced Virgo where one needs a bandwidth of 50 Hz, but this is a first step).

Apart from this, the SHGs are exact replicas from the one at LKB, and the OPO is almost exactly identical. For now, for obvious tuning/optimizaton reasons, the OPO is still operated in air.

a) Modified coherent sideband locking

The concept of Modified coherent sideband locking is explained in figure (IV.35). The idea is similar to coherent sideband locking (Fig. IV.25), but this time the auxiliary laser (AUX) field, detuned from the MAIN laser by a frequency Ω pumps a second SHG and

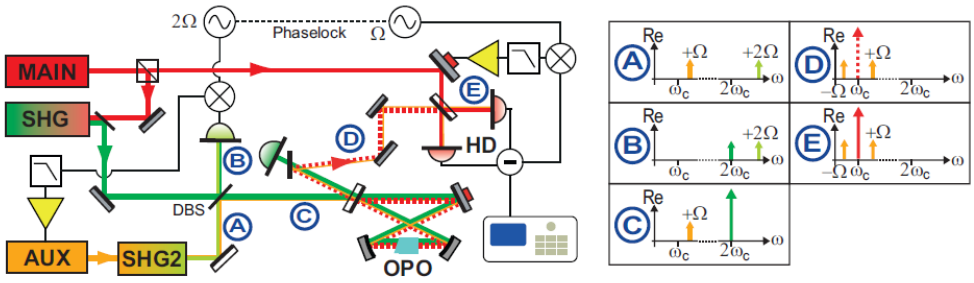

Fig. IV.35 **Modified coherent sideband locking**. *The auxiliary laser (AUX) field, detuned from the MAIN laser by a frequency Ω pumps a second SHG and generates a harmonic field at $2\omega_0 + 2\Omega$. After attenuation of the AUX, the two fields will co-propagate towards the OPO (A). The Dichroic Beam Splitter (DBS) transmits green and reflects infrared. The beatnote between the pump at $2\omega_0$ and the AUX harmonic at $2\omega_0 + 2\Omega$ (B) is demodulated at 2Ω to maintain the detuning between the MAIN and the AUX at Ω. The auxiliary field reflected by the DBS now enters the OPO cavity via the input coupler.*

generates a harmonic field at $2\omega_0 + 2\Omega$. After attenuation of the AUX, the two fields will co-propagate towards the OPO (A). We insert a Dichroic Beam Splitter (DBS) right before the OPO, that transmits green and reflects infrared. In the reflection, we get the beatnote between the pump at $2\omega_0$ and the AUX harmonic at $2\omega_0 + 2\Omega$ (B). This signal is demodulated at 2Ω to maintain the detuning between the MAIN and the AUX at Ω. This also sets the phase relationship between the reflected auxiliary field and the pump field (Here we save one phase lock compared to standard sideband locking using the phase relation of the SHG process but at the cost of an extra SHG). The auxiliary field reflected by the DBS now enters the OPO cavity via the input coupler and not a high reflectivity coupler (as it was the case for standard coherent sideband locking). So the non-linear interaction in the OPO is much stronger and all the error signals (that are now the same as in standard coherent sideband locking) will be greater.

This scheme yields an error signal of better quality to control the angle of squeezing, at the expense of an extra SHG. The PLL uses a RedPitaya and PyRPL, as the one at LKB. We have obtained a stable lock over more than 10 hours with a 2° rms error of phase between the two lasers. For now, we are still working on the alignment of the OPO so the other loop has not been tested yet.

IV.11.2 Results

As mentioned previously, the OPO is still causing issues and we are investigating if the crystal is working properly. But we have been able to send the LO field on the homodyne photodiodes and characterize the dark noise and the shot noise. This measurement has shown that the LO is shot-noise limited only above 1 kHz. Below, we see large peaks dominant over shot noise, probably due to seismic noise or resonant mechanical motion of optical components, driven by sound. These should be removed by vacuum operation. (IV.36).

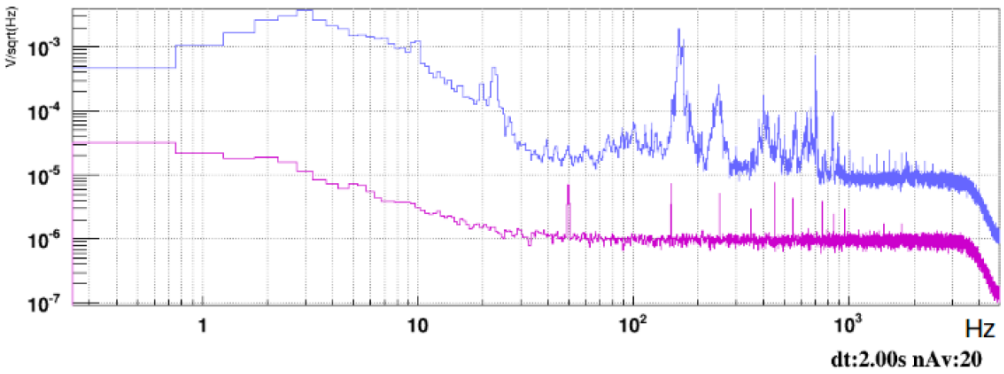

Fig. IV.36 ***Noise spectrum of the homodyne detection.*** *The signals are band-pass filtered between 2Hz and 4 kHz. On the dark noise (purple curve), notice a peak at 50 Hz and some peaks at higher frequency. Blue curve: noise obtained for 2.5 mW of power on the LO. We see that from 1 kHz to 3.5 kHz, we have a flat noise that corresponds to shot noise, but below 1 kHz, we see large peaks, probably due to seismic noise or mechanical resonances of some optical components.*

IV.12 Conclusion and perspectives

The High-Frequency squeezer is producing controlled frequency independent squeezing, meaning all parts of the experiment function, apart from the rotation cavity. However the setup still requires improvement, as we should be able to see a higher level of squeezing and reduce the amount of technical noise visible on the squeezing spectra. The different cavities and phase locks work but still require otimization to reduce parasitic phase noise. This is the main priority to improve the amount of squeezing measurable.

For the rotation cavity, we still have to figure out how to lock it with a detuning matching the resonant frequency of the oscillator so roughly 1 MHz. Our main idea so far would be to add a phase modulation at 1 MHz and use the sideband to lock the cavity or use a higher order mode that would be detuned from the TEM_{00} mode from 1 MHz. The first solution requires to add a phase modulator at 1 MHz which is not so simple. The second solution requires the rotation cavity to not be perfectly mode-match which will add losses on the squeezing that can be characterized [46]. The best solution would be to send a frequency shifted beam on the other port of the rotation cavity on a separated polarization axis than the squeezing so there are no interaction between the two. And then use the reflected beam to lock the cavity to the frequency shifted field. By controlling the frequency of the shift, we could control the detuning of the cavity. But the output port of the rotation cavity is highly reflective so there would be very little signal to lock the cavity. This is still under discussion.

The low frequency squeezer is still under development but working at low frequencies where vibrations noise are much more present adds a lot of complications for the experiment. However we can already say that we should not have any issue observing

and controlling squeezing above 1 kHz as we are already shot noise limited above this frequency and the coherent control sideband locking all ready works at LKB.

Chapter V

An optomechanical system dominated by radiation pressure noise

As discussed in Chapter III, one of the main challenges in the field of optomechanics has always been to design and fabricate a resonator with both optimum mechanical and optical properties: high mechanical Q, low optical losses... in order to optimize the coupling to the optical field. In this regard, µg-scale resonators with dielectric coatings are not optimal. In this chapter, I will present the next-generation optomechanical system with which sub-SQL will hopefully be performed in the group.

V.1 Context

In 2016, Sheon Chua started the design and assembly of the squeezer setup described in the previous chapter. The idea at the time was to combine it with the cooling experiment discussed in Chapter III, so the two experiments were developed side by side for 2 years before I joined LKB. The squeezer was set-up on two breadboards to be easily installed near the dilution cryostat. As we progressed with the cooling experiments, Thibaut Jacqmin and Samuel Deléglise started to experiment with a new kind of optomechanical resonator: a very thin and highly-stressed membrane of silicon nitride.

This resonator has very good quality factors that can go up to 10^9 using patterning techniques described by Edouard Ivanov in his thesis. Its only downside it it has relatively poor optical properties (a reflectivity around 40%). It also has a very small mass (typically 50 ng), so it appeared at the time not very interesting for the "macroscopic" cooling experiments. However, to perform a displacement measurement below the SQL, having a small mass is of course better because you increase the ratio between QRPN and thermal noise. So it was decided we would use a membrane of which we master the fabrication process, instead of a macroscopic resonator fabricated by Francesco's Marin group.

In the last year of my PhD, the LKB group also bought a new "dry" dilution cryostat from BlueFors, giving access to base temperatures below 10 mK. The old cryostat that we had used for the macroscopic cooling experiments was causing a lot of issues at the time, and still consumed lot of liquid helium liquid, of which the price has gone up recently. Given the old cryostat performance we decided to use the new cryostat for the sub-SQL

Parameter	Symbol	Optimistic value	Pessimistic value
Optical power	P_{in}	1 mW	1 µW
Mechanical quality factor	Q	10^9	10^6
Optical Finesse	$\mathcal{F}$	30 000	4 000
Temperature	T	10 mK	1 K
Resonance frequency	$\Omega_m/2\pi$	1 MHz	
Mass	m	50 ng	

Table V.1: Envisioned parameters for a QRPN-limited optomechanical system.

displacement measurement experiment as well. Adding an optical access to the cryostat is doable but it would add quite a lot of technical difficulties and could affect affect its cooling performance. This cryostat being now used for microwave experiments requiring only electrical access, we decided to go with a fibered setup that would require minimal modification of the squeezer setup and minimal disturbance to the other experiments taking place in the cryostat.

As discussed below, the new design we have opted for involves a number of innovations compared to our previous experiments:

- a nanomechanical membrane as mechanical resonator
- a phononic crystal design to increase the mechanical Q and isolate the resonator from cryostat vibrations
- a new cryostat, with only a fiber access
- a membrane-in-the-middle optical setup...
- ... with an indirect bending-induced position-tuning of the membrane.

In this chapter, I will present these different steps and how we have started addressing and characterizing them separately, to obtain a good working knowledge of each of them to confidently consider building a full system that incorporates them all. The full design will be presented in Sec. V.5.4.

V.2 Desired specifications

The goal of the experiment is to demonstrate sub-SQL position measurements with the 1064-nm squeezed light source discussed in Chap. IV. A required intermediate step is obviously to perform a displacement measurement limited by QRPN. This requires classical thermal noise to be lower than QRPN. As established in Sec. II.5, the ratio between the two respective spectral densities is :

$$R = S_F^{RP}/S_F^{Th} = \frac{16\hbar P_{in} Q \mathcal{F}^2}{\lambda c \pi k_B T m \Omega_m}. \tag{V.1}$$

Actually, for a silicon nitride membrane, the quality factor, the mass and the resonance frequency are related to the size l of the membrane in such a way ($Q \propto l$, $\Omega_m \propto l^{-1}$ and $m \propto l^2$) that R is independent of l. From previous experience, we know that a resonator in the MHz range greatly simplifies the experiment by avoiding classical noise. We can easily control the amount of optical power injected into the cavity thanks to the squeezer design, the only limitation being the sample heating caused by optical absorption which is hard to determine.

Optimizing the finesse is still a work in progress: by design, our empty cavity finesse can be up to $100,000$, but adding the membrane will bring extra-losses. From the literature, most groups have an optical finesse in the $10,000$ range. From previous experiments with the macroscopic resonator and a study from Rémi Metzdorff during his PhD [65], we know a short cavity ($< 400\,\mu$m) is best for a high finesse to avoid parasitic coupling of the TEM_{00} fundamental mode to higher-order transverse modes. Another constraint is that the waist of the optical beam must be smaller than the size of the membrane to avoid optical loss and ensure a good optomechanical coupling.

V.3 The Silicon Nitride Membrane

These resonators are fabricated from a silicon wafer coated with a $\simeq$ 100-nm thick film of silicon nitride deposited with a very large pre-stress. The silicon is then etched in the center using Potassium Hydroxide (KOH) to liberate the thin membrane. The pre-stress allows to greatly increase the mechanical quality factor, the mechanical energy associated with the out-of-plane vibrational modes being stored in the elongation of the film, rather than in the bending. The main source of loss is now the clamping of the membrane at the edge.

The boundary conditions impose a large bending of the membrane at the edge, causing loss particularly for high-order mechanical modes with displacement extrema located near the edge. To prevent this, the membrane can be patterned with a phononic crystal composed of a regular array of holes (visible on Fig. V.1). A single defect is present in the center of the phononic crystal allowing for at least one soft-clamped vibrational mode to exist and to be localized in the center of the membrane.

The joint design of the crystal and of the defect sets the resonance frequency of the defect mode inside a gap of the vibration mode density of the crystal (see Fig. V.1). As a consequence, the mode profile quickly decreases far from the center of the membrane and the corresponding vibration amplitude is completely negligible at the edge. This soft-clamping technique allows to take full advantage of the mechanical dilution induced by the mechanical stress of the membrane. More details on the fabrication and the physics of these membranes can be found in [74]. The phononic crystal also ensures a better isolation of the oscillator motion from parasitic vibrations inside the cryostat. In the experiment presented in this chapter, I have only worked with a standard square membrane for preliminary tests.

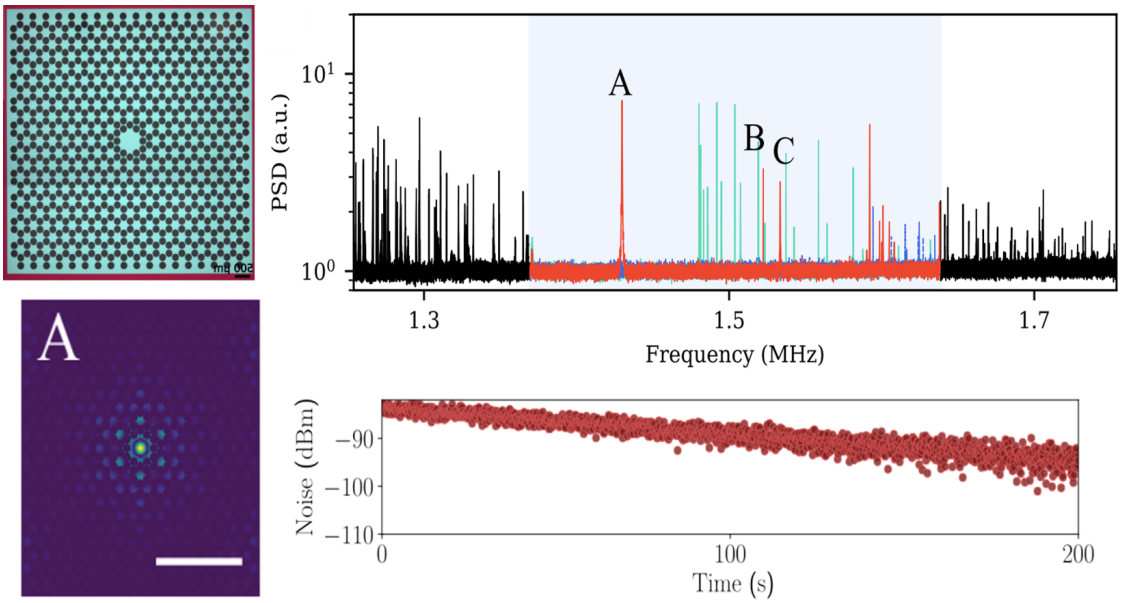

Fig. V.1 **A phononic-crystal SiN membrane as a high-Q optomechanical system**. *Top Left: Optical view (false color) of a 2.5 mm × 2.5 mm × 100 nm membrane, with a phononic crystal and a defect. Bottom: Simulated profile of the fundamental defect mode. Top right: Noise spectrum, with only a few localized modes of the defect present in the frequency gap of the phononic crystal. The mode A is the main mode of interest. Bottom right: Mechanical decay measurement of the Q of the fundamental mode of a non-patterned membrane. The Q value is here above* 10^8 *at* $\simeq 1$ *K, which makes us optimistic we can reach* 10^9 *with a patterned membrane in a dilution fridge.*

V.4 The new dilution cryostat

The group recently bought a new dilution cryostat from Bluefors (Model BF-LD 250) that can go down to 10 mK in less than 24 hours (see Fig. V.2). It is a dry cryostat that doesn't require liquid helium transfer. It does however have a pulse-tube that can cause parasitic vibrations that could make optomechanics experiments particularly complicated. We took the option to add an helium battery to the cryostat in order to be able to turn off the pulse-tube for 2-3 hours. In case the vibrations are too problematic, this should give us a small window of time to perform measurements. The cryostat is now mainly used for the microwave experiments led by Samuel Deléglise and Thibaut Jacqmin. It has no optical access but does have a fiber feed-through: the idea is to put a fibered cavity inside and inject the squeezed beam via a fiber. If the fibers bring to much loss and make the measurements impossible, there is still the possibility to add an optical access.

V.5 Cavity design

The idea is to adapt the micro-pillar/wheel resonator cavity design, described in Chap. III, that has proved to be robust and flexible. It indeed allows to align the two mirrors

Fig. V.2 ***The new LKB Bluefors cryostat.*** *The pulse tube has been isolated by building a small cabin around it. The wooden box is also for acoustic isolation. We don't know yet if this will have any effect for the vibrations disturbing the sample, but we can already tell the difference for the acoustic vibrations disturbing the PhD students.*

of the cavity in front of each other with a good precision in terms of cavity length and finesse, because we can measure both while aligning the cavity and then lock the cavity in place once we are satisfied with the numbers. In the following sections, I will present experiments from other group that we have used as inspirations to come up with this design.

V.5.1 Membrane In the Middle (MIM) cavity

The first experiment discussed pioneered the field of membrane optomechanics.

a) Characteristics and results

In this paper [22], Jack Harris and his group designed a 6.7-cm long optical cavity containing a 1-mm^2 and 50-nm thick SiN membrane. They managed to reach a finesse of 15 000 for the optical cavity and a mechanical quality factor of 1.1×10^6. The cavity is rigid and they tune the laser to resonance with an acousto-optic modulator (AOM). The

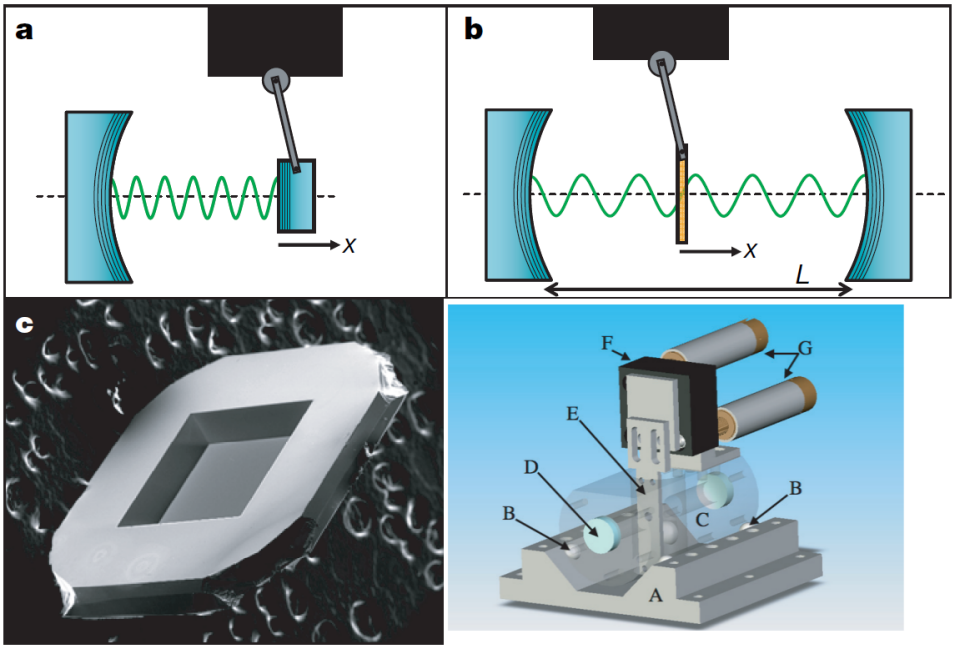

Fig. V.3 ***The Membrane In the Middle experiment from Jack Harris' group.*** *(a) and (b) display the classical optomechanical system vs. the membrane-in-the-middle cavity setup (c) Photograph of a SiN membrane (1 mm x 1 mm x 50 nm) on a silicon chip. (d) Design of the optical cavity. The Invar support (A) is mounted inside the vacuum chamber. Alumina spheres (B) provide kinematic mounting between the support and the Invar cavity spacer (C). The end mirrors (D) define the optical cavity. The membrane and piezoelectric elements are mounted to the Invar arm (E) which is in turn mounted to the tilt stage (F), which can be adjusted in situ by two actuators(G). Figure from [75].*

membrane position and tilt are controlled with a 6-axis position stage, which appears crucial to reach a high finesse. They were able to optically cool the membrane from room temperature down to $\simeq 7$ mK.

b) Issues for our experiments

The first issue of this design for our experiment is its footprint. We want to put the membrane in a dilution cryostat to be able to reach lower temperature and higher Q. But putting a 6.7-cm long optical cavity in a dilution cryostat is impossible, which means miniaturizing the whole design is necessary. The main constraint is the membrane positioning stage, that is fairly big and forces them to use a long cavity. Also, reducing the cavity length is crucial to reach a high finesse as it reduces parasitic coupling between the fundamental optical mode and higher-order modes. Another issue is the laser tuning. As we want to perform a displacement measurement of the resonator with a bright squeezed field, we cannot use an AOM to tune the laser frequency. As a consequence, we need to be able to control the length of the cavity and the position of the membrane while keeping a compact design.

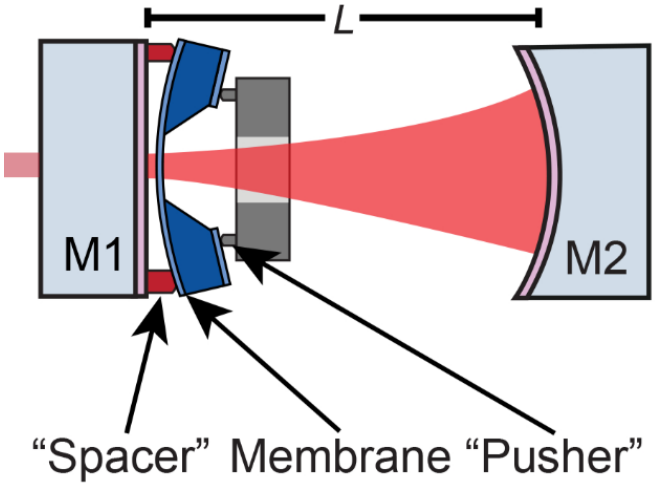

Fig. V.4 ***The MATE cavity experiment from Jack Sankey's group.*** *It is made of an input mirror M1, 21-µm thick spacers, a membrane, piezo-actuated pushers, and a "backstop" mirror (not to scale). The length $L = 10$ cm between M1 and M2 is tuned with piezo actuators on M2. Figure from [24].*

V.5.2 Membrane At The Edge (MATE) cavity

The group of Jack Sankey proposed an interesting alternative to the MIM cavity, by putting the membrane very close to one of the mirrors instead of in the middle of the cavity. To control the position of the membrane with respect to the mirrors, they use both "spacers" and "pushers" (see Fig. V.4) to bend the membrane, effectively bringing it closer to the mirror. This design is much more compact and easier to align, the silicon frame of the membrane being fixed to one of the mirrors. It also gives access to larger optomechanical couplings [24]. However, their experiment uses a 10-cm long cavity and a tunable laser, so we still need to miniaturize it and add some way to tune the cavity length.

V.5.3 Fiber Fabry-Perot cavity

The last source of inspiration for the design was the fibered Fabry-Perot cavity designed by Jakob Reichel's group [76]. They were able to use a CO_2 laser to fabricate a concave, ultralow-roughness surface at the end of the fiber. The fiber end is also coated with a 12-ppm coating, allowing them to reach a finesse of $130,000$. The fibered setup allows a very compact cavity design, with a length of a few microns and an easy alignment setup. Finally, the fiber is glued on a shear piezo to tune the length of the cavity.

Our idea is to have the membrane at the edge close to a flat mirror like in J. Sankey's experiment and use a carved fiber as an input mirror. This would give a compact setup with full control of the length of both sub-cavities and an easy fibered access, via a fiber port on the cryostat.

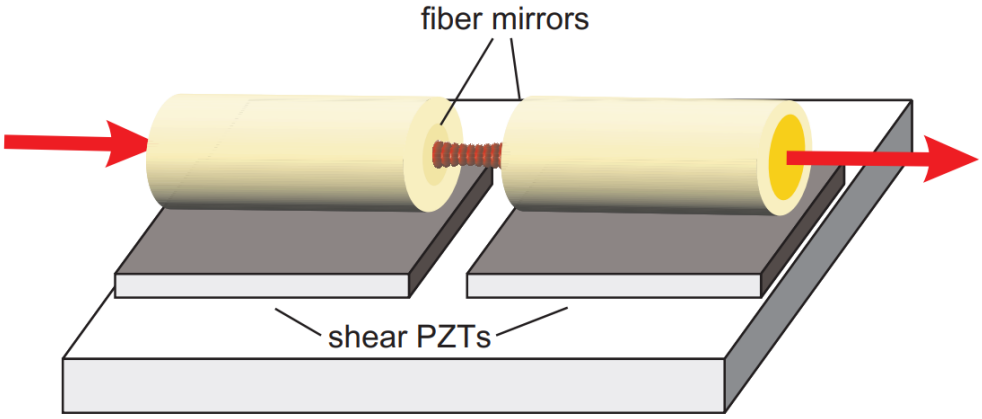

Fig. V.5 ***Miniature mounts for a tunable Fiber Fabry-Perot Cavity by Jakob Reichel's group.*** *Piezoelectric transducers are used to scan the cavity length. All other alignment is done during assembly. Figure from [76].*

V.5.4 LKB design

We have tried to make a design similar to the Fabry-Perot cavity already used in the cooling experiments, that works fine for alignment and stability and is easily tunable. We have kept the "cavity-top" part and just replaced the µ-RoC with a flat mirror (from LaserOptik). We then put double-sided Kapton tape as "spacers" on the edge of the mirror and place the membrane on top of it. We then mount the "cavity-top" part of the "cavity holder" the same way as before. The three "pushers" (Thorlabs F2DSES8) are screwed inside the cavity top with a fine thread and come to contact with the membrane. When the pusher PZT move, the membrane bends and we can tune the length between the flat mirror and the membrane. Until now, we haven't placed a fiber on the setup yet but the idea is to put it inside the ferrule and glue it on the shear piezo so the fiber can move freely inside the ferrule and the cavity length can easily be tuned. The ferule will just fit tightly inside the "cavity holder" part without any degree of freedom regarding the angle. To align the cavity, we plan to use the same procedure as before but we have added a thread inside the "cavity holder" to tune the angle with the "cavity top" if needed.

To just test how the membrane behaves when we bend it, we replace the input fiber by a curved mirror of RoC 2.5 cm. The mirror is glued on a piezo and mounted on a Thorlabs mount attached to the cavity via a cage system. We then build a 1.7-cm long cavity, with an empty cavity finesse of $28,000$.

V.6 The modified optical field dynamics

The membrane placed between the two mirrors of the cavity will change the field dynamics. In this section, I will derive the optomechanical coupling of the system and estimate the decay rate of the cavity.

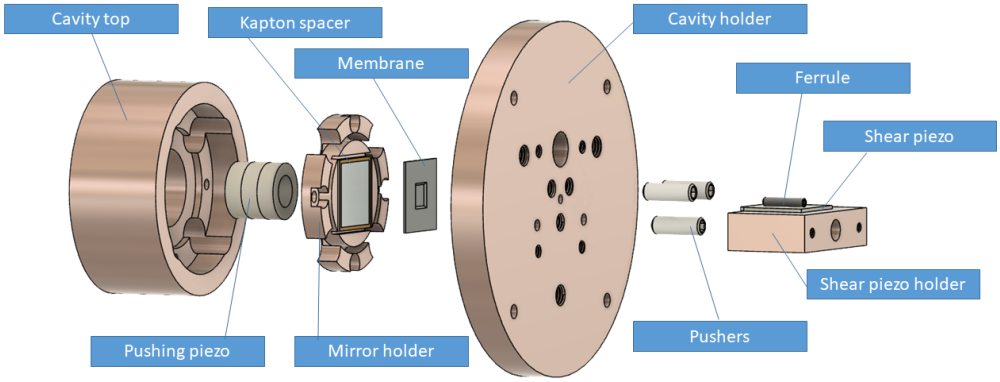

Fig. V.6 *Exploded view of the fiber MATE cavity design. The "cavity top" and "mirror holder" parts are the same as before. The "cavity holder" has been modified with extra threads for the "pushers", a hole to fit the ferrule and 2 extra threads to put screws holding the "shear piezo holder". The shear piezo holder has a hole in the middle for the pusher.*

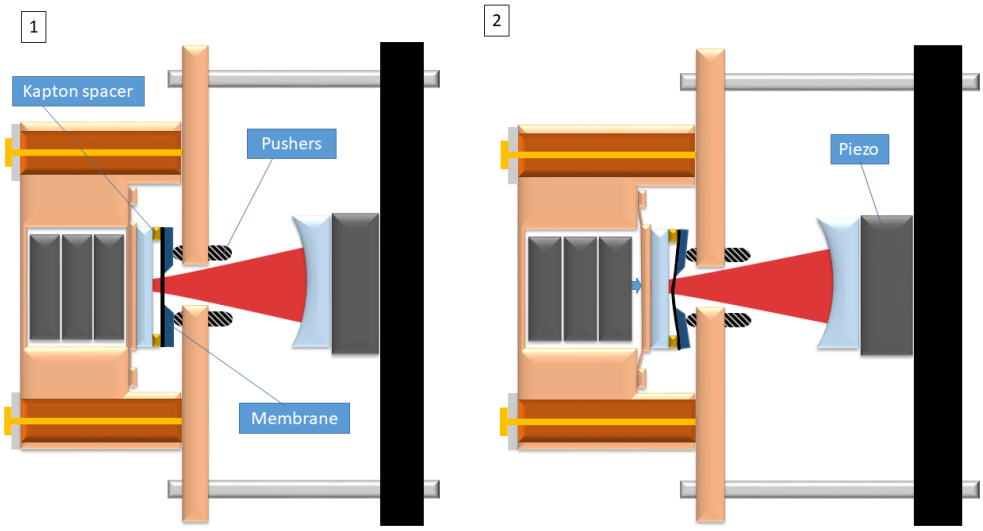

Fig. V.7 *Schematic view of the pusher/spacer system with the preliminary "membrane bending test" cavity.*

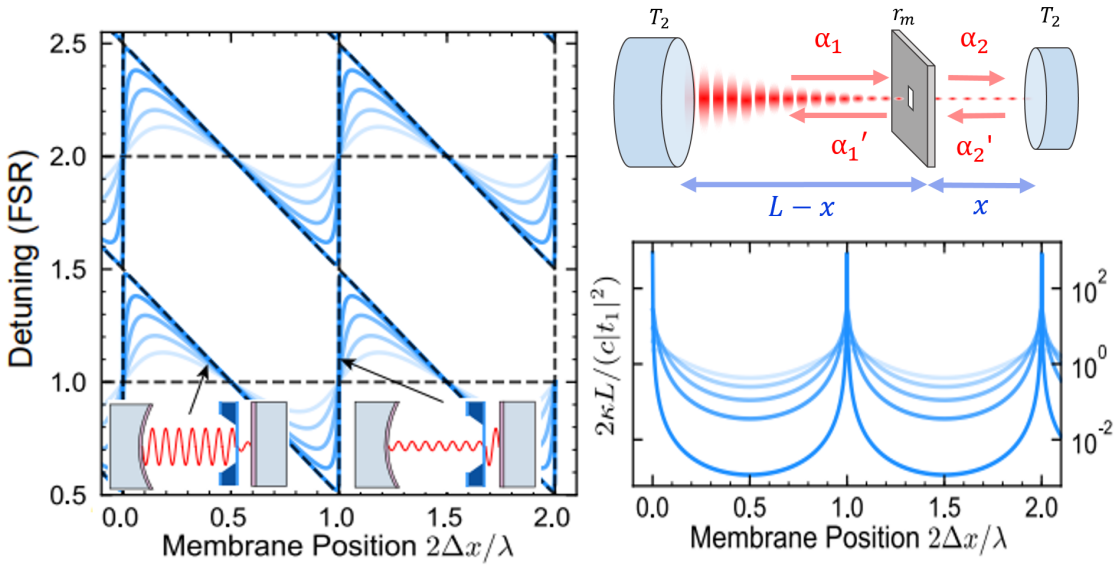

Fig. V.8 **Optical resonances for a membrane-at-the-edge cavity**. *Top right: schematic view of the cavity, in reality $x \ll L$. Left: Dependence of the cavity resonance detuning (normalized by the free spectral range (FSR)) on membrane displacement x from the back mirror with r_m values (from light to dark) -0.4, -0.6, -0.8, -0.931, and -0.9977. The horizontal dashed lines represent empty cavity resonance frequencies ($r_m = 0$), and the vertical dashed lines represent the left and right sub-cavity resonances when $t_m = 0$. Inserts qualitatively show the field distribution of these modes. Bottom right: Dependence of the cavity energy decay rate on membrane displacement, normalized by the empty single port cavity decay rate ($r_m = 0$, $r_2 = -1$). Figure adapted from [24].*

V.6.1 The optomechanical coupling

The field of optomechanics has taken advantage of a lot of different geometries to couple an optical resonator to a mechanical resonator. Whatever the geometry is, standard optomechanics equations such as the ones presented in Chap. II can always be used as long as we assume a linear coupling between the resonator displacement and the resonance frequency of the cavity. This coupling $G = \frac{\partial \omega_{cav}}{\partial x}$ is quite simply defined in the case of a linear Fabry-Perot cavity as

$$G = \frac{\partial \omega_{cav}}{\partial x} = \frac{1}{\tau}\frac{\partial \psi_{cav}}{\partial x} = \frac{2k}{\tau}. \tag{V.2}$$

We use this value to calibrate the optical phase measurements into displacement measurements. I will now compute it in the case of a partially reflective membrane in the middle of a high-finesse cavity, based on calculations in [24].

We consider a cavity of length L, as represented on Fig. V.8. We will note α_1 and α_2 the field propagating from left to right in the left and right parts of the cavity and α_1' and α_2' the counter-propagating fields. The membrane has a reflectivity r_m and a transmission

t_m and is placed at a distance x from the back mirror. We can write

$$\alpha_2 = t_m \alpha_1 + r_m \alpha_2' \tag{V.3}$$
$$\alpha_1' = t_m \alpha_2' + r_m \alpha_1. \tag{V.4}$$

We assume a high-finesse cavity with mirror reflectivities $r \approx 1$, so after a single round-trip the fields are related by:

$$\alpha_1 = -\alpha_1' e^{2ik(L-x)} \tag{V.5}$$
$$\alpha_2' = -\alpha_2 e^{2ikx}. \tag{V.6}$$

Combining the previous equations, we get the following resonance condition:

$$(t_m^2 - r_m^2)e^{ikL} - e^{ikL} = 2|r_m| \cos(2kx - kL). \tag{V.7}$$

From here we can solve the equation numerically for a lossy membrane, but if we make the assumption that the membranes is lossless (such that $|t_m|^2 + |r_m|^2 = 1$), we can write

$$-\cos(kL + \phi_r) = r_m \cos(2kx - kL), \tag{V.8}$$

where ϕ_r is the phase of the membrane reflectivity. Expanding the cosine, we can find the resonating cavity length :

$$L = \frac{1}{k} \arctan\left[\frac{\cos\phi_r + |r_m|\cos(2kx)}{\sin\phi_r - |r_m|\sin(2kx)}\right]. \tag{V.9}$$

This expression will be particularly helpful as the cavity length is scanned to resonate with the laser and not the other way around. We now want to compute the resonance frequency. We will make the assumption that the length L of the cavity is large compared to the wavelength λ, so the wavenumber occupying the cavity $k_N = \pi N/L$ is large and the perturbation induced by the membrane is small. So we can write $k = k_N + \delta k$ with $\delta k \ll k_N$. We also make the assumption that the membrane is positioned very close to the end mirror and only performs small displacements compared to the cavity length, such that $x \ll L$. So the product kx now becomes

$$kx = k_N \delta x, \tag{V.10}$$

and from equation (V.9), we can compute the resonance frequencies of the cavity, represented on Fig. V.8 as a function of the membrane position:

$$\omega_{MATE} = kc = \omega_{FSR}\left(N + \frac{1}{\pi}\arctan\left[\frac{\cos\phi_r + |r_m|\cos(2k_N\delta x)}{\sin\phi_r - |r_m|\sin(2k_N\delta x)}\right]\right). \tag{V.11}$$

Taking the derivative by δx we get the optomechanical coupling :

$$G = c\frac{\partial k}{\partial x} = \frac{2k_N}{\pi}\omega_{FSR}\frac{|r_m|(|r_m| + \cos(2k_N\delta x + \phi_r))}{(|r_m|^2 + 2|r_m|\cos(2k_N\delta x + \phi_r) + 1)^2} \tag{V.12}$$
$$= 2G_{FP}\frac{|r_m|(|r_m| + \cos(2k_N\delta x + \phi_r))}{(|r_m|^2 + 2|r_m|\cos(2k_N\delta x + \phi_r) + 1)^2} \tag{V.13}$$

where G_{FP} is the optomechanical coupling of a standard Fabry-Perot.

V.6.2 Cavity dissipation

The optomechanical coupling computed above depends on the membrane reflectivity. One way to measure it is to measure the cavity reflection and transmission as a function of the cavity detuning as has been done in Section II.2.5, and to measure the cavity decay rate as a function of the membrane position. This decay rate can be computed by considering the total energy stored in the cavity as the sum of the energy of the two sub-cavities, that can be written as:

$$E = P_1\tau_1 + P_2\tau_2, \tag{V.14}$$

where P_i is the power circulating in the sub-cavity i and τ_i is the sub-cavity's lifetime such that $\tau_1 = 2(L-x)/c$ and $\tau_2 = 2x/c$. The energy leaks out of the two mirrors with a rate:

$$\frac{\partial E}{\partial t} = -P_1T_1 - P_2T_2 \tag{V.15}$$

Using Eqs. (V.4) and (V.6), we can compute the ratio

$$\frac{P_2}{P_1} = \left|\frac{\alpha_2}{\alpha_1'}\right|^2 = \frac{1+|r_m|^2+2|r_m|\cos(2kx+\phi_r)}{1-|r_m|^2}. \tag{V.16}$$

and eliminate P_2 from equation (V.14) to express P_1 as

$$P_1 = \frac{cE}{2}\left((L-x) + x\frac{1+|r_m|^2+2|r_m|\cos(2kx+\phi_r)}{1-|r_m|^2}\right)^{-1}. \tag{V.17}$$

The global leak rate κ such that

$$\frac{\partial E}{\partial t} = -\kappa E \tag{V.18}$$

can be expressed as

$$\kappa = \frac{(1-R_m)cT_1 + (1+2|r_m|\cos(2kx+\phi_r)+R_m)cT_2}{2x(1-R_m)+2(L-x)(1+2|r_m|\cos(2kx+\phi_r)+R_m)}, \tag{V.19}$$

where $R_m = |r_m|^2$. For $|r_m| = 0$, we retrieve the standard Fabry-Perot cavity decay rate $\kappa = (T_1+T_2)/\tau$. This expression is valid for every cavity geometry but fairly complicated.

κ is plotted for $T_2 = 0$ on Fig. V.8 and we get:

$$\kappa = \frac{(1-R_m)cT_1}{2x(1-R_m)+2(L-x)(1+2|r_m|\cos(k(L-x)+\phi_r)+R_m)}. \tag{V.20}$$

If we make the membrane-at-the-edge approximation, we get

$$\kappa = \kappa_1\frac{1+|r_m|^2+2|r_m|\cos(2kx+\phi_r)}{1-|r_m|^2}, \tag{V.21}$$

where $\kappa_1 = cT_1/2L$ is the empty cavity decay rate. We see that the decay rate is the empty cavity decay rate multiplied by the ratio P_2/P_1 . Indeed, if the majority of the energy of the cavity is in the right part of the cavity (where there is no loss source), then the global loss of the cavity will be small and vice-versa. We can also see that if the majority of the energy of the cavity is in the right part of the cavity (which is very short), the resonance frequency of the optical mode will be very sensitive to the membrane displacement, hence the high slope in these regions (see Fig. V.8) and vice-versa: when the majority of the power is in the left, the long cavity will barely be effected by the membrane displacement, hence the small slope.

V.7 Results

V.7.1 The optomechanical coupling

In the first experiments, we just wanted to make sure we were able to tune the membrane position and see an effect on the frequency of the optical modes of the cavity. To do so, we scanned the cavity length using the front piezo of the input curved mirror for different DC values of the voltage applied to the back piezos acting on the membrane position. Doing so, we see series of equally separated peaks corresponding to the cavity resonances. As we change the membrane position for each scan, we see these frequencies shifting, according to Eq. (V.11):

$$\omega_{MATE} \approx ck_{MATE} = \frac{c}{2L}(N\pi + \arctan\left[\frac{\cos(\phi_r) + |r_m|\cos(2k_N\Delta x)}{\sin(\phi_r) - |r_m|\sin(2k_N\Delta x)}\right], \tag{V.22}$$

where $k_N = \pi N/L$ is the N^{th} resonant mode of the empty cavity, with $N \gg 1$. The frequency difference between two resonances is constant and still corresponds to the cavity free spectral range, which we know by just measuring the length of the cavity. This allows us to calibrate the scan in frequencies. For an empty cavity ($r_m = 0$), we just have a straight line with a constant slope because as we push the back mirror, we also sweep the cavity length $L \to L + K\Delta x$ where K is a geometrical factor to take into account the bending of the membrane. For a cavity with a membrane, we see a wave pattern starts to appear on top of the straight line which is a clear sign we are moving the membrane position inside the cavity (see Fig. V.9).

V.7.2 The cavity decay rate

For each scan, we can also measure the width of the resonances, which correspond to the cavity decay rate κ. As the membrane goes through the nodes and antinodes of the standing wave inside the cavity, it will increase or decrease the decay rate and we obtain oscillations as a function of the membrane position, according to Eq. (V.21):

$$\kappa = \frac{(1-|r_m|^2)c|t_1|^2 + (1+2|r_m|\cos(2kx+\phi_r) + |r_m|^2)c|t_2|^2}{2L(1+2|r_m|\cos(2kx+\phi_r) + |r_m|^2)}. \tag{V.23}$$

By taking into account the piezo non-linearity (the voltage we apply to the back piezo doesn't transduce linearly in displacement), we can fit this function and obtain the membrane reflectivity $|r_m|^2$. This formula assumes a perfectly reflective membrane and perfect alignment of the membrane with the cavity mirrors. This explains the discrepancy between expected value and measured value. From the parameters of the fit, we can deduce the values of $T_1 = 220$ ppm, $T_2 = 1000$ ppm and $R_m = 0.36$. This value matches very well the theoretical value as silicon nitride has an optical index specified to be 2.01, which gives a reflectivity of 0.34 [77]. We did a preliminary test with an empty cavity and found $T_1 = 188$ ppm and $T_2 = 36$ ppm, and the specified values for the coatings done by LMA are $T_1 = 100$ ppm and $T_2 = 20$ ppm. So we can conclude that $T_1 \approx 200$ ppm, that the empty cavity has 20 ppm of extra losses and that the membrane adds 1000 ppm of losses. We don't know yet if these losses come from beam clipping by the membrane frame or the membrane itself being dirty or tilted with respect to the back mirror. For now, the

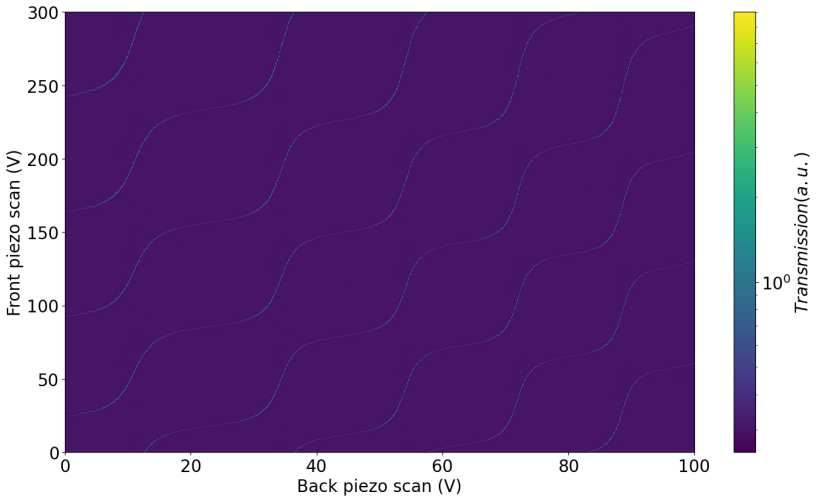

Fig. V.9 *Transmission of the MATE cavity for a length scan using the cavity front piezo for various back piezo voltage values. The bright lines correspond to cavity resonances separated by one FSR. We see an upward trend due to the cavity length being shortened as we sweep the back mirror position, and superimposed oscillations due to the effective displacement of the membrane being pushed by the back mirror.*

highest finesse we have measured is $\mathcal{F} = 6,700$. From the measured value of R_m, we can compute the maximal value of the mechanical coupling:

$$G_{max} = \frac{4ck_N}{L}\frac{1}{|t_m|^2} = \frac{4}{|t_m|^2}G_{FP} = 0.65\,\frac{\text{GHz}}{\text{nm}}, \tag{V.24}$$

for a cavity length of 17 mm. We see that the MATE cavity optomechanical coupling is increased by a factor 6.25 compared to the standard Fabry-Perot optomechanical coupling.

V.8 Conclusion

So far, our design seems to work as planned, as we are able to control precisely the position of the membrane. We were able to calibrate the membrane reflectivity, which matches the value measured in literature [77] and to measure a cavity finesse of 6,700. We now need to investigate where the excess optical noise comes from by using different sizes of membranes and putting an extra care on membrane cleanliness. We can also tune the position of the pushers to try to control the tilt of the membrane with respect to the back mirror. For now, other groups [22, 13, 23, 24, 25] have reported cavity finesse values only around 10,000 so it's not sure we can do a lot better. The cavity has been installed inside a vacuum chamber and the next step will be to measure the thermal noise of the membrane at low pressure. This will be useful to characterize its mechanical properties and have a better idea of what the SQL frequency will be. This will be crucial to choose the rotation cavity characteristics II.5.5.

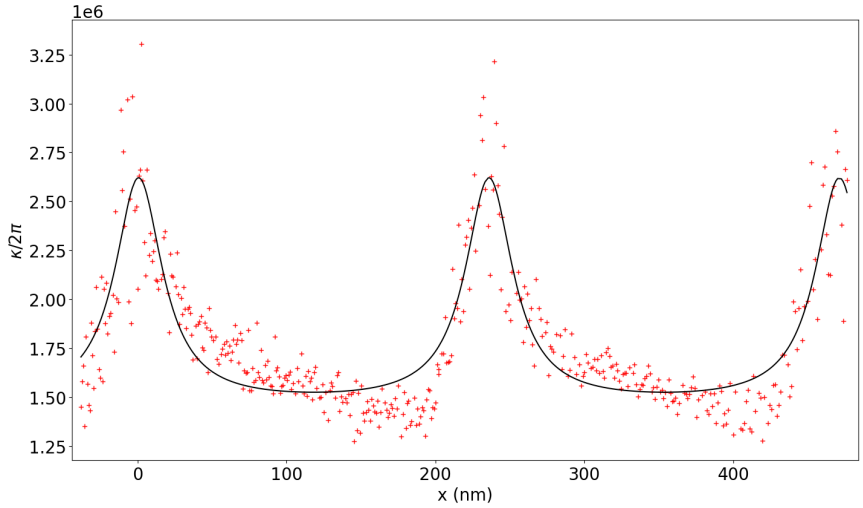

Fig. V.10 **Decay rate of MATE cavity as a function of the membrane position**. *We see that as the membrane goes through the nodes and antinodes of the standing wave inside the cavity, we increase or decrease the decay rate of the cavity.*

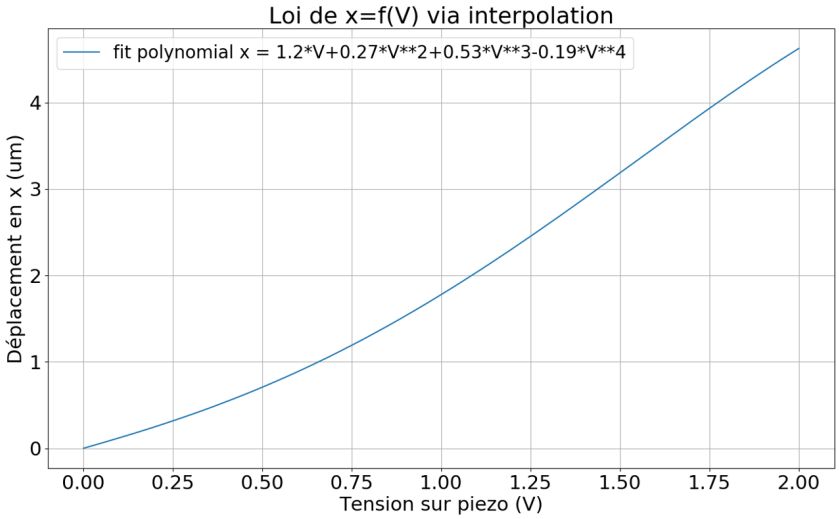

Fig. V.11 *Membrane position as a function of the voltage applied to the back piezoelectric transducer.*

Summary, conclusion and perspectives

After the introduction to this thesis and a quick panorama of the field of optomechanics, I have briefly presented in Chapter II the theoretical elements required to discuss and understand the experiments performed during this PhD work. I have shown how the quantum nature of an optical field sets a fundamental limit, the Standard Quantum Limit, to the sensitivity of interferometric continuous position measurement. I have then introduced non-linear optics and presented how it allows to produce squeezed light and actually to perform measurements beyond the SQL. Thermal position noise is still dominant for most optomechanics experiments and I have shown how optomechanics provides the tools to overcome this noise by reducing the effective temperature of a macroscopic mechanical resonator well below its environment temperature.

In Chapter III, I have presented the results I have obtained cooling macroscopic resonators close to their quantum ground state. I have presented a first kind of mechanical resonator, a mm-scale quartz µ-pillar. Such a resonator has long been designed, fabricated and operated in the group but, despite some interesting samples, it's been unfortunately characterized by a very complex multi-step fabrication process and very low reproducibility of its mechanical properties from one sample to the other, particularly its mechanical quality factor. I have recalled the experimental results obtained by Remi Metzdorff during his PhD, with a cooling down to 6 phonons, and I have presented a thorough statistical analysis I have performed to compute an uncertainty of ± 0.4 on this number.

I have then presented and characterized a new kind of mechanical resonator, designed and fabricated by the group of Francesco Marin, the wheel resonator, and discussed mechanical quality factor measurements from room temperature down to 4 K, that display very consistent properties from one sample to the other. I have also presented and discussed the cooling results obtained for these resonators, down to a temperature similar as the one demonstrated with the µ-pillar but due to their lower resonance frequency, this still corresponds to a higher number of residual phonons, with $n_{ph} = 87 \pm 3$.

To improve this result would require to improve the proper functioning of the dilution cryostat. During the second part of this thesis, the cryostat indeed displayed a base temperature getting higher and higher at each of the last cool-downs, most likely due to a small leak in the dilution circuit that we haven't been able to find. A better working cryostat would mean a lower thermalization temperature for the optomechanical resonator, which would improve the results in two ways.

Firstly, a lower environment temperature would mean a higher mechanical quality factor. During the last experimental runs, we indeed observed day-to-day variations

of the quality factor as the cryostat struggled to stabilize at its base temperature. As a higher mechanical Q means a stronger signal-to-noise (or noise-to-noise) ratio of the thermal peak above the sensitivity floor, it implies lower temperatures achievable with feedback cooling as the noise floor is the current limit of the experiment.

Secondly, if the temperature of the resonator is lower, we obviously need less optical cooling to reach the quantum ground state. It should be noted that, other things being equal, with our current setup, an increase by a factor 10 at most on the quality factor and a decrease by a factor 10 of the thermalization temperature would be sufficient to reach the ground state.

Another way to improve the results would be to try a new design of the resonator, combining the best features of the two resonators:

- using an elongation mode, such as the one used for the pillar experiment, that gives a very high resonance frequency, with minimal clamping losses...
- but fabricating it in silicon, using the same lithography technique as for the wheel resonator, that proved to make highly reproducible samples, and optimising the frame of the resonator to limit the negative impact of low frequency modes.

Once a lower phonon number is achieved, another interesting upgrade of this experiment would be to characterize the quantum behaviour not only by the level of position noise, a quantitative feature that requires a careful calibration procedure to compute the phonon number, but by demonstrating a sheer qualitative feature such as sideband asymmetry of the Stokes and anti-Stokes sidebands using a heterodyne detection. The idea of such a measurement is to address and detect individually the two sidebands, which scale respectively as n_{ph} and $n_{ph}+1$. Such a measurement was actually attempted during Remi's PhD, when the µ-pillar was cooled down to 6 phonons, but limited signal-to-noise ratio with a very weak heterodyne probe beam prevented any conclusive result.

The next (much longer term) step would be to try to demonstrate a possible gravitational decoherence effect. This would require to put the resonator into a non-Gaussian state, for example a cat state, which is not possible using only linear optomechanical effects (that can only map an input Gaussian state to another Gaussian state). The most promising platform for such an experiment involves a SiN membrane, resonantly coupled to a superconducting qubit, which provides the nonlinear interaction. At LKB, there is a strong dedicated experimental effort led by Samuel Deléglise and Thibaut Jacqmin. The photonic-crystal SiN nanomembrane is a moving electrode for a capacitor, embedded in an LC circuit, with a resonance frequency depending on the membrane position. The LC-circuit is coupled as well to the qubit. One of the notable experimental challenges is to design and fabricate a superconducting qubit with a frequency that matches the mechanical resonance frequency, typically in the MHz range (SiN mechanical resonators at 5 MHz have been demonstrated recently by the team), to be compared with the usual GHz frequency of such qubits.

In Chapter IV, I have described in great technical detail the design of the squeezed light source developed at LKB. We have designed a SHG that is able to produce more than 300 mW of power at 532 nm. We have then demonstrated that the OPO is able

to produce up to 4 dB of squeezing. We have also set up a phase lock-loop between the main laser and the coherent control laser, that keeps the laser at a stable detuning with a typical rms error of 2° for more than 14 hours. We have also demonstrated the control of the squeezing ellipse, but the simultaneous operation of all systems and control loops only allowed the demonstration of controlled squeezing with a noise reduction between 1 and 2 dB.

This modest intermediate result most likely stems from uncontrolled phase noise due to the various feedback loops being still not optimised. This is clearly the first issue to address. Reducing optical losses is next on the to-do list. One may think of:

- improving the mode-matching of the homodyne detection.
- reducing propagation losses.

The mode-maching efficiency indeed scales quadratically with the fringe visibility. A fringe visibility of 99 % should be attainable by putting the mode-matching lens on a translation stage to finely tune the position of the beam waist. Propagation losses could probably be reduced by optimising the loss due to the optical circulator, which is now about 10%. We still do not know if this is an issue related to the polarization rotator or to the polarizing beam splitter, but other experiments [78] have been able to reduce this number down to 1 %. Using a triangular rotation cavity would also be a solution as the input and output beams would be spatially separated and no circulator would be required, but it does involve one extra mirror in the cavity, meaning higher cavity losses, which are worse than propagation loss as they couple antisqueezing and not vacuum to squeezing. There is also the issue of scattering to the counter-circulating optical mode that should be characterized.

Once these issues are taken care of and the frequency-dependent squeezing has been demonstrated with the addition of the rotation cavity, an improvement we started thinking about was to use a 3-mirror rotation cavity. In this configuration, the first two mirrors form a sub-cavity that can be tuned around its resonance to work as an effective input mirror with tunable optical reflectivity. This would make the bandwidth of the cavity tunable to some extent, which will be useful on the long term to perform SQL-limited measurements on a set of optomechanical resonators as the SQL frequency will depend on the mechanical quality factor of the resonator and the intracavity power. Such characteristics will indeed vary from one sample to the other so some tuning range on our rotation cavity bandwidth will be an interesting feature of the final setup. The final challenge will be to couple the squeezed light to an optomechanical cavity through an optical fiber while keeping optical losses to a minimum. This will require great care in the coupling of the squeezed field into the fiber.

Finally, in Chapter V, I have described the different steps of the progression toward the design of an optomechanical system that will be limited by QRPN. To do so, I have first given a summary of three different cavity designs demonstrated by other research groups before actually presenting our own. I have then presented the results we obtained on a preliminary design with a curved mirror instead of the input fiber mirror. These results demonstrate that it is is indeed possible to effectively tune the membrane position inside

the cavity with a sufficient sensitivity, and to obtain a maximal finesse of 6000. I eventually derive some expected numbers for the future operation at cryogenics temperature.

Though it started already about 5 years ago, this research project is still quite far from completion. We have so far only checked the optical properties of the system but the membrane cavity is mounted in a vacuum chamber and we expect to be able to measure thermal noise at low pressure, even with a basic optical setup and a modest displacement sensitivity, quite soon. Such a measurement would already give the mode frequencies and the corresponding mechanical quality factors, which should already be quite high. Other groups have reported issues where the thermal motion of the membrane is so large that the cavity cannot be kept at resonance [79].

Finally, operating the fiber mirror cavity in the cryogenic environment is foreseen to be quite challenging. For examples, optical stability at the required level might be an important issue to deal with. Indeed, the new dilution cryostat works with a pulse-tube, which adds a lot of low-frequency vibrations. Hopefully, the soft clamping of the membrane will however provide sufficient passive isolation. Thermalization of the membrane in such a cryogenic cavity is also a matter of concern.

To address all these challenges, I'm happy to pass the torch to Pierre-Édouard who started his PhD about a year ago, and to whom I wish the best as he embarks on this fascinating but demanding (or demanding but fascinating?) journey.

Bibliography

[1] A. et al.; «Observation of gravitational waves from a binary black hole merger»; Physical Review Letters **116**, p. 061 102 (2016). ISSN 10797114. https://journals.aps.org/prl/abstract/10.1103/PhysRevLett.116.061102. vii, 1

[2] C. M. Caves; «Quantum-Mechanical Radiation-Pressure Fluctuations in an Interferometer»; Physical Review Letters **45**, p. 75–79 (1980). ISSN 0031-9007. http://link.aps.org/doi/10.1103/PhysRevLett.45.75http://prl.aps.org/abstract/PRL/v45/i2/p75_1. vii

[3] R. Schnabel; «Gravitational wave detectors: Squeezing up the sensitivity»; Nature Physics **4** (2008). vii

[4] H. P. Yuen; «Two-photon coherent states of the radiation field»; Physical Review A **13**, p. 2226 (1976). ISSN 10502947. https://journals.aps.org/pra/abstract/10.1103/PhysRevA.13.2226. vii

[5] C. M. Caves; «Quantum-mechanical noise in an interferometer»; Physical Review D **23**, p. 1693–1708 (1981). ISSN 0556-2821. http://link.aps.org/doi/10.1103/PhysRevD.23.1693. vii, 23

[6] C. M. Caves; «New formalism for two-photon quantum optics. I. Quadrature phases and squeezed states»; Physical Review A **31**, p. 3068–3092 (1985). ISSN 0556-2791. http://link.aps.org/doi/10.1103/PhysRevA.31.3068. vii

[7] A. et al.; «Enhanced sensitivity of the LIGO gravitational wave detector by using squeezed states of light»; Nature Photonics **7**, p. 613–619 (2013). ISSN 1749-4885. http://www.nature.com/doifinder/10.1038/nphoton.2013.177. vii

[8] A. et al.; «Increasing the Astrophysical Reach of the Advanced Virgo Detector via the Application of Squeezed Vacuum States of Light»; Physical Review Letters **123**, p. 231 108 (2019). ISSN 10797114. https://journals.aps.org/prl/abstract/10.1103/PhysRevLett.123.231108. vii

[9] C. Baker; *On-chip nano-optomechanical whispering gallery resonators*; Thèse de doctorat; Université Paris-Diderot; Paris (2013). viii

[10] J. D. Teufel, T. Donner, D. Li, J. W. Harlow, M. S. Allman, K. Cicak, A. J. Sirois, J. D. Whittaker, K. W. Lehnert & R. W. Simmonds; «Sideband cooling of micromechanical motion to the quantum ground state.»; Nature **475**, p. 359–363

(2011). ISSN 1476-4687. http://www.ncbi.nlm.nih.gov/pubmed/21734657. viii, 8, 9, 51

[11] P.-F. Cohadon, A. Heidmann & M. Pinard; «Cooling of a Mirror by Radiation Pressure»; Physical Review Letters **83**, p. 163 174 (1999). ISSN 0031-9007. http://link.aps.org/doi/10.1103/PhysRevLett.83.3174. viii, 7

[12] R. Schnabel; «Einstein would be doubly amazed»; Physics Today **75**, p. 46 (2022). ISSN 0031-9228. https://physicstoday.scitation.org/doi/abs/10.1063/PT.3.5063. 2, 3

[13] T. P. Purdy, P.-L. Yu, R. W. Peterson, N. S. Kampel & C. A. Regal; «Strong Optomechanical Squeezing of Light»; Physical Review X **3**, p. 031 012 (2013). ISSN 2160-3308. http://link.aps.org/doi/10.1103/PhysRevX.3.031012. 5, 10, 120

[14] A. et al.; «Quantum Backaction on Kg-Scale Mirrors: Observation of Radiation Pressure Noise in the Advanced Virgo Detector»; Physical Review Letters **125**, p. 131 101 (2020). ISSN 0031-9007. 6

[15] Y. et al.; «Quantum correlations between light and the kilogram-mass mirrors of LIGO»; Nature **583**, p. 43–47 (2020). ISSN 0028-0836. 6

[16] O. Arcizet, P.-F. Cohadon, T. Briant, M. Pinard & A. Heidmann; «Radiation-pressure cooling and optomechanical instability of a micromirror.»; Nature **444**, p. 71–74 (2006). ISSN 1476-4687. http://www.ncbi.nlm.nih.gov/pubmed/17080085. 7

[17] S. Gigan, H. R. Böhm, M. Paternostro, F. Blaser, G. Langer, J. B. Hertzberg, K. C. Schwab, D. Bäuerle, M. Aspelmeyer & A. Zeilinger; «Self-cooling of a micromirror by radiation pressure.»; Nature **444**, p. 67–70 (2006). ISSN 1476-4687. http://www.ncbi.nlm.nih.gov/pubmed/17080084. 7

[18] A. H. Safavi-Naeini, J. Chan, J. T. Hill, T. Alegre, A. Krause & O. Painter; «Observation of Quantum Motion of a Nanomechanical Resonator»; Physical Review Letters **108**, p. 033 602 (2012). ISSN 0031-9007. http://link.aps.org/doi/10.1103/PhysRevLett.108.033602. 9

[19] L. Neuhaus, R. Metzdorff, S. Zerkani, S. Chua, J. Teissier, D. Garcia-Sanchez, S. Deleglise, T. Jacqmin, T. Briant, J. Degallaix, V. Dolique, G. Cagnoli, O. L. Traon, C. Chartier, A. Heidmann & P.-F. Cohadon; «Laser cooling of a Planck mass object close to the quantum ground state»; (2021). https://arxiv.org/abs/2104.11648v1. 10, 48, 50, 54

[20] S. Gröblacher, K. Hammerer, M. R. Vanner & M. Aspelmeyer; «Observation of strong coupling between a micromechanical resonator and an optical cavity field.»; Nature **460**, p. 724–7 (2009). ISSN 1476-4687. http://www.ncbi.nlm.nih.gov/pubmed/19661913. 10

[21] D. K. Armani, T. J. Kippenberg, S. M. Spillane & K. J. Vahala; «Ultra-high-Q toroid microcavity on a chip»; Nature **421**, p. 925–928 (2003). ISSN 0028-0836. 10

[22] A. M. Jayich, J. C. Sankey, B. M. Zwickl, C. Yang, J. D. Thompson, S. M. Girvin, A. A. Clerk, F. Marquardt & J. G. E. Harris; «Dispersive optomechanics: a membrane inside a cavity»; New Journal of Physics **10**, p. 095 008 (2008). ISSN 1367-2630. http://stacks.iop.org/1367-2630/10/i=9/a=095008?key=crossref.252fc7193dae0f986a14ff7316a8a9fe. 10, 111, 120

[23] S. A. Saarinen, N. Kralj, E. C. Langman, Y. Tsaturyan & A. Schliesser; «Laser cooling a membrane-in-the-middle system close to the quantum ground state from room temperature»; (2022). 10, 120

[24] A. Kato, V. Dumont, S. Bernard, J. C. Sankey, C. Reinhardt & M. Ruf; «Flexure-tuned membrane-at-the-edge optomechanical system»; Optics Express, Vol. 27, Issue 18, pp. 25731-25748 **27**, p. 25 731–25 748 (2019). ISSN 1094-4087. https://opg.optica.org/viewmedia.cfm?uri=oe-27-18-25731&seq=0&html=truehttps://opg.optica.org/abstract.cfm?uri=oe-27-18-25731https://opg.optica.org/oe/abstract.cfm?uri=oe-27-18-25731. 10, 113, 116, 120

[25] J. R. Pratt, A. R. Agrawal, C. A. Condos, C. M. Pluchar, S. Schlamminger & D. J. Wilson; «Nanoscale torsional dissipation dilution for quantum experiments and precision measurement»; Rapport technique (2021). 10, 120

[26] A. H. Safavi-Naeini & O. Painter; «Design of optomechanical cavities and waveguides on a simultaneous bandgap phononic-photonic crystal slab.»; Optics express **18**, p. 14 926–43 (2010)ISSN 1094-4087. http://www.ncbi.nlm.nih.gov/pubmed/20639979. 10

[27] N. Parappurath, F. Alpeggiani, L. Kuipers & E. Verhagen; «Direct observation of topological edge states in silicon photonic crystals: Spin, dispersion, and chiral routing»; Science Advances **6** (2020). ISSN 23752548. https://www.science.org/doi/10.1126/sciadv.aaw4137. 10

[28] H. X. Tang, M. Li & W. H. P. Pernice; «Optomechanical coupling in photonic crystal supported nanomechanical waveguides»; Optics Express, Vol. 17, Issue 15, pp. 12424-12432 **17**, p. 12 424–12 432 (2009). ISSN 1094-4087. https://opg.optica.org/viewmedia.cfm?uri=oe-17-15-12424&seq=0&html=truehttps://opg.optica.org/abstract.cfm?uri=oe-17-15-12424https://opg.optica.org/oe/abstract.cfm?uri=oe-17-15-12424. 10

[29] J. D. Teufel, T. Donner, M. a. Castellanos-Beltran, J. W. Harlow & K. W. Lehnert; «Nanomechanical motion measured with an imprecision below that at the standard quantum limit.»; Nature nanotechnology **4**, p. 820–3 (2009). ISSN 1748-3395. http://www.ncbi.nlm.nih.gov/pubmed/19893515. 10, 54

[30] J. Bochmann, A. Vainsencher, D. D. Awschalom & A. N. Cleland; «Nanomechanical coupling between microwave and optical photons»; Nature Physics **9**, p. 712–716 (2013). ISSN 1745-2473. http://www.nature.com/doifinder/10.1038/nphys2748. 10

[31] N. R. Bernier, L. D. Tóth, A. Koottandavida, M. A. Ioannou, D. Malz, A. Nunnenkamp, A. K. Feofanov & T. J. Kippenberg; «Nonreciprocal reconfigurable microwave optomechanical circuit»; Nature Communications 2017 8:1 **8**, p. 1–8 (2017). ISSN 2041-1723. https://www.nature.com/articles/s41467-017-00447-1. 10

[32] K. Hammerer, M. Aspelmeyer, E. S. Polzik & P. Zoller; «Establishing Einstein-Poldosky-Rosen Channels between Nanomechanics and Atomic Ensembles»; Physical Review Letters **102**, p. 020 501 (2009). ISSN 0031-9007. http://link.aps.org/doi/10.1103/PhysRevLett.102.020501. 10

[33] K. W. Murch, K. L. Moore, S. Gupta & D. M. Stamper-Kurn; «Observation of quantum-measurement backaction with an ultracold atomic gas»; Nature Physics **4**, p. 561–564 (2008). ISSN 1745-2473. http://www.nature.com/doifinder/10.1038/nphys965. 10

[34] D. Hunger, S. Camerer, M. Korppi, A. Jöckel, T. W. Hänsch & P. Treutlein; «Coupling ultracold atoms to mechanical oscillators»; Comptes Rendus Physique **12**, p. 871–887 (2011). ISSN 16310705. http://linkinghub.elsevier.com/retrieve/pii/S1631070511001198. 10

[35] H. Ritsch, P. Domokos, F. Brennecke & T. Esslinger; «Cold atoms in cavity-generated dynamical optical potentials»; Reviews of Modern Physics **85**, p. 553–601 (2013). ISSN 0034-6861. 10

[36] V. Jain, J. Gieseler, C. Moritz, C. Dellago, R. Quidant & L. Novotny; «Direct Measurement of Photon Recoil from a Levitated Nanoparticle»; Physical Review Letters **116**, p. 243 601 (2016). ISSN 0031-9007. 10

[37] A. T. M. A. Rahman & P. F. Barker; «Laser refrigeration, alignment and rotation of levitated Yb3+:YLF nanocrystals»; Nature Photonics **11**, p. 634–638 (2017). ISSN 1749-4885. 10

[38] U. Delić, M. Reisenbauer, D. Grass, N. Kiesel, V. Vuletić & M. Aspelmeyer; «Cavity Cooling of a Levitated Nanosphere by Coherent Scattering»; Physical Review Letters **122**, p. 123 602 (2019). ISSN 0031-9007. 10

[39] M. Aspelmeyer, T. J. Kippenberg & F. Marquardt; «Cavity optomechanics»; Reviews of Modern Physics **86**, p. 1391–1452 (2014). ISSN 0034-6861. 10

[40] DrBob; «https://en.wikipedia.org/wiki/Gaussian_beam#/media/File:GaussianBeamWaist.svg»; . 12

[41] S. S. Y. Chua; *Quantum Enhancement of a 4km Laser Interferometer Gravitational-Wave Detector*; Thèse de doctorat; The Australian National University; Canberra (2013). 20, 22, 27, 35, 80, 84

[42] R. V. Pound; «Electronic Frequency Stabilization of Microwave Oscillators»; Review of Scientific Instruments **17**, p. 490–505 (1946). ISSN 0034-6748. 28

[43] R. W. P. Drever, J. L. Hall, F. V. Kowalski, J. Hough, G. M. Ford, a. J. Munley & H. Ward; «Laser phase and frequency stabilization using an optical resonator»; Applied Physics B Photophysics and Laser Chemistry **31**, p. 97–105 (1983). ISSN 14320649. 28

[44] S. Hum & M. M. Fejer; «doi:10.1016/j.crhy.2006.10.022»; C. R. Physique **8**, p. 180–198 (2007). http://france.elsevier.com/direct/COMREN/Recentadvancesincrystaloptics/AvancÃľesrÃľcentesenoptiquecristalline. 32

[45] Robert W. Boyd; *Nonlinear Optics* (Elsevier) (2003); ISBN 9780121216825. 32

[46] P. Kwee, J. Miller, T. Isogai, L. Barsotti & M. Evans; «Decoherence and degradation of squeezed states in quantum filter cavities»; Phys. Rev. D **90**, p. 062 006–062 018 (2014). 42, 104

[47] M. Poggio, C. L. Degen, H. J. Mamin & D. Rugar; «Feedback Cooling of a Cantilever's Fundamental Mode below 5 mK»; Physical Review Letters **99**, p. 017 201 (2007). ISSN 0031-9007. 48

[48] M. F. Gely & G. A. Steele; «Superconducting electro-mechanics to test Diósi-Penrose effects of general relativity in massive superpositions»; AVS Quantum Science **3**, p. 035 601 (2021). ISSN 26390213. https://avs.scitation.org/doi/abs/10.1116/5.0050988. 52

[49] J. Chan, T. P. M. Alegre, A. H. Safavi-Naeini, J. T. Hill, A. Krause, S. Gröblacher, M. Aspelmeyer & O. Painter; «Laser cooling of a nanomechanical oscillator into its quantum ground state.»; Nature **478**, p. 89–92 (2011). ISSN 1476-4687. http://www.ncbi.nlm.nih.gov/pubmed/21979049. 51, 54

[50] R. Penrose; «On Gravity's role in Quantum State Reduction»; General Relativity and Gravitation 1996 28:5 **28**, p. 581–600 (1996). ISSN 1572-9532. https://link.springer.com/article/10.1007/BF02105068. 52

[51] L. Diósi; «Intrinsic time-uncertainties and decoherence: comparison of 4 models»; Brazilian Journal of Physics **35**, p. 260–265 (2005). ISSN 0103-9733. http://www.scielo.br/j/bjp/a/sGRL93zxZCZrP8XzkhYywSs/?lang=en. 52

[52] D. Rugar, R. Budakian, H. J. Mamin & B. W. Chui; «Single spin detection by magnetic resonance force microscopy.»; Nature **430**, p. 329–332 (2004). ISSN 1476-4687. http://www.ncbi.nlm.nih.gov/pubmed/15254532. 54

[53] F. Fogliano, B. Besga, A. Reigue, P. Heringlake, L. Mercier de Lépinay, C. Vaneph, J. Reichel, B. Pigeau & O. Arcizet; «Mapping the Cavity Optomechanical Interaction with Subwavelength-Sized Ultrasensitive Nanomechanical Force Sensors»; Physical Review X **11**, p. 021 009 (2021). ISSN 2160-3308. 54

[54] P. Arrangoiz-Arriola, E. A. Wollack, Z. Wang, M. Pechal, W. Jiang, T. P. McKenna, J. D. Witmer, R. Van Laer & A. H. Safavi-Naeini; «Resolving the energy levels of a nanomechanical oscillator»; Nature **571**, p. 537–540 (2019). ISSN 0028-0836. 54

[55] K. J. Satzinger, Y. P. Zhong, H.-S. Chang, G. A. Peairs, A. Bienfait, M.-H. Chou, A. Y. Cleland, C. R. Conner, Dumur, J. Grebel, I. Gutierrez, B. H. November, R. G. Povey, S. J. Whiteley, D. D. Awschalom, D. I. Schuster & A. N. Cleland; «Quantum control of surface acoustic-wave phonons»; Nature **563**, p. 661–665 (2018). ISSN 0028-0836. 54

[56] A. D. O'Connell, M. Hofheinz, M. Ansmann, R. C. Bialczak, M. Lenander, E. Lucero, M. Neeley, D. Sank, H. Wang, M. Weides, J. Wenner, J. M. Martinis & A. N. Cleland; «Quantum ground state and single-phonon control of a mechanical resonator.»; Nature **464**, p. 697–703 (2010). ISSN 1476-4687. http://www.ncbi.nlm.nih.gov/pubmed/20237473. 54

[57] Y. Chu, P. Kharel, W. H. Renninger, L. D. Burkhart, L. Frunzio, P. T. Rakich & R. J. Schoelkopf; «Quantum acoustics with superconducting qubits»; Science **358**, p. 199–202 (2017). ISSN 10959203. https://www.science.org/doi/10.1126/science.aao1511. 54

[58] M. Rossi, D. Mason, J. Chen, Y. Tsaturyan & A. Schliesser; «Measurement-based quantum control of mechanical motion»; Nature **563**, p. 53–58 (2018). ISSN 0028-0836. 54

[59] A. H. Ghadimi, S. A. Fedorov, N. J. Engelsen, M. J. Bereyhi, R. Schilling, D. J. Wilson & T. J. Kippenberg; «Elastic strain engineering for ultralow mechanical dissipation»; Science **360**, p. 764–768 (2018). ISSN 10959203. https://www.science.org/doi/10.1126/science.aar6939. 54

[60] E. Verhagen, S. Deléglise, S. Weis, A. Schliesser & T. J. Kippenberg; «Quantum-coherent coupling of a mechanical oscillator to an optical cavity mode.»; Nature **482**, p. 63–67 (2012). ISSN 1476-4687. http://www.ncbi.nlm.nih.gov/pubmed/22297970. 54

[61] L. Y. Chen, M.-r. He, J. Shin, G. Richter & D. S. Gianola; «Measuring surface dislocation nucleation in defect-scarce nanostructures»; Nature Materials **14** (2015). ISSN 1476-1122. http://www.nature.com/doifinder/10.1038/nmat4288. 55

[62] A. Borrielli, M. Bonaldi, E. Serra, A. Bagolini, P. Bellutti, F. S. Cataliotti, F. Marin, F. Marino, A. Pontin, G. A. Prodi, G. Pandraud, P. M. Sarro, G. Lorito & T. Zoumpoulidis; «Design of silicon micro-resonators with low mechanical and optical losses for quantum optics experiments»; Microsystem Technologies 2014 20:4 **20**, p. 907–917 (2014). ISSN 1432-1858. https://link.springer.com/article/10.1007/s00542-014-2078-y. 55, 57

[63] K. G. Lyon, G. L. Salinger & C. A. Swenson; «Linear thermal expansion measurements on silicon from 6 to 340 K ARTICLES YOU MAY BE INTERESTED IN»; Journal of Applied Physics **48**, p. 865 (1977). https://doi.org/10.1063/1.323747. 56

[64] A. G. Kuhn; «Optomécanique en cavité cryogénique avec un micro-pilier pour l 'observation du régime quantique d 'un résonateur mécanique macroscopique»; (2013). 63

[65] R. Metzdorf, L. Neuhaus, S. Zerkani, J. Degallaix, T. Jacqmin, S. Deléglise, T. Briant, J. Reichel, P.-F. Cohadon & A. Heidmann; «Finesse recovery in high- nesse Fabry-Perot micro-cavities»; . 63, 109

[66] L. Neuhaus, R. Metzdorff, S. Zerkani, S. Chua, J. Teissier, S. Del, T. Jacqmin, T. Briant, V. Dolique, C. Michel, L. Pinard, O. L. Traon, C. Chartier, A. Heidmann & P. Cohadon; «Cooling of a 30- µ g optomechanical resonator down to 20 phonons»; p. 1–5. 63

[67] B. Efron & R. J. Tibshirani; *An Introduction to the Bootstrap* (Springer US, Boston, MA) (1993); ISBN 978-0-412-04231-7. 68

[68] H. Kogelnik & T. Li; «Laser Beams and Resonators»; Applied Optics **5**, p. 1550 (1966). ISSN 0003-6935. http://ao.osa.org/abstract.cfm?URI=ao-5-10-1550. 76

[69] A. Lartaux-Vollard; *Beating the Standard Quantum Limit for the gravitational wave detector Advanced Virgo*; Thèse de doctorat; Université Paris-Saclay (2020). 79, 101

[70] M. Zhou, B. X. Yan, G. Bao, Y. Zhang, C. Gawith, D. D. Wang, Y. Qi & Y. Bi; «52% optical-to-optical conversion efficiency in a compact 1.5 W 532 nm second harmonic generation laser with intracavity periodically-poled MgO:LiNbO3»; Laser Physics **20**, p. 1568–1571 (2010). ISSN 1054-660X. https://www.researchgate.net/publication/226654444_52_Optical-to-Optical_Conversion_Efficiency_in_a_Compact_15_W_532_nm_Second_Harmonic_Generation_Laser_with_Intracavity_Periodically-Poled_MgOLiNbO3. 80

[71] P. Patimisco, A. Sampaolo, F. K. Tittel & V. Spagnolo; «Mode matching of a laser-beam to a compact high finesse bow-tie optical cavity for quartz enhanced photoacoustic gas sensing»; Sensors and Actuators A: Physical **267**, p. 70–75 (2017). ISSN 0924-4247. 86

[72] L. Neuhaus; *Cooling a macroscopic mechanical oscillator close to its quantum ground state*; Thèse de doctorat; Sorbonne Université; Paris (2016). 88

[73] S. Chelkowski, H. Vahlbruch, K. Danzmann & R. Schnabel; «Coherent control of broadband vacuum squeezing»; Physical Review A - Atomic, Molecular, and Optical Physics **75**, p. 043 814 (2007). ISSN 10502947. https://journals.aps.org/pra/abstract/10.1103/PhysRevA.75.043814. 90

[74] Ivanov Edouard; «Optimization of silicon nitride membranes for hybrid superconducting-mechanical circuits»; Rapport technique; Sorbonne Université; Paris (2021). 109

[75] J. D. Thompson, B. M. Zwickl, A. M. Jayich, F. Marquardt, S. M. Girvin & J. G. E. Harris; «Strong dispersive coupling of a high-finesse cavity to a micromechanical membrane.»; Nature **452**, p. 72–75 (2008). ISSN 1476-4687. http://www.ncbi.nlm.nih.gov/pubmed/18322530. 112

[76] D. Hunger, T. Steinmetz, Y. Colombe, C. Deutsch, T. W. Hänsch & J. Reichel; «A fiber Fabry–Perot cavity with high finesse»; New Journal of Physics **12**, p. 065 038 (2010). ISSN 1367-2630. https://iopscience.iop.org/article/10.1088/1367-2630/12/6/065038https://iopscience.iop.org/article/10.1088/1367-2630/12/6/065038/meta. 113, 114

[77] J. Steinlechner, C. Krüger, I. W. Martin, A. Bell, J. Hough, H. Kaufer, S. Rowan, R. Schnabel & S. Steinlechner; «Optical absorption of silicon nitride membranes at 1064 nm and at 1550 nm»; Physical Review D **96**, p. 022 007 (2017). ISSN 2470-0010. 119, 120

[78] M. Evans, L. Barsotti, P. Kwee, J. Harms & H. Miao; «Realistic filter cavities for advanced gravitational wave detectors»; Physical Review D - Particles, Fields, Gravitation and Cosmology **88**, p. 022 002 (2013). ISSN 15507998. https://journals.aps.org/prd/abstract/10.1103/PhysRevD.88.022002. 125

[79] S. A. Fedorov, A. Beccari, A. Arabmoheghi, D. J. Wilson, N. J. Engelsen & T. J. Kippenberg; «Thermal intermodulation noise in cavity-based measurements»; Optica, Vol. 7, Issue 11, pp. 1609-1616 **7**, p. 1609–1616 (2020). ISSN 2334-2536. https://opg.optica.org/viewmedia.cfm?uri=optica-7-11-1609&seq=0&html=truehttps://opg.optica.org/abstract.cfm?uri=optica-7-11-1609https://opg.optica.org/optica/abstract.cfm?uri=optica-7-11-1609. 126

Michaël Croquette **7 décembre 2022**

Sujet : Optomécanique et lumière comprimée

Résumé : Cette thèse porte sur l'étude des bruits fondamentaux qui limitent la sensibilité des mesures interférométriques de position d'un résonateur optomécanique de haut facteur de qualité mécanique, couplé dans un environnement cryogénique à une cavité Fabry-Perot de grande finesse. Nous avons d'abord étudié le bruit thermique du résonateur et l'avons réduit pour nous approcher de l'état quantique fondamental d'un résonateur mécanique macroscopique. Nous présentons nos résultats expérimentaux, obtenus avec deux géométries différentes de résonateurs, en détaillant leurs avantages et inconvénients respectifs. Dans un deuxième temps, nous étudions les sources de bruit liées à la nature quantique de la lumière. Ces deux bruits, le bruit quantique de phase et celui de pression de radiation, sont les limites les plus fondamentales aux mesures interférométriques de position, et limitent déjà la sensibilité des interféromètres gravitationnels sur une large plage de fonctionnement. Nous présentons tout d'abord le développement d'une source de lumière comprimée, optimisée pour sonder les déplacements d'un oscillateur mécanique résonnant dans la gamme du MHz. Cette source réduit aujourd'hui le bruit quantique d'un facteur 2. Nous présentons ensuite succinctement le développement d'une source optimisée pour un interféromètre gravitationnel, pour des fréquences inférieures à quelques kHz. Enfin nous présentons la conception et la réalisation d'une nouvelle géométrie de cavité fibrée cryogénique, couplée au mouvement d'une membrane nanométrique de SiN, qui permettra d'observer le bruit quantique de pression de radiation et de mettre en évidence l'effet de la lumière comprimée sur la mesure.

Mots clés : Optomecanique, Lumière comprimée, Cavité de grande Finesse, Interferométrie, Bruit thermique, Bruit de grenaille quantique, Resonateur de grand facteur de Qualité , Interféromètres pour la detection d'ondes gravitationnelles, Bruit de pression de radiation quantique

Subject : Optomechanics and squeezed light

Abstract: This thesis investigates the fundamental noise that limits the sensitivity of interferometric position measurements of a high mechanical quality factor optomechanical resonator coupled in a cryogenic environment to a high finesse Fabry-Perot cavity. We first studied the thermal noise of the resonator and reduced it to approach the fundamental quantum state of a macroscopic mechanical resonator. We present our experimental results, obtained with two different resonator geometries, detailing their respective advantages and disadvantages. In a second step, we study the sources of noise related to the quantum nature of light. These two noises, the quantum phase noise and the radiation pressure noise, are the most fundamental limits to interferometric position measurements, and already limit the sensitivity of gravitational interferometers over a wide operating range. We first present the development of a compressed light source, optimised to probe the displacements of a resonant mechanical oscillator in the MHz range. This source now reduces the quantum noise by a factor of 2. We then briefly present the development of an optimised source for a gravitational interferometer, for frequencies below a few kHz. Finally, we present the design and implementation of a new cryogenic fibre cavity geometry, coupled to the movement of a nanometric SiN membrane, which will allow us to observe the radiation pressure quantum noise and to highlight the effect of compressed light on the measurement.

Keywords : Optomechanics, Squeezing, High-Finesse cavity, Interferometry, Thermal Noise, Quantum Shot Noise, High-Q Resonator, Gravitational wave Interferometer,Quantum Radiation Pressure Noise